Advanced Electrical Resistivity Modelling and Inversion using Unstructured Discretization

Von der Fakultät für Physik und Geowissenschaften

der Universität Leipzig

genehmigte

DISSERTATION

zur Erlangung des akademischen Grades

doctor rerum naturalium

Dr. rer. nat.,

vorgelegt

von Diplom-Geophysiker Carsten Rücker

geboren am 02. Juli 1973 in Schmölln.

Gutachter: Prof. Dr. Franz Jacobs, Leipzig
Prof. Dr. Ugur Yaramanci, Hannover

Tag der Verleihung: 24. Januar 2011

Bibliographical data

Rücker, Carsten

Advanced Electrical Resistivity Modelling and Inversion using Unstructured Discretization

University of Leipzig, Dissertation
121 pages, 120 references, 42 figures, 12 tables

Abstract

In this dissertation an approach is presented for the three-dimensional electrical resistivity tomography (ERT) using unstructured discretizations. The geoelectrical forward problem is solved by the finite element method using tetrahedral meshes with linear and quadratic shape functions. Unstructured meshes are suitable for modelling domains of arbitrary geometry (e.g., complicated topography). Furthermore, the best trade-off between accuracy and numerical effort can be achieved due to the capability of problem-adapted mesh refinement. Unstructured discretizations also allow the consideration of spatial extended finite electrodes. Due to a corresponding extension of the forward operator using the complete electrode model, known from medical impedance tomography, a study about the influence of such electrodes to geoelectrical measurements is given.

Based on the forward operator, the so-called triple-grid-technique is developed to solve the geoelectrical inverse problem. Due to unstructured discretization, the ERT can be applied by using a resolution dependent parametrization on arbitrarily shaped two-dimensional and three-dimensional domains. A Gauss-Newton method is used with inexact line search to fit the data within error bounds. A global regularization scheme is applied using special smoothness constraints.

Furthermore, an advanced regularization scheme for the ERT is presented based on unstructured meshes, which is able to include a-priori information into the inversion and significantly improves the resulting ERT images. Structural information such as material interfaces known from other geophysical techniques are incorporated as allowed sharp resistivity contrasts. Model weighting functions can define individually the allowed deviation of the final resistivity model from given start or reference values. As a consequent further development the region concept is presented where the parameter domain is subdivided into lithological or geological regions with individual inversion and regularization parameters. All used techniques and concepts are part of the open source C++ library GIMLI, which has been developed during this thesis as an advanced tool for the method-independent solution of the inverse problem.

Contents

1. Overview 7

I. Modelling 11

2. Geoelectrical forward problem 13
2.1. Introduction 13
2.2. Calculation of the total potential 16
2.2.1. Finite element modelling 17
2.3. Calculation of the secondary potential 19
2.4. Solving the system of equations 20
2.5. Mesh generation and refinement 21
2.5.1. Quality measures 22
2.5.2. Discretization for calculating the total potential 22
2.5.3. Discretization for calculating the secondary potential 24
2.6. Modelling geometry effects 26
2.6.1. A subsurface example 27
2.6.2. A complicated surface topography 28
2.7. Computational aspects 31
2.8. Discussion and conclusions 34

3. Modelling finite electrodes 37
3.1. Introduction 38
3.2. The complete electrode model 40
3.3. Verification 42
3.3.1. Influence on surface resistivity arrays 45
3.4. Examples 46
3.4.1. Model tank 46
3.4.2. Plate-shaped electrodes 49
3.4.3. Modelling a good conductor with CEM 52
3.4.4. Vertical electrode chain 53
3.5. Conclusions 54

II. Inversion **57**

4. Inversion on unstructured meshes **59**
4.1. Introduction 59
4.2. Motivation 61
4.3. The three meshes 61
4.4. Inversion scheme 62
  4.4.1. The objective function 62
  4.4.2. Sensitivity calculation 64
  4.4.3. Solution of the inverse subproblem 65
  4.4.4. Choice of the regularization parameter 66
  4.4.5. Line search 67
  4.4.6. Triple-grid inversion scheme 68
4.5. A synthetic example 69
  4.5.1. Synthetic model and data 69
  4.5.2. Geometry effect 71
  4.5.3. Inversion result 71
  4.5.4. Comparison with even surface 74
4.6. Application to field data 75
4.7. Discussion and conclusions 79

5. Advanced electrical resistivity tomography **81**
5.1. Introduction 82
5.2. Method 83
  5.2.1. Generalized minimization approach 83
  5.2.2. Transformation functions 85
  5.2.3. Region concept 86
5.3. Examples 87
  5.3.1. Incorporating structural constraints from seismics 87
  5.3.2. Demonstration of the region concept by an underwater survey 89
  5.3.3. Incorporating borehole parameter information 92
  5.3.4. Solving a 1D inverse problem while modelling in 3D 95
  5.3.5. Geological block inversion 97
5.4. Conclusions 99

6. Summary and Outlook **101**

A. Element integration and shape functions **103**

Bibliography **109**

1. Overview

The Electrical Resistivity Tomography (ERT) denotes an imaging technique for direct current (DC) resistivity data and is a proven area of applied geophysics. The main purpose of ERT is the non-invasive determination of the spatial distribution of the electrical resistivity. The electrical resistivity respectively his reciprocal, the electrical conductivity, depends on several lithological and petrophysical parameters, hence the knowledge about the conductivity distribution permits assumptions about geological settings in the ground.

The field technique is rather simple in its basic application. Apparent resistivity data values are obtained by using spatially distributed four-point measurements and depends on the measured voltage, the injected current and a scaling geometric factor. Modern multi-electrode systems have received a high technical standard nowadays and allow efficient two-dimensional (2D) and three-dimensional (3D) surveys, which make the method today a practical geophysical exploration tool for environmental and engineering studies.

The interpretation of the geoelectrical data represents an inverse problem. The main task of the inversion is to find a discrete distribution of the resistivity in the ground (the so-called model), which can explain the data within their measured errors. Three-dimensional surveys at all scales, subsurface voids and surface topography are challenges that have to be addressed by modern inversion software to reconstruct the resistivity for realistic environments. Additionally, the general problem of all inversion strategies is the ambiguity of the method. However, often additional information or assumptions exists, which might be counteract the problem of ambiguity but can be hardly incorporated by conventional strategies. The modelling, i.e., the simulation of the data based on a given model, is the decisive element of the inversion process. The main request for the modelling is to achieve at least the accuracy of the measured data with minimized effort under consideration of arbitrary modelling geometries and possible sources of systematic errors (e.g., electrode effects).

The central part for both modelling and inversion is the discretization of the area under investigation, which have to meet all requirements for a modern ERT software. Unstructured discretizations are suitable for the modelling as they allow the best trade-off between accuracy and numerical effort and on the other hand they can be chosen problem-adapted for the inversion. However, this requires new techniques that were developed during this work.

In this thesis unstructured discretizations based on tetrahedrons are the fundamentals to develop a forward operator, which acts for the modelling and have to fit all the needs mentioned before. Unstructured discretizations allow also the considerations of spatial extended finite electrodes. Due to a corresponding extension of the forward operator, a study about the influence of such electrodes to geoelectrical measurements is possible for the first time.

Based on the forward operator a flexible inversion strategy is developed with close collaboration with Dr. Thomas Günther (Leibniz Institute for Applied Geophysics, Hannover) as an efficient ERT tool for arbitrarily shaped three-dimensional domains. An advanced regularization scheme based on unstructured meshes allows for the incorporation of both structural and parameter a-priori information into the inversion.

All used techniques and concepts are part of the open source C++ library GIMLi, which has been developed during this thesis as an advanced tool for the method independent solution of the inverse problem. The forward operator which is specially adapted for the DC resistivity problem represents the basis for the application suite BERT (Boundless Electrical Resistivity Tomography) which is increasingly used in the geoelectrical community (e.g, Ullrich et al., 2008; Clément et al., 2009; Bock et al., 2010; Flechsig et al., 2010; Schütze et al., 2010; Doetsch et al., 2010). However, the presented thesis does not show programming issues but the physical and mathematical concepts and is divided into two main parts modelling and inversion and is outlined in the following.

Geoelectrical forward problem This chapter presents the fundamentals for the three-dimensional geoelectrical forward operator using the finite element method with linear and quadratic shape functions on unstructured tetrahedral meshes. The unstructured discretization allows efficient local mesh refinement and most flexible description of arbitrary model geometries. Therefore, refinement strategies are investigated for the efficient calculation of the primary and the secondary electrical potential. The influence of complicated topography on geoelectrical measurements is shown by two examples and quantified by the so-called geometry effect. Furthermore, some approaches are compared for the solution of the resulting system of equations. Essential parts of this chapter have been published in Rücker et al. (2006).

Modelling finite electrodes This chapter provides the physical and mathematical fundamentals of the complete electrode model (CEM), which is known from medical impedance tomography. The geoelectrical forward operator is extended by the CEM and the solution of the electrical field is validated by an analytical model. The influence of spatial extended electrodes to geophysical measurements are quantified by the electrode effect and investigated for typical geoelectrical survey arrays. The electrode effects are studied also for non typical plate electrodes. Beside the capability of considering real current and potential electrodes, two additionally purposes are demonstrated. The use of a passive electrode as a high conductive body within the modelling domain and the realistic simulation of the effects of a drilling using ring electrodes. Essential parts of this chapter are accepted for publication Rücker and Günther (2011).

Inversion on unstructured meshes This chapter introduces the triple-grid inversion technique for efficient determination of three-dimensional resistivity structures based on unstructured tetrahedral meshes and the forward operator described above. The eponymous meshes are described as well as the inversion approach. A Gauss-Newton method is used with inexact line search to fit the data within error bounds. A global regularization scheme is applied using special smoothness constraints. The inverse sub-problem is calculated by an adapted conjugate gradient solver. The technique is applied on a 3D synthetic example and a 3D field-dataset. Both examples containing steep topography. Furthermore, an approach is given for reducing the sensitivity matrix to cope with memory limitations of today's standard PC. Essential parts of this chapter has been published in Günther et al. (2006).

Advanced electrical resistivity tomography This chapter describes an advanced regularization scheme for the flexible incorporation of a-priori information. Beside the theoretical background, transformation functions are introduced, which allow the restriction of the resulting resistivity range by the use of logarithmic barriers. Furthermore, the so-called region concept is developed. The inversion domain is thereby subdivided into lithological or geological regions with individual inversion and regularization parameters. The regularization scheme as well as the region concept is demonstrated on several field examples to show the capability of incorporating structural information (e.g., from refraction seismic surveys) and the considering of discrete resistivity values (e.g., from borehole logs). Regions can also be treated as single parameters, which allows model reduction. This is demonstrated by two further examples. The inversion of a 3D problem that is reduced to its 1D inversion-character and the interpretation of a very sparse dataset. The publication of essential parts of this chapter is in preparation.

Part I.

Modelling

2. Geoelectrical forward problem

Abstract

This section presents a technique for the efficient numerical computation of the electrical potential with the finite element method in three dimensions and arbitrary topography. The crucial innovation is, firstly, the incorporation of unstructured tetrahedral meshes which allow efficient local mesh refinement and most flexible description of arbitrary model geometry. Secondly, considerably more accurate results are achieved by the implementation of quadratic shape functions. Exploiting a secondary potential approach, meshes are downsized significantly in comparison with highly refined meshes for total potential calculation. However, the latter is necessary for the determination of the required primary potential in arbitrary model domains. To start with, homogeneous models with different geometries at the surface and subsurface are simulated to quantify their influence. This results in a so-called geometry effect, which is not only a side effect but may be responsible for serious misinterpretations. Moreover, it represents the basis for treating heterogeneous conductivity models with the secondary potential approach, which is especially promising for the inverse problem.

It is addressed how the resulting system of equations is solved most efficiently using modern multi-frontal direct solvers in combination with reordering strategies or rather traditional preconditioned conjugate gradient methods depending on the size of the problem. Furthermore, a reciprocity approach to estimate modelling errors is presented, and it is investigated to which degree the model discretization has to be refined to yield sufficiently accurate results.

2.1. Introduction

Numerical calculation of the electric field started in the late 1960s using the techniques of integral equations (Dieter et al., 1969), finite elements (Coggon, 1971) and finite differences (Mufti, 1976). A special variant based on integral equations is the boundary element method (Okabe, 1981). Finite difference (FD) calculations in three dimensions go back to Dey and Morrison (1979). They were the methods of choice throughout the 1980s and 1990s and were refined several times. Zhang et al. (1995), e.g., presented improved boundary conditions for a more accurate potential approximation and Spitzer (1995), e.g., introduced efficient preconditioned conjugate gradient solvers to decrease execution time.

By splitting up the total potential (TP) into a known reference potential of a background model and a secondary potential (SP) due to conductivity deviations from the background model, accurate numerical calculations of the secondary potential can be carried out on moderate grids (Coggon, 1971). This technique is known as singularity removal (Lowry et al., 1989) and was enhanced by Zhao and Yedlin (1996). However, it is used only for flat-earth problems with analytically known potentials.

The finite difference method is restricted to orthogonal grids which limit its ability to reproduce non-orthogonal geometries. In recent years, more and more finite element (FE) approaches appeared which are generally not subject to these drawbacks. Besides the aforementioned paper by Coggon (1971), FE formulations of the direct current (DC) resistivity problem are described in Pridmore et al. (1981); Queralt et al. (1991); Li and Spitzer (2002); Zhou and Greenhalgh (2001); Pain et al. (2003). Simulations with surface topography were presented in two dimensions (2D) Coggon (1971); Fox et al. (1980) and three dimensions (3D) Holcombe and Jiracek (1984); Sasaki (1994); Yi et al. (2001). However, the presented algorithms mainly work with block-oriented (structured) discretizations using hexahedral or tetrahedral elements and, thus, do not exploit the full power of the FE approach. Sasaki (1994) and Zhou and Greenhalgh (2001) use tetrahedral grids but since they are derived from bricks the approach is still block-oriented.

Figure 2.1 shows three possible grid types. The grids in (a) and (b) are of type regular (structured). The orthogonal hexahedral grid (a) is the one that is furthermost restricted with respect to geometrical flexibility and local refinement. The local refinement of (b), a non-orthogonal regular hexahedral type, is still awkward and inefficient, but its geometrical adjustability is already increased. The grid in (c) shows an unstructured or irregular tetrahedral type which is evidently the most flexible discretization in this regard. Especially the refinement of regular grids results in an immoderately increased number of nodes, which consequently expands the numerical effort. An unstructured discretization, commonly called mesh, is highly superior to the structured types with respect to the geometrically flexibility and the expected numerical performance, the ration between accuracy and effort.

In this work the C++ class library GIMLI has been developed, which provide the solution of finite element problems and applies the non-commercial mesh generator TetGen Si (2004) for the generation of unstructured tetrahedral meshes. Therefore two subjects can be addressed. Firstly, any model topography and electrode layout can be described flexibly, e.g., arbitrary electrode positions can be represented by prefixed nodes within the mesh. Secondly, the node distribution can be controlled on demand by refining the mesh locally in the vicinity of electrodes or at strong conductivity contrasts, i.e., where strong gradients of the simulated potential require

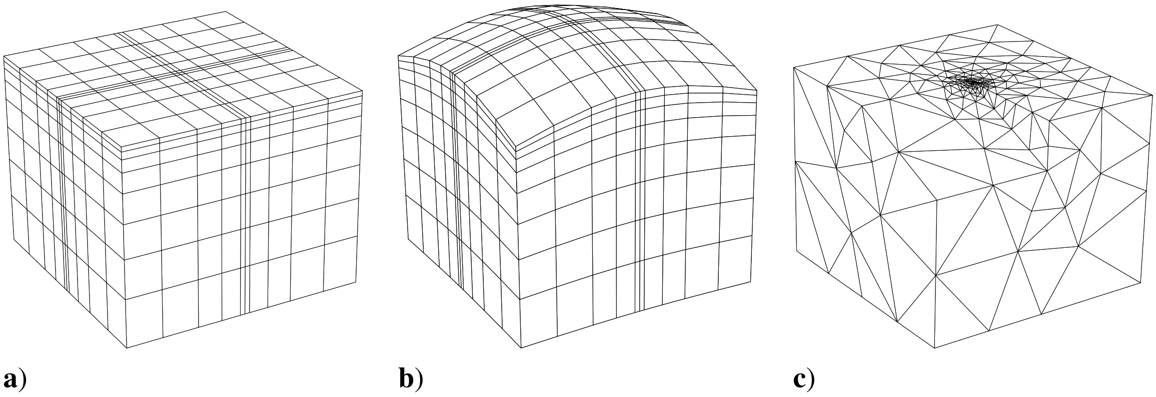

Figure 2.1.: Different grid types: **a**) Orthogonal cuboid, **b**) non-orthogonal hexahedral and **c**) unstructured tetrahedral grid

enhanced accuracy. In return, coarse grids toward the boundaries are sufficient to approximate the rather smooth fields.

As a result of any discretization technique, a sparse system of equations has to be solved for each current location. Spitzer and Wurmstich (1999) gave an overview on non-stationary iterative equation solvers for DC resistivity problems. They suggest conjugate gradient techniques with preconditioners. One very efficient, albeit memory consuming technique is obtained by an incomplete Cholesky decomposition (Kershaw, 1978) as applied to DC modelling by Dey and Morrison (1979) and Li and Spitzer (2002). In contrast to these iterative methods direct equation solvers have made substantial progress in recent years. Multi-frontal decomposition methods going back to Duff et al. (1986) seem to suit best for problems with many right-hand sides, since the decomposition is done only once. The use of reordering techniques helps to limit the memory requirements for direct methods as well as for the incomplete Cholesky preconditioner.

Accuracy in DC resistivity modelling is enhanced not only by grid refinement strategies but also by employing higher order base functions in the FE approach. It can be shown that a combination of both, mesh refinement and quadratic shape functions, yields most efficient solutions.

First an introduction to finite element modelling, unstructured mesh generation and refinement is given. The homogeneous half-space is used to investigate how refinement strategies improve the results for the calculation of the total potential. As a continuation, a conducting half-sphere is used to demonstrate the geometric flexibility of the presented approach and to apply the secondary potential modelling. With the help of two examples it will be shown how complicated subsurface and surface geometry can be involved. A geometry effect is defined to appraise the influence of any topography on DC resistivity measurements. Finally, the computational aspects for the solution of the system of equations are discussed.

2.2. Calculation of the total potential

The boundary value problem for the direct current (DC) resistivity forward problem is given by the equation of continuity with mixed boundary conditions:

$$\nabla \cdot (\sigma \nabla u) = -\nabla \cdot \boldsymbol{j} \;\text{ in }\; \Omega \subset \mathbb{R}^3 \tag{2.1a}$$

$$\frac{\partial u}{\partial \boldsymbol{n}} + \alpha u = 0 \;\text{ on }\; \partial\Omega = \partial\Omega_\mathrm{S} \cup \partial\Omega_\mathrm{I}\,, \tag{2.1b}$$

where $\sigma(x,y,z)$ represents a given conductivity distribution in the ground, $\boldsymbol{j}$ the source current density and u is the sought electrical potential. The electrical resistivity ρ, which is the most widely used material parameter in DC geophysics, equals the reciprocal of σ. The classical geoelectrical source term for the current density $\boldsymbol{j}$ reads

$$\nabla \cdot \boldsymbol{j} = I\delta(\boldsymbol{r} - \boldsymbol{r}_\mathrm{s}) \tag{2.2}$$

and assumes a current I being injected through a point-like electrode situated at $\boldsymbol{r}_\mathrm{s} = (x_\mathrm{S}, y_\mathrm{S}, z_\mathrm{S})$. The Dirac's delta δ forces a singular current density at the source position. The formulation (2.1a) allows point sources at arbitrary positions inside the domain as well as sources on the boundary of the modelling domain. However, the expression does not take into account the physical presence of finite electrodes that may influence practical measurements. Chapter 3 gives a detailed insight into the modelling of finite electrodes and their influence on geoelectrical measurements.

The type of boundary condition for the geoelectrical problem in equation (2.1b) is specialized by α. At the earth's surface $\partial\Omega_\mathrm{S}$ (i.e. air/material interface) homogeneous Neumann conditions ($\alpha = 0$) are applied to avoid current flow through the boundary along the outward normal $\boldsymbol{n}$.

To allow an asymptotic decrease of the potential on an artificial subsurface boundary $\partial\Omega_\mathrm{I}$, Dey and Morrison (1979) impose $\alpha = (\boldsymbol{n} \cdot \boldsymbol{r})/r^2$ for a current source at the earth's surface, whereas $r = |\boldsymbol{r}|$ is the radial distance between the current source and the corresponding boundary. A more generally form for a buried current source inside the domain is given by (Zhou and Greenhalgh, 2001)

$$\alpha = \frac{r'^3 \boldsymbol{n} \cdot \boldsymbol{r} + r^3 \boldsymbol{n} \cdot \boldsymbol{r}'}{(r^3 r'^3 (r + r'))} \tag{2.3}$$

with $r' = |\boldsymbol{r}'|$ where $\boldsymbol{r}'$ denotes the image position of $\boldsymbol{r}$ regarding the earth's surface. This type of boundary condition is sometimes referred to as Robin type (Herwanger et al., 2004).

Note that on pure Neumann domains, e.g. $\alpha = 0$ on the whole boundary as in modelling tanks, there are two additional requirements ensuring a unique solution. First, the conservation of charge $\int_{\partial\Omega} \boldsymbol{j} \cdot \boldsymbol{n} = 0$ (total current flow on the whole boundary $\partial\Omega$ is zero), which can simply be achieved by using a reference electrode or dipole current pattern. Secondly, since only derivatives of u are present on the boundary, the solution of equation (2.1) becomes ambiguous and hence the system of equations becomes singular. This can be avoided by choosing an arbitrary reference point on the boundary with the additional condition $u = 0$.

2.2.1. Finite element modelling

To find a unique solution for equation (2.1a) considering the boundary conditions (2.1b), the finite element method (FEM) (Zienkiewicz, 1977) is applied.

There are two approaches to FEM, the variational formulation (Pridmore et al., 1981; Sasaki, 1994; Li and Spitzer, 2002) and weighted residuals (Zhou and Greenhalgh, 2001). Both approaches lead to the so-called weak formulation of the boundary value problem. This weak formulation allows a piecewise approximation of the solution u but does not require the existence of a continuous second derivative.

The method of weighted residuals is more general and (in case of the DC problem) equivalent to the variational formulation (Zhou and Greenhalgh, 2001). For a generalized partial differential equation (PDG) $D(u)+f=0$ exists an approximated solution $u_h \approx u$ which solves the PDG with a residuum R, $D(u_h)+f=R$. Choose yet undetermined weighting function w which fulfil the condition

$$\int\limits_{\Omega} wR \,\mathrm{d}\Omega = 0\,. \tag{2.4}$$

Applying the weighted residuals approach (2.4) on the fundamental DC equation (2.1a) and further partial integration to vanish the second derivatives, leads to the weak formulation of the DC resistivity forward operator:

$$\int\limits_{\Omega} \sigma\nabla w \nabla u \,\mathrm{d}\Omega - \int\limits_{\partial\Omega} \sigma w \frac{\partial u}{\partial \boldsymbol{n}} \,\mathrm{d}\partial\Omega = \int\limits_{\Omega} w\nabla\cdot\boldsymbol{j}\,\mathrm{d}\Omega\,. \tag{2.5}$$

The 2nd term on the left side is a placeholder for the boundary conditions from equation (2.1b) which are necessary to solve the equation. The Neumann boundary condition $\partial u/\partial \boldsymbol{n} = 0$ on the boundary $\partial\Omega_{\mathrm{S}}$ is automatically satisfied hence their common name, natural boundary condition. The Robin boundary condition on $\partial\Omega_{\mathrm{I}}$ is applied with $\partial u/\partial \boldsymbol{n} = -\alpha u$ so the complete weak formulation can be read as:

$$\int\limits_{\Omega} \sigma\nabla w \nabla u \,\mathrm{d}\Omega + \int\limits_{\partial\Omega_{\mathrm{I}}} \sigma w \alpha u \,\mathrm{d}\partial\Omega = \int\limits_{\Omega} w\nabla\cdot\boldsymbol{j}\,\mathrm{d}\Omega \tag{2.6}$$

which has to be solved for a set of appropriate weighting functions w.

The fundamental FEM principle provides the approximated solution u_h belonging to $\mathcal{N}$ discrete points (nodes) within the domain:

$$u \approx u_h = \sum_{i=1}^{\mathcal{N}} N_i u_{h_i} \tag{2.7}$$

The base functions N represent interpolation rules for the sought potential u_h in each node. The subscript $_h$ can be interpreted as the smallest distance between two nodes hence converge $u_h \rightarrow u$ for $h \rightarrow 0$.

Applying the FEM approximation rule (2.7) to the weak formulation (2.6) and determining the unknown weighting functions after Galerkin's criterion ($w_j = N_j$) (Zienkiewicz, 1977) leads to the finite element approximation for the DC forward problem:

$$\sum_{i=1}^{\mathcal{N}} u_{h_i} \left(\int\limits_{\Omega} \sigma \nabla N_j \nabla N_i \, \mathrm{d}\Omega + \int\limits_{\partial\Omega_\mathrm{I}} \sigma \alpha N_j N_i \, \mathrm{d}\partial\Omega \right) = \int\limits_{\Omega} N_j \nabla \cdot \boldsymbol{j} \, \mathrm{d}\Omega \quad \text{for} \quad j = 1 \ldots \mathcal{N}. \tag{2.8}$$

Dissecting the domain into $\mathcal{C}$ elements (hence the name finite element method) with element-wise constant conductivity $\sigma^{(e)}$ and $\mathcal{B}_\mathrm{I}$ inner boundaries leads to a symmetrical system of equations:

$$\begin{aligned} \mathbf{A}\mathbf{u} &= \mathbf{b}\,, \qquad (2.9)\\ \text{with } \mathbf{A} &= \sum_{e=1}^{\mathcal{C}} \sigma^{(e)} \mathbf{S}^{(e)} + \sum_{b=1}^{\mathcal{B}_\mathrm{I}} \sigma^{(b)} \alpha^{(b)} \mathbf{M}^{(b)}\,, \\ \mathbf{b} &= \sum_{e=1}^{\mathcal{C}} \mathbf{l}^{(e)} I \delta(\boldsymbol{r} - \boldsymbol{r}_\mathrm{s}) \\ \text{and } \mathbf{u} &= [u_{h_i}]\,, \quad \text{for } i = 1 \ldots \mathcal{N} \end{aligned}$$

that can be assembled from local element matrices:

$$\begin{aligned} \mathbf{S}^{(e)} &= \int\limits_{\Omega^{(e)}} \nabla N_k \nabla N_l \, \mathrm{d}\Omega\,, \quad \mathbf{l}^{(e)} = \int\limits_{\Omega^{(e)}} N_k \, \mathrm{d}\Omega \quad \text{for } k,l = 1 \ldots \mathcal{N}^{(e)} \\ \text{and } \mathbf{M}^{(b)} &= \int\limits_{\partial\Omega^{(b)}} N_k N_l \, \mathrm{d}\partial\Omega \quad \text{for } k,l = 1 \ldots \mathcal{N}^{(b)}\,. \end{aligned} \tag{2.10}$$

$\mathbf{S}^{(e)}$ is referred to as the so-called local stiffness matrix for each element $\Omega^{(e)}$, $\mathbf{M}^{(b)}$ the local mass element matrix for each boundary element $\partial\Omega^{(b)}$ and $\mathbf{l}^{(e)}$ the load vector for the respective element $\Omega^{(e)}$ that contains a current source. The contributions from these matrices depend on the type of the element as well as on the base functions N. For details on the implementation with linear and quadratic base functions refer to Appendix A.

2.3. Calculation of the secondary potential

The Dirac delta function δ in the source term of the DC equation (2.1a) leads to infinite potential gradients at the source position $\boldsymbol{r}_\mathrm{s}$. Typically, this singularity is responsible for very poor numerical approximations, particularly close to the electrode positions. The singularity can be removed according to a procedure described by Coggon (1971) for FE and Lowry et al. (1989) for FD. The total potential (TP) u is split up into a primary and a secondary part, $u = u_\mathrm{p} + u_\mathrm{s}$. The primary potential u_p is a known electrical field for a given background conductivity structure σ_p and satisfies the source term: $\nabla \cdot (\sigma_\mathrm{p} \nabla u_\mathrm{p}) = -\nabla \cdot \boldsymbol{j}$. Usually the analytical solution for the homogeneous half-space is used but also more complex background structures (vertical dike or layered models) can be applied (Li and Spitzer, 2002).

The boundary value problem for the secondary potential (SP) reads:

$$\nabla \cdot (\sigma \nabla u_\mathrm{s}) = \nabla \cdot ((\sigma_\mathrm{p} - \sigma) \nabla u_\mathrm{p}) \;\; \text{in} \;\; \Omega \tag{2.11a}$$

$$\frac{\partial u_\mathrm{s}}{\partial \boldsymbol{n}} + \alpha u_\mathrm{s} = \frac{\partial u_\mathrm{p}}{\partial \boldsymbol{n}} + \alpha u_\mathrm{p} = 0 \;\; \text{on} \;\; \partial\Omega_\mathrm{I}\,, \tag{2.11b}$$

where the singular current density $\boldsymbol{j}$ is vanished. However, the integral of equation (2.11a) contains the gradient of the primary potential u_p. The precondition for it being regular is that the conductivity in the direct vicinity of the electrode equals σ_p, as already mentioned by Zhao and Yedlin (1996). To determine σ_p, the local conductivity at the electrodes has to be chosen and not the mean conductivity as suggested by Lowry et al. (1989). Secondary sources appear where the conductivity deviates from σ_p.

Both left-hand side and right-hand side differential operators are identical to that of the total potential. By approximating the operators by matrices the system of equations can be written as

$$\mathbf{A}^{\sigma} u_\mathrm{s} = \mathbf{A}^{\sigma_\mathrm{p} - \sigma} u_\mathrm{p}\,. \tag{2.12}$$

In order to avoid the assembling of $\mathbf{A}^{\sigma_\mathrm{p} - \sigma}$ for each source conductivity σ_p, the linearity of $\mathbf{A}$ is exploited by

$$\mathbf{A}^{\sigma_\mathrm{p} - \sigma} u_\mathrm{p} = (\mathbf{A}^{\sigma_\mathrm{p}} - \mathbf{A}^{\sigma}) u_\mathrm{p} = \mathbf{A}^{1} u_\mathrm{p} \sigma_\mathrm{p} - \mathbf{A}^{\sigma} u_\mathrm{p}\,. \tag{2.13}$$

Thus only one matrix $\mathbf{A}^1$ for a homogeneous conductivity of 1 has to be created additionally to $\mathbf{A}^{\sigma}$ for the whole forward calculation with many sources and heterogeneous conductivity distribution.

2.4. Solving the system of equations

The boundary conditions and, thus, the corresponding matrix entries depend on the source position. In order to avoid the intense reassembling of the coefficient matrix for each individual source of a multi-electrode system a constant average source position for the boundary conditions is used, which is sufficiently accurate since the boundaries are generally far away from the sources. Hence, the matrix **A** is constant.

For the total and the secondary potential a system of equations $\mathbf{A}\mathbf{u}^l = \mathbf{b}^l$ has to be solved for each current source $l = 1, \ldots, \mathcal{E}$, where $\mathcal{E}$ is the number of current sources, i.e. number of used electrodes. Thus, the system of equations is solved $\mathcal{E}$ times. Given that the individual electrodes usually used more than once in typical DC measurements, it is most efficient to calculate the potential for each single electrode and superpose the results.

Matrix **A** is symmetrical, sparse, positive definite and of dimension $\mathcal{N} \times \mathcal{N} \in R$ where $\mathcal{N}$ is the amount of nodes used for the discretization of the modelling domain. With linear shape functions generally between 3 and 20 non-zero entries per row, with a mean of around 14, are obtained.

For the solution of such large systems of equations with sparse matrices, conjugate gradient (CG) methods (Hestenes and Stiefel, 1952) prove to be very efficient (Spitzer and Wurmstich, 1999). Their convergence can be significantly improved by the use of preconditioners. A very efficient preconditioner for many right-hand side vectors is achieved by incomplete Cholesky (IC) factorization of **A**, because the preconditioning process is done only once and the number of iterations per individual right-hand side vector is drastically reduced. There are two main variants of the incomplete factorization (Saad, 1996; Zhou and Greenhalgh, 2001). One restricts the non-zero elements to the sparsity structure of **A** (Dey and Morrison, 1979; Li and Spitzer, 2002; Wu et al., 2003). Another variant allows fill-in but neglects values smaller than a certain threshold (Saad, 1996). In the following addressed as IC-nofill and IC-droptol.

The conjugate gradient method using IC-droptol is something like a hybrid between iterative and direct methods. An IC decomposition with a threshold of 0 corresponds to a direct solver since the iteration is stopped after 1 iteration step. Consequently, direct methods are the matter of choice, if there is enough memory to save the complete Cholesky factor. In recent years multi-frontal algorithms have been developed (Duff et al., 1986), which allow for efficient Cholesky decomposition. The C library TAUCS (Toledo et al., 2001) as iterative solver based on the multi-frontal method and the direct sparse Cholesky factorization package CHOLMOD (Chen et al., 2009) were used.

The fill-in produced by the (complete or incomplete) Cholesky factorization can be significantly diminished by reordering the matrix rows and columns. Historically, the oldest methods are

Cuthill-McKee (CMK) and Reverse Cuthill-McKee (RCM). A detailed description of the individual methods would go beyond this paper and can be found in mathematical literature (Saad, 1996). Generally, three classes exist:

- Nested dissection (ND) is based on geometrical node separation (graph partitioning). A popular and very efficient implementation is METIS (Karypis and Kumar, 1998).

- Minimum degree (MD) methods try to reduce the neighbouring relations (degrees) of the nodes. Popular methods are multiple minimum degree (MMD) and approximate minimum degree (AMD) (Amestoy et al., 1996).

- Minimum deficiency (MF) is a much more extensive technique which successively eliminates the nodes with minimal fill-in (Davis et al., 2000).

2.5. Mesh generation and refinement

An initial partitioning of the modelling domain often incorporates the given electrode layout as fixed nodes. However, an additional refinement has to be applied to obtain accurate forward calculations due to the singular potential at the electrodes. The existing approaches use block-oriented grids for both FD and FE calculations (Loke and Barker, 1996b; Wu et al., 2003; Yi et al., 2001). To minimize the error of the forward calculation, grid lines between the electrodes are introduced. Using between two and four additional grid lines all calculations end up in around 4% relative error for a pole-pole configuration (Yi et al., 2001).

For a successive superposition of configurations with large geometric factors (such as dipole-dipole) a further refinement is required since the relative error is amplified by the geometric factor. However, since refining block-oriented grids always works in a global way, the number of nodes increases rapidly. One main advantage of unstructured meshes is the facilitation of refining grids within distinct regions. Thus in regions of varying potential gradients (close to electrodes) the mesh can be chosen very fine whereas the cell sizes grow toward the boundaries of the modelling domain.

It can be distinguished between a-posteriori and a-priori refinement. For the former, the discretization depends on an error estimation procedure in the solution process, whereas for the latter, the information is introduced in advance. Since the critical regions are known, the a-priori type is chosen to enforce a locally fine mesh by introducing additional supporting nodes to the mesh generation process.

2.5.1. Quality measures

In addition to the local node density, the approximation quality depends on the cell size growth (or prolongation) factor. This can mainly be controlled by the ratio of the tetrahedral edge lengths and the radius of the circumscribing sphere. Since sliver-shaped elements yield poor approximation properties, so-called mesh generators try to minimize the radius-edge ratio. The maximum ratio throughout the mesh can be used as a global mesh quality control.

The applied mesh-generator TetGen (Si, 2004) tries to force all radius-to-edge ratios below a certain quality constraint. For all subsequent meshes a radius-to-edge ratio of 1.2 is chosen, which, due to experience, provides sufficiently accurate results.

To create an unstructured mesh the domain has to be defined by points, polygons or faces, the so-called piecewise linear complex (PLC) (Si, 2004). It includes the geometry of the domain and the electrode locations as well as the boundary. By introducing nodes and creating tetrahedral elements, the mesh generator creates the mesh of the desired quality.

In the following study, local and global refinement techniques are investigated to find a best trade-off between accuracy and computational effort. In addition to the spatial mesh refinement (h-method), the use of higher order shape functions (p-method) was taken into account.

2.5.2. Discretization for calculating the total potential

A uniform earth with a flat surface boundary offers the most simple analytical solution for a homogeneous resistivity distribution $\rho = 1/\sigma = 1\,\Omega\mathrm{m}$ with:

$$u = \frac{I\rho}{2\pi|\boldsymbol{r} - \boldsymbol{r}_\mathrm{s}|} \tag{2.14}$$

at radial distance $\boldsymbol{r}(x,y,z)$ from source location $\boldsymbol{r}_\mathrm{s}(x_\mathrm{s},y_\mathrm{s},z_\mathrm{s})$.

A straight line is defined containing 21 electrode nodes with 1 m spacing. The model boundaries are placed at 5 km around the origin in order to minimize the effects of the boundary conditions. The first mesh created by the mesh generator TetGen obtains 2047 nodes.

Figure 2.2 shows the relative deviations of a pole-pole sounding curve between analytical and numerical solutions at the electrode locations. The numerical results can be read directly from the FEM solution u at the given nodes for the electrodes. In the vicinity of the source electrode quite large errors can be observed, whereas the error stabilizes at around 5% with increasing distance.

To diminish the large errors at the sources, the discretization density is increased around the source node. By adding supporting points at a fixed depth dz below the electrodes, the mesh

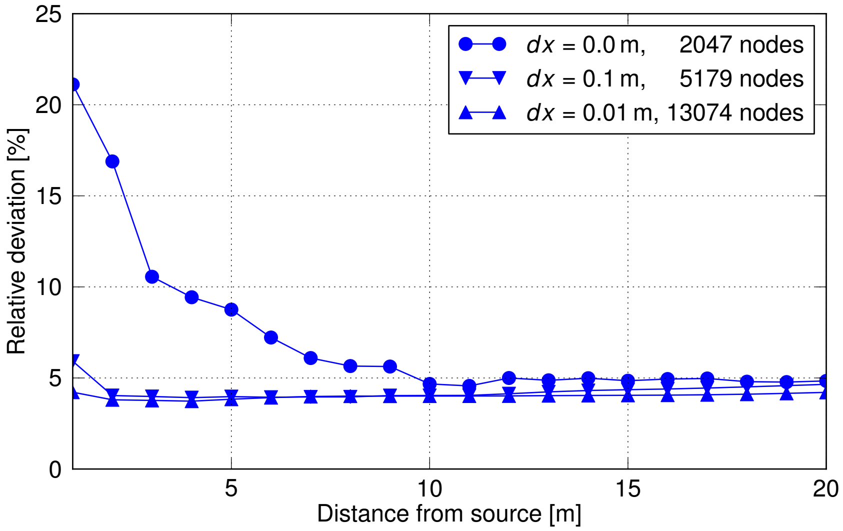

Figure 2.2.: Relative deviation between analytical and numerical solutions of a pole-pole sounding for three meshes with increasing local refinement around the source electrode (total potential calculations).

generator is forced to apply a local refinement. In addition to the coarse unrefined mesh denoted by $dz = 0.0$ m (2 047 nodes), Figure 2.2 shows the results for the locally refined meshes denoted by $dz = 0.1$ m (5 179 nodes) and $dz = 0.01$ m (13 074 nodes). The error is almost constant for $dz = 0.1$ m. The later local refinement ($dz = 0.01$ m) yields only a negligible improvement. Therefore an a-priori mesh refinement of $dz = 0.1$ m is proposed sufficient and used in the further.

Apparently, a global refinement is needed to enhance the global error level of $\approx 4\%$. The simplest strategy is to bisect all tetrahedron edges (h-refinement) such that each tetrahedron disintegrates into 8 smaller ones. The number of nodes is increased approximately by a factor of 8 (38 533 nodes). Alternatively, the second order polynomials are applied (p-refinement) by replacing the 4-node tetrahedron by a 10-node tetrahedron, with a new node at each edge centre. Therefore, the resulting amount of mesh nodes is identical to those of the h-refined mesh.

Figure 2.3 shows the relative deviations for the intermediate mesh of Figure 2.2 of 5179 nodes (top), after a global h-refinement to 38 533 nodes (centre), and with the use of quadratic shape functions (bottom, also 38 533 nodes). By global h-refinement the error is halved to less than 2%, whereas quadratic shape functions yield errors around 0.1% and below. The computational effort for solving the system of linear equations is nearly the same in both cases. However, significantly more accurate results can be obtained by using the p-refinement method.

First investigations show that efficiency may not be improved any further by the use of even higher polynomial order. Therefore, the use of moderately locally refined meshes with quadratic shape functions is proposed for all calculations of the total potential.

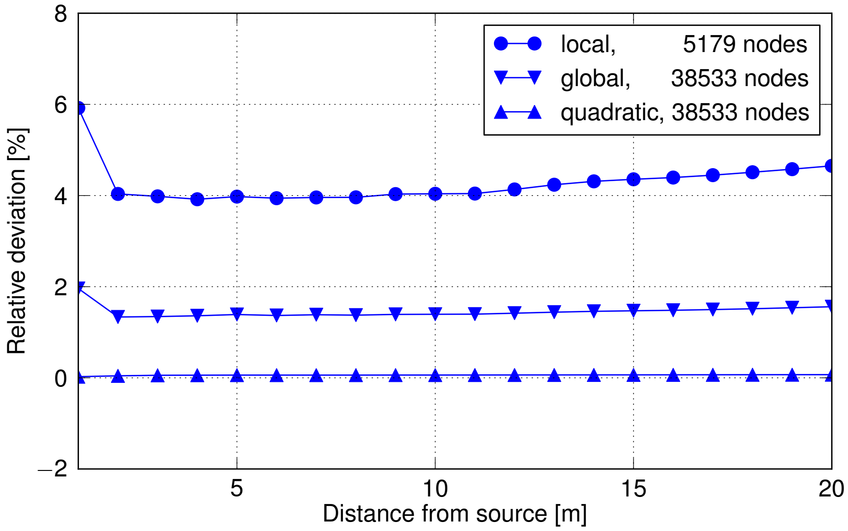

Figure 2.3.: Relative deviation between the numerical and analytical solutions of a pole-pole sounding for different meshes and shape functions (total potential calculations).

2.5.3. Discretization for calculating the secondary potential

In order to show the flexibility of unstructured meshes a spherical anomaly was chosen, which can hardly be discretized by block-oriented grids. The analytical solution for a conducting sphere is known (Large, 1971; Zhdanov and Keller, 1994). However, instead of a sphere in full-space, a half-sphere at the upper boundary of a half-space is considered, on which electrodes are placed along a profile line. Since the half-space boundary is an axis of symmetry, the solution can easily be obtained by doubling the calculated potential values.

The secondary potential is expected to be rather smooth so that the first calculation may start with a quite coarse mesh. Figure 2.4 shows a section of the meaningful parts mesh. A half-sphere with a radius of 2.25 m is placed at the origin. A line of 21 electrodes from $x = -5\,\mathrm{m}$ to $x = 5\,\mathrm{m}$ with a spacing of 0.5 m is defined using fixed nodes. Note that the electrodes can be placed independently of the nodes in general, however, defining fixed nodes in this example avoids possible interpolation issues while collecting the resulting potentials.

The model boundary is also chosen away from the origin in each direction (1000 m). Using a radius-to-edge ratio of 1.2 a mesh of 1769 nodes has been generated on which the secondary potential is simulated. Defining the resistivity of half-sphere to 1 Ωm, whereas the half-space has $\rho_\mathrm{p} = 10\,\Omega\mathrm{m}$. The source electrode is set at $\boldsymbol{r}_\mathrm{s} = (-4;0;0)$ and the primary potential is calculated with equation (2.14) assuming a background resistivity of 10 Ωm.

Consequently, sources for the secondary potential occur only within the half-sphere. The calculated potentials at the remaining electrodes are transformed into apparent resistivities using pole-pole geometric factors. In Figure 2.5, the numerical results are compared to the analytical

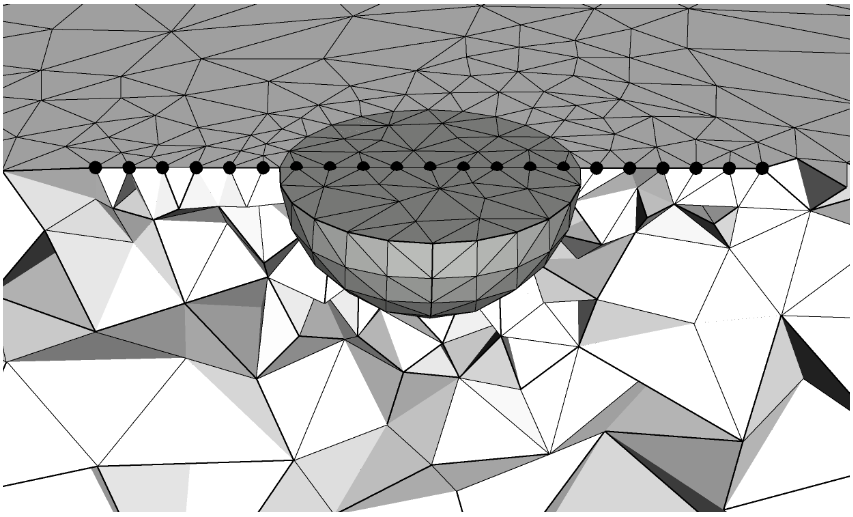

Figure 2.4.: Section of the mesh used for the conducting half-sphere study. The dots denote electrode positions.

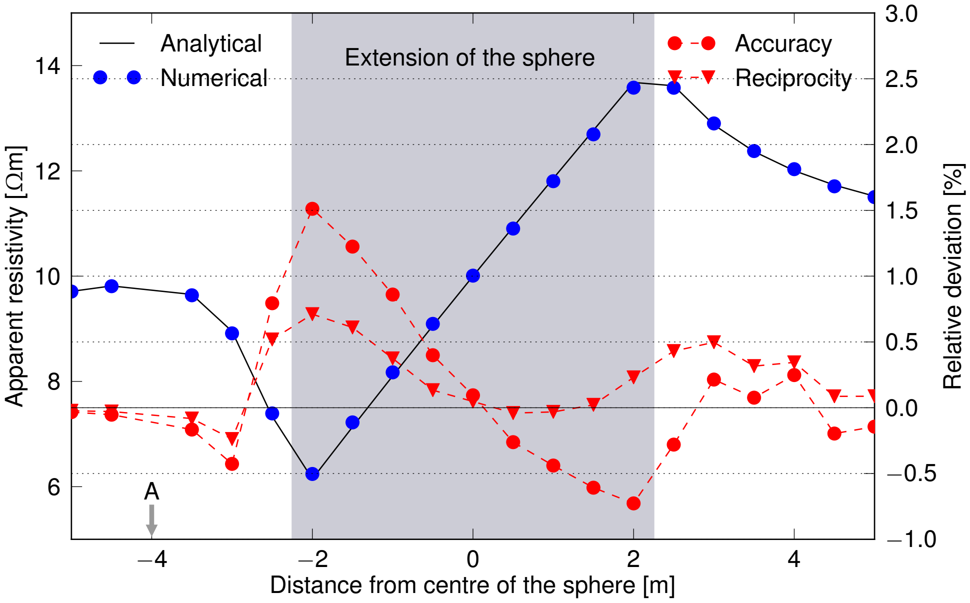

Figure 2.5.: Apparent resistivity of a pole-pole configuration over a conducting half-sphere: comparison of analytical and numerical results using secondary potentials (A is the source position). The right-hand axis denotes the relative deviation and the reciprocity measure r.

solution. Although the number of nodes is very small, the numerical and analytical values agree very well. The relative deviation (right-hand axis) stays below 1% on the whole profile.

In the following a measure of accuracy is derived for cases where the analytical results are not available. Going back to the idea of Coggon (1971), Günther (2004) suggests to appraise the simulation results based on reciprocity. According to the reciprocity principle the measured potential remains constant if current and potential electrodes are interchanged. A deviation from this inevitably corresponds to simulation errors. The reciprocity measure is proposed as an indication for modelling errors:

$$r = 2\frac{\rho^a_{\text{forward}} - \rho^a_{\text{reverse}}}{\rho^a_{\text{forward}} + \rho^a_{\text{reverse}}}, \tag{2.15}$$

where ρ^a_{forward} and ρ^a_{reverse} are the two simulated apparent resistivities with interchanged current and potential electrodes. Figure 2.5 shows that in regions of increased errors the reciprocity measure r rises. To appraise the accuracy of a multi-electrode simulation, the standard deviation and the maximum value of the individual reciprocity measures can be regarded.

In order to compare the SP results with the solution for the total potential, a mesh has been constructed for calculating the latter for the half-sphere model. The refinement factors have been chosen such that the accuracy is just as good as the one depicted in Figure 2.5. This proceeding ends up with 49 341 nodes which is almost 30 times more than for the secondary potential (1 769 nodes). Thus, the secondary potential may be simulated on coarse meshes and with small computational effort. However, if topography is present, the primary potential can only be computed numerically. In the following, the calculation of the primary potential is investigated for a constant resistivity on different non trivial model geometries.

2.6. Modelling geometry effects

In general, the measured electrical impedance $\Delta u/I$ is transformed into the apparent resistivity ρ_a by means of the geometric factor k. The latter is chosen such that the apparent resistivity equals the true resistivity in case of a homogeneous distribution. The geometric factor clearly depends on both, the electrode layout and the surface geometry. If the topography is non-trivial, k is unknown and can only be assessed numerically.

Usually an approximation k_a is based on the half-space potentials (equation (2.14)) for surface measurements. For buried current sources the analytical expression can easily be adapted by introducing an image source position $\boldsymbol{r}'_{\text{s}}$ using the earth's surface as a mirror:

$$\frac{1}{k_a} = u_a = \frac{I}{4\pi}\left(\frac{1}{\boldsymbol{r}_{\text{s}}} + \frac{1}{\boldsymbol{r}'_{\text{s}}}\right). \tag{2.16}$$

It is important for any measurement, to distinguish between effects of the subsurface conductivity distribution and artefacts caused by using wrong geometric factors. Therefore, a geometry effect t is defined as the ratio of the voltage differences for the given geometry Δu and the approximation Δu_a. From the equality of the apparent resistivities the expression for the geometry effect yields:

$$t = \frac{\Delta u}{\Delta u_a} = \frac{k_a}{k}. \tag{2.17}$$

If any surface topography is present, a homogeneous resistivity of $\rho = 1\,\Omega\mathrm{m}$ is assigned to the model and the potential u is calculated numerically. Since ρ_a has to equal ρ the numerical geometric factor can be obtained by $k = I\rho/\Delta u$. To appraise geometry effects, t can be plotted for each datum. With a value of $t = 1$ the measurement is not affected by topography. Values of $t > 1$ refer to increased apparent resistivities whereas values of $t < 1$ indicate a decrease.

2.6.1. A subsurface example

The following example originates from a DC resistivity survey inside a mining gallery. The measurements were carried out at the side wall of the gallery. To interpret the measurements it is of interest to determine whether half-space or full-space approximation has to be used. The influence of the cavity is expressed by the value of the geometric factor k which may be determined by simulating the electric potential for the gallery geometry within a homogeneous conductivity.

The studied mining gallery is 500 m long and has a $5\,\mathrm{m} \times 2\,\mathrm{m}$ cross-section. To minimize potential nonconformities from the outer boundary conditions, the model boundaries are chosen at a distance of 5 km from the gallery. A number of 50 electrodes with 1 m spacing are assumed at one side wall.

Figure 2.6 shows the mesh surface used for the numerical calculations. The gallery itself is described by an inner surface with (no-flow) Neumann boundary conditions ($\alpha = 0$, cf. Chap. 2.2). Alternatively, the problem could be solved by the approach of Queralt et al. (1991), since the resistivity distribution is 2D and the array is parallel to the strike direction. However, this calculation is numerically unstable as mentioned by the author. Furthermore, a more general solution is desirable that allows for involving real 3D geometry.

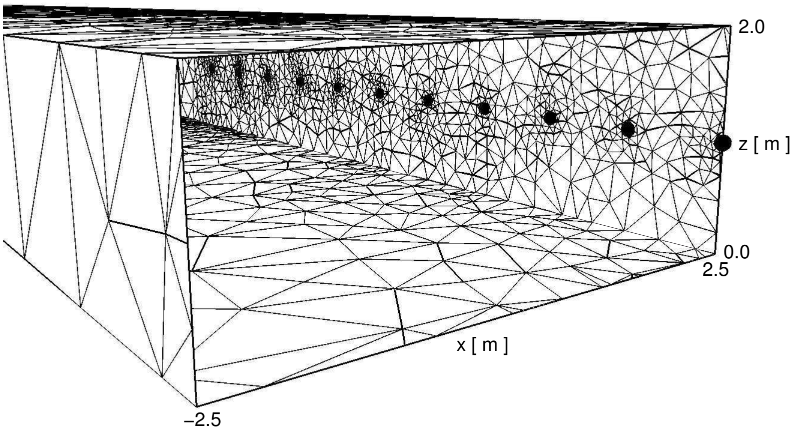

Figure 2.6.: Surface mesh of the mining gallery model showing a part of the cavity. The dots denote electrode positions

A large number of mesh nodes are necessary to describe the model geometry and to approximate the total potentials accurately. With local mesh refinement at the vicinity of the electrodes and global quadratic shape functions the resulting mesh contains 128 169 nodes.

A resistivity of 1 Ωm is assigned to the model and a full-space geometric factor is used to obtain the apparent resistivities ρ_a. Figure 2.7 shows the simulated ρ_a values as a function of the distance between transmitter and receiver dipole (dipole-dipole sounding). The dipole length is the electrode spacing of 1 m.

The curve starts at values around 2 Ωm for small separations, which may be considered as half-space case and corresponds to a topography factor of $t = 2$. As the separation increases, the curve is tending more and more to 1 Ωm which is associated with the full-space case of $t = 1$. For practical applications, the geometry effect can be neglected if it falls below 10%. In the case of the presented gallery this applies for a dipole separation of 15 m and more. However, it has to be considered for small separations.

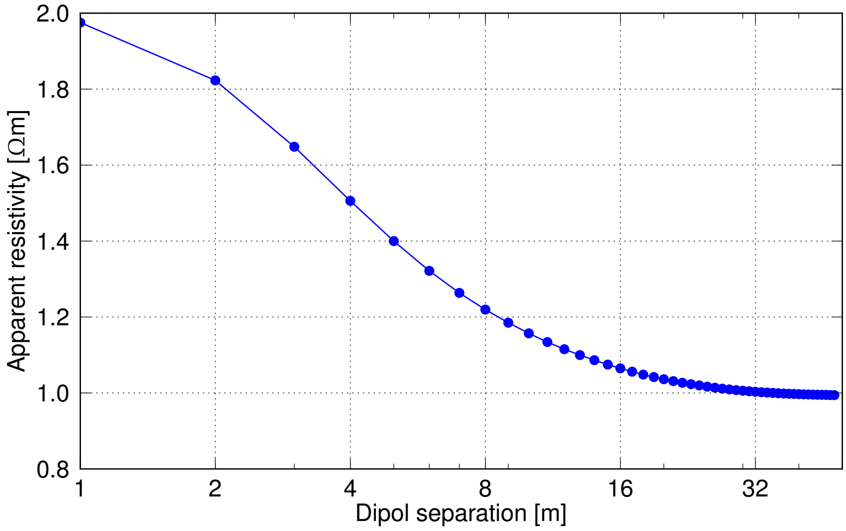

Figure 2.7.: Full-space apparent resistivities of the dipole-dipole sounding as a function of the dipole separation.

2.6.2. A complicated surface topography

To show a practical example with complicated surface topography, a structural investigation at Merapi volcano was selected. Direct current measurements have been conducted in 1998 and 1999 at Merapi's northern, southern and western flanks which show a pronounced topography (Friedel et al., 2000). The northern profile comprises 16 electrodes at ≈ 200 m, a total length of 2600 m, and altitude differences of up to 730 m. This profile is affected massively by the volcano topography.

Some preparation steps are necessary to construct a mesh that contains the complicated topography as well as the nodes for the electrodes. First, a 2D surface mesh is needed to apply the topography. Using the Triangle algorithm (Shewchuk, 2002) a 2D mesh was created that fits the boundary dimension. To satisfy boundary conditions and to include the whole volcano into the model, the boundary is chosen at a distance of 10 km outside the electrodes. The electrode positions are placed with supporting points in a distance of 1 m to ensure local refinement at the electrodes. The resulting 2D mesh (Fig. 2.8b) has only 4 000 nodes, a regular mesh with similar refinement would obtain unlike more.

The TU Darmstadt (Gerstenecker et al., 2005) provides a high-resolution topography data for the area containing more than 350 000 points (Fig. 2.8a). To every node of the 2D mesh an altitude is associated by interpolation. Together with the lower boundary a 3D surface mesh is obtained which is used by Tetgen (Si, 2004) to create the 3D mesh. As a result a tetrahedral mesh of 79 611 nodes is created which reflects Merapi's surface topography. The use of p-refinement for quadratic shape functions yields a mesh with 566 736 nodes. Figure 2.8c shows the mesh of Merapi's northern slope and the position of the used electrodes(bullets). The size of the tetrahedrons is small close to the profile (1 m) and reflecting the volcano's topography to a high degree. However, the cell size grows with distance such that the whole volcano can be simulated at affordable costs.

Figure 2.9 shows the resulting pseudo-section of the topography effect. As expected, half-space values of around $t = 1$ can be found on the left (electrode number 1–10) since the topography on the lowest part of the profile is almost planar. Close to the upper right-hand corner an increase of the resistivities of up to 50% can be observed. Since the current lines are compressed by the valleys running parallel to the electrode line, the resulting voltages and, thus, the apparent resistivities are increased. All readings associated with the last dipole (electrodes 15 and 16), i.e., on a diagonal line from the upper right-hand corner of the pseudo-section to the lower central value, are decreased by 20%. This may be caused by the steep dip of the dipole axis toward the top of the volcano, since the last electrode is situated on top of a narrow ridge.

The potentials for a homogeneous conductivity can be used to determine the geometric factors. Thus, the resulting apparent resistivities contain only the effect of the subsurface. Having calculated the primary potential for arbitrary geometries it is now possible simulate the potentials for arbitrary conductivity distributions using the secondary potential technique on a relatively coarse grid. In Chapter 4, this will be exploited for inversion.

Note that the potentials at the electrodes may also be obtained by the boundary element method (Xu, 2001). This results in solving a dense system of equations where the degree of freedoms equals the number of nodes in the surface mesh. This may be more efficient in some cases. However, to solve the secondary potential, the potential in the interior is needed, which can only be achieved by numerical integration for each node, resulting in a huge numerical effort.

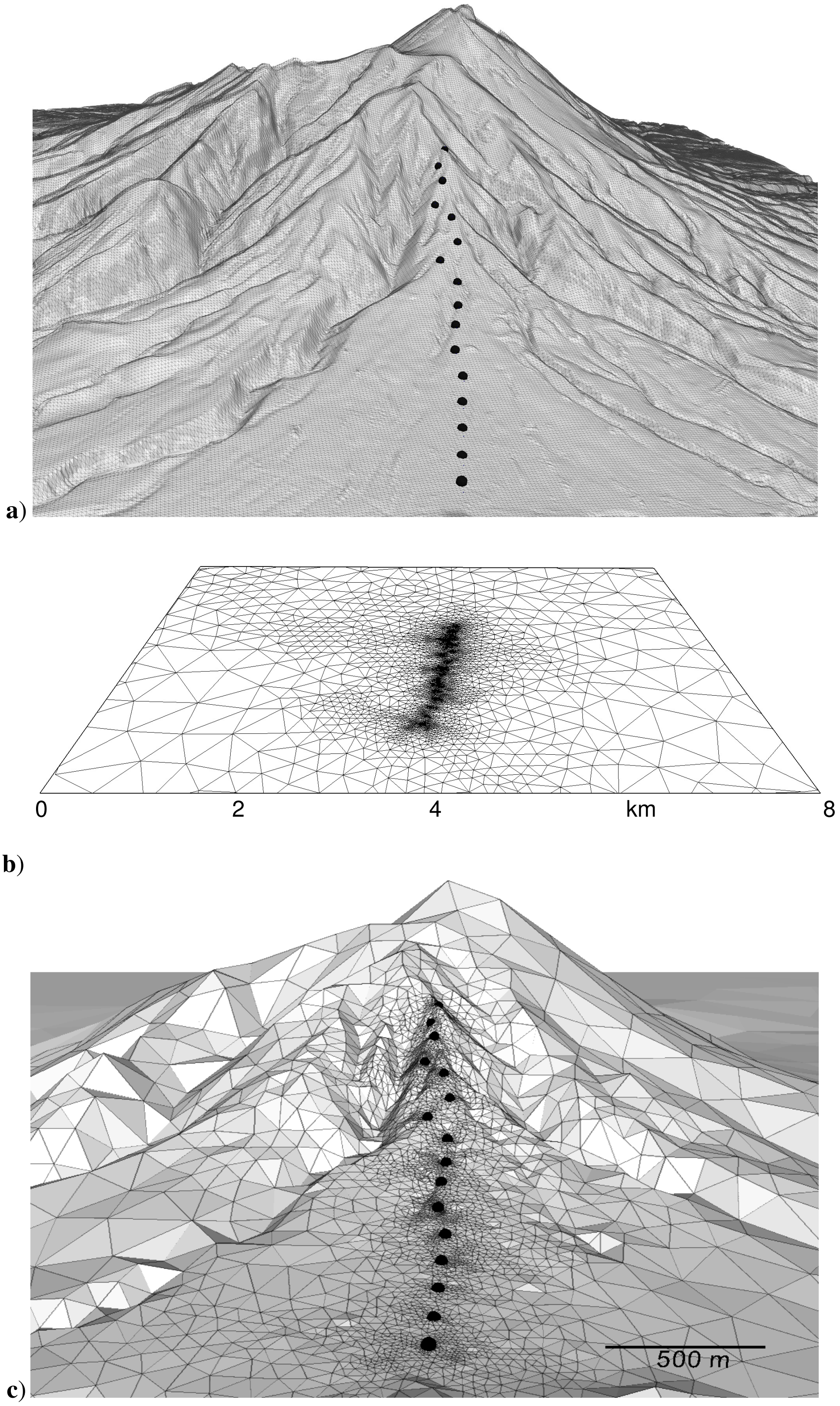

Figure 2.8.: **a**) Highly refined topographical data. **b**) Section of the 2D mesh with local refinement in the vicinity of the electrodes, **c**) 3D surface mesh with topography at the northern slope of Merapi volcano. The dots represent the location of the electrodes.

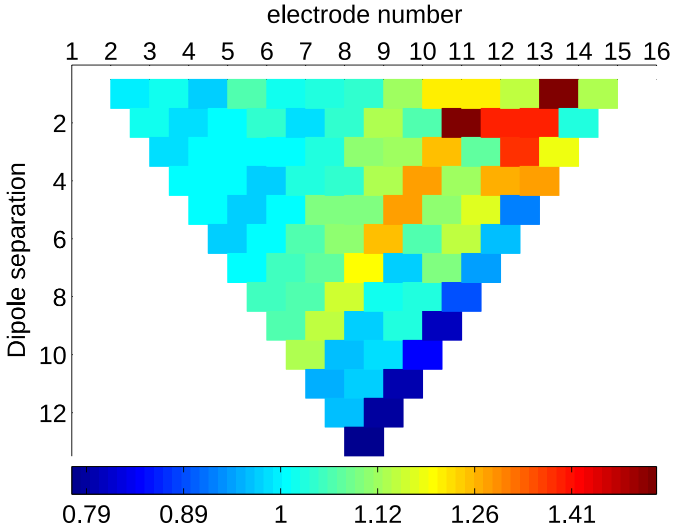

Figure 2.9.: Dipole-dipole pseudo-section of the topography effect t along the profile at the northern slope of Merapi volcano. The origin is at the foot of the mountain. The abscissa denotes the electrode number, the ordinate reflects the dipole separation. The individual values are plotted in the centre between the two dipoles involved.

2.7. Computational aspects

The meshes of the previous sections are now being reviewed with respect to the effort of solving the system of equations. For iterative methods, a stopping criterion has to be defined depending on the accuracy of the solution. Experience shows a relative residual value of 10^{-6} is sufficient for practical purposes and was used in all computations. Table 2.1 gives an overview of the mesh sizes used in the last two sections. The node numbers span a range of almost four orders in magnitude.

Proceeding in the order of the mesh size and starting with the smallest example, the conducting sphere with 1 769 nodes and 21 right-hand side vectors. The stiffness matrix contains 24 427 non-zero entries which is about ≈ 14 per row. Due to the small size, a direct equation solver is appropriate. Once the factorization is done the back-substitutions for the individual sources are obtained almost instantly. The Cholesky factor is computed in 1.85 s and contains 750 238 non-zero elements which need about 11.5 MB memory if 12 bytes/entry are considered.

Table 2.1.: Mesh sizes and number of non-zeros (nnz) in the stiffness matrix for the four meshes of the preceding examples.

Example	Half-sphere	Half-space	Gallery	Merapi
Nodes	1769	38 533	128 169	566 736
nnz	24 427	542 459	$1.86 \cdot 10^6$	$7.74 \cdot 10^6$

To reduce the amount of storage, the matrix rows and columns are reordered in such a way that the number of non-zeros (nnz) in the Cholesky factor is being minimized. Different reordering strategies are compared in Table 2.2: Reverse Cuthill-McKee (RCM), Multiple Minimum Degree (MMD) and Approximate Minimum Degree (AMD) (cf. Chap 2.4).

All methods of reordering can reduce the nnz drastically, also the computing time is decreased by several decades. AMD performs best with a reduction factor of about 6. In Figure 2.10 the sparsity structure is shown for the original and the reordered stiffness matrix. It can be seen that the neighbouring relations of the elements have been changed such that the reordered entries are located near the main diagonal.

The locally refined homogeneous half-space with quadratic shape functions (38 533 nodes) still represents a moderate mesh with a stiffness matrix $\mathbf{A}$ of 542 459 non-zero elements. Without reordering, the Cholesky factor obtains $6.84 \cdot 10^8$ elements corresponding to 780 MB RAM which almost exceeds the memory limits of a current standard PC (1 GB). However, with AMD reordering the allocation can be reduced to $\mathrm{nnz} = 1.07 \cdot 10^7$ or 120 MB. The AMD reordering technique was used for all examples because of its great benefit.

The mining gallery (128 169 nodes, 1.8 Mio nnz's in $\mathbf{A}$, 50 electrodes) represents the next larger problem. The (reordered) Cholesky factor obtains $6.38 \cdot 10^7$ nnz's or 730 MB. On the present PC with 1 GB memory, 200 000 nodes represent the upper limit for direct equation solvers. The algorithm implemented in the CHOLMOD package needs about 3 s for the symbolic analysis and 52 s for the multi-frontal factorization. The following back-substitutions are carried out in 111 s which is about 2 s for each electrode.

The Merapi mesh with 566 736 degrees of freedom cannot be solved with direct methods due to memory limitations. Hence, conjugate gradient (library TAUCS) is chosen for solving the system of equations. Nevertheless, it is worth to carefully choose the preconditioner since the system is solved for each of the 16 electrodes. The incomplete Cholesky preconditioning, as used by Li and Spitzer (2002), was selected and both variants (IC-nofill and IC-droptol, cf. Chap. 2.4) were examined with different thresholds. As for the complete factorization, the nnz can be drastically reduced by AMD reordering.

Table 2.3 shows the computer resources used for various threshold values. The number of iterations and the run time can be decreased by a finer threshold. However, memory requirements

Table 2.2.: Computation time t and number of non-zero entries (nnz) for the Cholesky factor and different reordering strategies (half-sphere).

Reordering	None	RCM	MMD	AMD
t (Chol)	1.85 s	0.06 s	0.09 s	0.09 s
nnz (Chol)	750 238	181 299	150 454	119 843

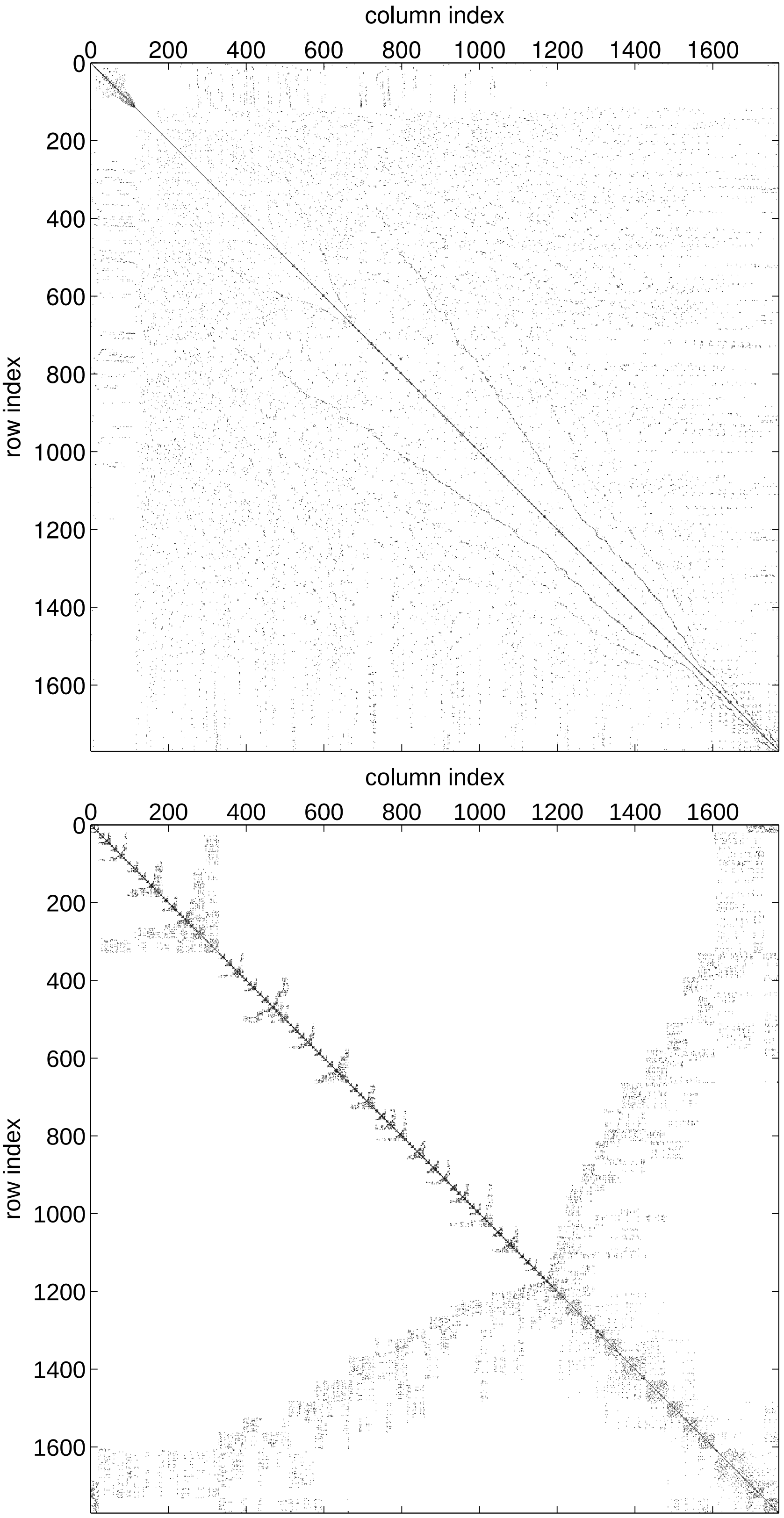

Figure 2.10.: Sparsity structure of the original (upper) and AMD-reordered (lower) stiffness matrix for the mesh of the half-sphere model.

Table 2.3.: Computing time t, memory requirements and number of iterations of the ICCG method for different preconditioners (Merapi mesh with 16 source vectors).

thresh.	time(IC)	memory	iter.	t/iter	total t
nofill	201 s	104 MB	146	1.6 s	65.1 min
10^{-1}	140 s	89 MB	170	1.6 s	74.8 min
10^{-2}	144 s	120 MB	94	1.8 s	47.7 min
10^{-3}	180 s	266 MB	45	2.9 s	37.9 min
10^{-4}	393 s	561 MB	19	5.5 s	34.8 min

grow. An increase of run time for even smaller values than 10^{-4} is to be expected because the back-substitution requires more time for a greater nnz (Günther, 2004).

To summarize, the numerical computations must always find a trade-off between the two resources calculation speed and memory. Mesh size and available computer memory determine the runtime of the solver. Direct methods should be used whenever it possible. Conjugate gradient methods with incomplete Cholesky preconditioners are the alternative in most cases. The threshold value of the incomplete factorization must be chosen carefully to meet memory limits and to minimize calculation time. For very large meshes, the SSOR preconditioner is of advantage since it allows preconditioning without additional storage memory (Spitzer, 1995). However, convergence becomes slower.

2.8. Discussion and conclusions

In this section the simulation of DC resistivity data with finite elements has been addressed. Special attention has been paid to the incorporation of three-dimensional surface and subsurface topography. For this purpose unstructured tetrahedral meshes provide the highest flexibility for describing arbitrary model geometries. The derived geometry effect helps to understand how the physical fields are affected by the geometry of the modelling domain.

It has been distinguished between two techniques, the simulation of the primary potential and the secondary potential. With the latter, accurate simulations can be carried out using small-scale meshes. The main computational effort is associated with the simulation of the primary potential. However, for all problems with several conductivity distributions, that require multiple forward calculations, a gain in efficiency can be achieved by exploiting the secondary potential. This is an important benefit for the inverse problem.

Whereas the secondary potential can be obtained on a relatively coarse mesh, an accurate simulation of the primary potential requires a distinct mesh refinement. A local spatial refinement in the vicinity of the electrodes (at least $1/10$ electrode spacing) is suggested in combination with the global use of quadratic shape functions. A further improvement of efficiency may be achieved by adaptive mesh refinement using an a-posteriori error estimator (Verführt, 1993). The question remains whether the geometry effect or the primary potential can be calculated more efficiently using the boundary element method (Xu et al., 1988; Blome, 2009).

Two ways are proposed to solve the arising systems of equations: Small-scale problems are most efficiently solved by direct multi-frontal solvers. This is the case for all simulations of the secondary potential. Regarding larger systems of equations, as arising mainly from primary potential simulations, the method of choice are conjugate gradient methods with incomplete Cholesky preconditioners. The trade-off depends mainly on the available computer memory to store the Cholesky factor of the matrix. Matrix reordering techniques help to reduce memory requirements drastically.

The presented techniques permit the simulation of complicated geometries and conductivity distributions on standard computers within short time. Hence, the way to three-dimensional inversion with arbitrary topography has been opened up and will be considered in Chapter 4.

3. Modelling finite electrodes

Abstract

Direct current resistivity measurements are usually done using electrodes with finite extension and grounding resistance. However, in the modelling they are commonly treated as ideal point sources. In the following section computations are presented using the complete electrode model (CEM), known from medical imaging, to investigate up to which electrode extension a point approximation is sufficient. The electrode surface is thereby discretized and the partial differential equations are extended by additional relations incorporating the electrodes extent, a (usually unknown) contact impedance z and a condition for the current flow through the electrodes surface. The modelling of the electrical potential is verified by using an analytical solution for a perfectly coupled half-ellipsoid current source ($z = 0$). The potential for a non-zero contact resistance cannot be proved analytically but it behaves as expected for current and potential electrodes. For surface measurements of typical extend, the electrode effect, i.e., the ratio between CEM and a point solution for a homogeneous model, is in the order of the measuring accuracy for an electrode length/spacing ratio lower than 0.2. However, the effects become more noticeable for closed geometries such as modelling tanks or lysimeters. A comparison with different replacement points along the electrode shows the best agreement at about 60% of the electrode length.

Beside penetrating electrodes, plate electrodes with galvanic or capacitive coupling are investigated where effects in the same order can be observed. However, a non-homogeneous resistivity distribution clearly increases the size of these effects, which is also demonstrated by sensitivity computation.

Apart from the ability of considering electrodes, CEM can be used to simulate the behaviour of a good conductor. It is shown exemplary how an injection through a borehole casing can increase a measured anomaly. Finally, an example of a buried vertical electrode chain is presented where CEM can be useful to calculate notable effects caused by the geometrical disturbances due to a drilling.

3.1. Introduction

Electrical resistivity tomography (ERT) is a popular geophysical technique since the electrical conductivity is a key parameter for many applications. The used scales range from a few centimetres in soil probe investigation (Binley et al., 1996; Igel, 2007) to some kilometres for large scale experiments. In geophysics, four-point measurements are mostly used in order to separate contact resistances from ground resistivity. It consists of inputting a current I through two electrodes C_1 and C_2 while registering a potential difference Δu between two other electrodes P_1 and P_2.

From a practical point of view, in most surface measurements steel sticks are plugged into the soil. If the soil cannot be penetrated (e.g., roads, hard rock) plate electrodes (Athanasiou et al., 2007) coupled galvanic or capacitively (Kuras et al., 2006) can be used. Ring electrodes are frequently used in borehole applications (Ridd, 1994). Sometimes even a steel borehole casing can be used for current injection (Daily et al., 2004). Lysimeters for soil investigation use small screws on the boundary. In all cases mentioned above, electrodes show a finite extend and the contact surface is part of the electrical system.

Figure 3.1a shows an equivalent electrical circuit for a four-point measurement that is commonly used in geophysics. It can be seen that the grounding resistors Z_{C_1} and Z_{C_2} only affect the amount of injectable current. Assuming a notable higher (compared to $Z_{\mathrm{Earth}_{i+1}}$) internal resistance of the measuring device, the grounding resistors Z_{P_1} and Z_{P_2} do not affect the measured voltage. However, this idealized view of a four-point measurement does not consider the physical presence of the electrodes.

The enhanced equivalent electrical circuit in Figure 3.1b takes into account the physical extension of the electrodes as well as their contact area to the surrounding material. Therefore, the cumulative grounding resistor Z is subdivided into a constant part Z_{E}, the electrode's grounding resistor, and Z_{C} the resistor caused by the contact area. Z_{E} is an intrinsic property of the electrode itself and depends only on the shape of the electrode, i.e., their surface area. Z_{E} is represented by the minimal potential surface during current injection. For simple electrodes shapes (spheres, ellipsoids) Z_{E} can be determined analytically (Militzer and Weber, 1985).

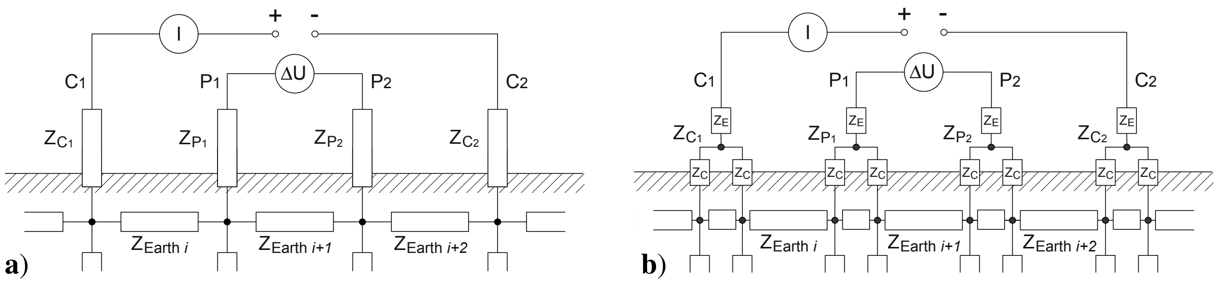

Figure 3.1.: **a**) Equivalent electrical circuit of a 4-point measurement used in DC resistivity measurements and **b**) including finite electrodes with contact resistance Z_{C}.

The contact resistor Z_C depends on the electrode surface area and the physical and electrochemical setting between the electrode and the surrounding material. In the sense of the equivalent electrical circuit, the injected current on the finite electrode flows through multiple contact resistors from the electrode into the ground in the vicinity of the electrode. Small contact resistors will therefore provide shortening circuits on parts of the ground, whereas high values for Z_C increase the overall contact resistance.

The presence of finite electrodes is largely neglected in geophysics. Modelling and inversion schemes use infinitely small injections, the point electrode model (PEM), i.e., a singular Dirac function for the current source within the modelling domain. Three expected effects are being ignored by PEM: (i) the spreading of the current density, (ii) the missing electrode volume from penetration, and (iii) the contact impedance influencing the local current flow and potential distribution around the electrode. So there are some questions to be answered:

- Up to which electrode size is a point assumption valid?
- Does the shortening caused by the contact impedance significantly affect the measurements?
- Which types of measurement arrays are affected most?

There are some electrode models in EIT literature that help to answer these questions.

The shunt electrode model (SEM) presented by Wang et al. (1999) allows the consideration of the electrodes extend and the shortening circuit due to a perfectly coupled electrode ($Z_C = 0$). It accounts for the real spatial extension by discretization of the electrode surface and forces the potential at the electrode surface to be equal.

A more sophisticated model, the so-called complete electrode model (CEM), was introduced in medical impedance tomography (EIT) by Cheng et al. (1989) and account for the electrode extend as well as the contact resistance Z_C by using a usually unknown contact impedance z.

The CEM formulation is briefly presented in the following as an extension of the Finite Element (FE) resistivity modelling described in Chapter 2. In order to verify the accuracy of the modelling, the results are compared with the analytical solution for an half-ellipsoidal electrode. The influence of the contact impedance and the electrode thickness are investigated by using two half-ellipsoids. Followed by a study on the influence of the electrode length on different electrode array types commonly used in geophysical ERT.

Several examples will show how the method is used for applications. Firstly, a model tank (lysimeter) of small dimensions is considered as a purely geometrical dependence. Secondly, the behaviour of plate electrodes and capacitively coupled line electrodes is investigated taking different contact impedances into account. In example three a borehole casing is used as a current electrode to improve the response of high conductive body which is modelled by a passive

CEM electrode. Finally, a vertical electrode chain with mounted ring electrodes is simulated which is used for monitoring ground water salinity.

3.2. The complete electrode model

The classical geoelectrical source term from equation (2.2) provides a singular current source but does not recognize the spatial extension of a physical electrode, e.g., the shape of a steel stick or any kind of electrode with a planar surface.

Assuming a highly conductive, e.g., metallic, surface of an electrode, the potential in the vicinity of the electrode surface appears to be constant as U. Cheng et al. (1989) provide an advanced boundary condition for an electrode boundary $\partial\Omega_{\mathrm{E}}$ to recognize this shorting or shunting effect and the finite electrode surface:

$$z\sigma\frac{\partial u}{\partial n}+u=U \quad \text{on} \quad \partial\Omega_{\mathrm{E}}\,, \tag{3.1}$$

as well as an additional current source condition (total current flow):

$$\int\limits_{\partial\Omega_{\mathrm{E}}} \sigma\frac{\partial u}{\partial n}\,\mathrm{d}s=I\,. \tag{3.2}$$

Equations (3.1) and (3.2) are called the complete electrode model (CEM) (Cheng et al., 1989). The usually unknown contact impedance $z[\Omega\,\mathrm{m}^2]$ between the electrode surface and the ground, caused by a very thin high resistive layer, has to be assumed since a pure shunting effect with $u=U$ on $\partial\Omega_{\mathrm{E}}$ would not provide a sufficient explanation practical EIT measurements (Cheng et al., 1989). Equation (3.2) describes an advanced current injection compared to the singular current equation (2.2) such that the current from the electrode flows through the entire electrode surface into the ground.

It is necessary to extent the previous finite element description (Sec. 2.2.1) to find a unique solution for the main DC equation (2.1a) including CEM (3.1, 3.2). The weak formulation of the DC resistivity forward operator can be obtained by applying the method of weighted residuals, partial integration followed by the specialization of the boundary condition with the CEM expression. Depending on arbitrary weighting functions w and $\mathcal{E}$ independent electrodes, the weak formulation can be read as:

$$\int\limits_{\Omega}\sigma\nabla w\nabla u\,\mathrm{d}\Omega+\int\limits_{\partial\Omega_{I}}\sigma\alpha wu\,\mathrm{d}\partial\Omega+\int\limits_{\partial\Omega_{E_l}}\frac{1}{z_l}wu\,\mathrm{d}\partial\Omega-\int\limits_{\partial\Omega_{E_l}}\frac{1}{z_l}wU_l\,\mathrm{d}\partial\Omega=0 \quad \text{for} \quad l=1\ldots\mathcal{E}\,. \tag{3.3}$$

Applying Galerkin's criterion $(w = N)$ leads to the finite element formulation:

$$\begin{aligned}
&\sum_{i=1}^{\mathcal{N}} u_{h_i} \left(\int\limits_{\Omega} \sigma \nabla N_i \nabla N_j \,\mathrm{d}\Omega + \int\limits_{\partial\Omega_I} \sigma \alpha N_i N_j \,\mathrm{d}\partial\Omega + \int\limits_{\partial\Omega_I} \frac{1}{z_l} N_i N_j \,\mathrm{d}\partial\Omega \right) \\
&- U_l \int\limits_{\partial\Omega_I} \frac{1}{z_l} N_j \,\mathrm{d}\partial\Omega = 0 \ \text{ for } \ j = 1 \ldots \mathcal{N}
\end{aligned} \tag{3.4}$$

with the additionally CEM source function:

$$\int\limits_{\partial\Omega_{\mathrm{E}_l}} \sigma \frac{\partial u}{\partial n} \,\mathrm{d}s = \int\limits_{\partial\Omega_{\mathrm{E}_l}} \frac{1}{z_l} (U_l - u) \,\mathrm{d}\partial\Omega = \sum_{i=1}^{\mathcal{N}} u_{h_i} \int\limits_{\partial\Omega_{\mathrm{E}_l}} -\frac{1}{z_l} N_i \,\mathrm{d}\partial\Omega + U_l \frac{1}{z_l} |E_l| = I_l \,. \tag{3.5}$$

The resulting system of equations reads:

$$\begin{aligned}
\mathbf{A}\mathbf{u} = \mathbf{b} \ \text{ with } \ \mathbf{A} = {} & \sum_{e=1}^{\mathcal{C}} \sigma^{(e)} \mathbf{S}^{(e)} + \sum_{b=1}^{\mathcal{B}_{\mathrm{I}}} \sigma \alpha^{(b)} \mathbf{M}^{(b)} + \frac{1}{z_l} \sum_{b=1}^{\mathcal{B}_{\mathrm{E}_l}} \mathbf{M}^{(b)} - \frac{1}{z_l} \sum_{b=1}^{\mathcal{B}_{\mathrm{E}_l}} \mathbf{l}^{(b)} \\
& - \frac{1}{z_l} \sum_{b=1}^{\mathcal{B}_{\mathrm{E}_l}} \mathbf{l}^{(b)^{\mathrm{T}}} + \mathrm{diag}_{\mathcal{N}+l} \frac{1}{z_l} |E_l|
\end{aligned} \tag{3.6}$$

$$\text{and } \ \mathbf{u} = [u_{h_i}, U_l] \,, \mathbf{b} = [b_i, I_l], b_i = 0 \ \text{ for } \ i = 1 \ldots \mathcal{N} \ \text{ and } \ l = 1 \ldots \mathcal{E} \tag{3.7}$$

and can be assembled from the known local element matrices $\mathbf{S}^{(e)}$, $\mathbf{M}^{(e)}$ and $\mathbf{l}^{(b)}$ described in Appendix A.

Note that the global system of equations (3.6), with the exception of the additional boundary condition for the inner surface, is equivalent to the result of the variational based description from Vauhkonen et al. (1999). An alternative approach to the finite element formulation that leads to an asymmetrical system of equations is described by Paulson et al. (1992). The system of equations (3.6) is solved by using the direct sparse Cholesky factorization package CHOLMOD (Chen et al., 2009). The resulting array **u** contains the potential distribution u_h for each node within the mesh as well as the sought potential values U_l for each electrode itself. The latter can be directly read and requires neither interpolation nor integration along the electrode surface.

The shapes of the electrodes used for medical EIT applications are limited to non-invasive flat surface pads, whereas in DC geophysics electrodes usually have a spatial extension and are plugged into the area of investigations. For the latter fortunately exists an analytical test case to validate the finite element solution.

3.3. Verification

The electrical field of an elliptical electrode is equal to the field of a line electrode with the length $2e$ which connects both foci (Sommerfeld, 1967). In analogy to the electrostatic problem of the electric field in the vicinity of a loaded elliptical object, the line source yields the following potential field (Militzer and Weber, 1985; Igel, 2007):

$$
\begin{aligned}
u &= \frac{I}{4\pi e} \ln \frac{z+e+\sqrt{x^2+y^2+(z+e)^2}}{z-e+\sqrt{x^2+y^2+(z-e)^2}} \\
\text{and}\quad e &= \sqrt{l^2-\frac{d^2}{4}}
\end{aligned}
\tag{3.8}
$$

with the potential u at distance (x,y,z) from an ellipsoidal electrode with the diameter d and the length l. The half-space solution for a half-ellipsoid at the surface is achieved by replacing 4π with 2π.

A half-ellipsoidal electrode with a length of $l = 0.5\,\mathrm{m}$ and a thickness $d = 0.1\mathrm{m}$ were chosen to verify the numerical approximation of the electrical field. It's true that these proportions may be too big and far from reality, but the example is suitable for evaluating the solution and studying the electrode effects as the problem is freely scalable.

To generate a suitable finite element discretization the 3D Delaunay mesh generator TetGen Si (2004) is applied. Initially, a set of piecewise coplanar facets is created in which the facets are connected via common nodes, the Piecewise Linear Complex (PLC), reflecting the geometry of the electrode. The PLC for the electrode is further subtracted from the main modelling domain. After applying the mesh generator the resulting mesh contains only elements of the modelling domain and the electrode surface, the inner electrode domain is not part of the problem and hence not discretized. If a valid PLC is given, this approach has no limitation to the complexity of the electrode shape.

For the verification test case a unit half-sphere ($d(x,y,z) = 1$ m) is created and scaled by $x,y = 0.1$ and $z = 0.5$. The main domain is represented by a cube with an edge length of $1000\,\mathrm{m}$ to avoid errors from the mixed boundary conditions that are based on a fixed point source position. Figure 3.2 shows a part of the resulting mesh boundary including the surface of the half-ellipsoidal electrode as well as parts of the earth's surface. The complete mesh contains 44 815 nodes, 31 025 quadratically shaped tetrahedrons and 3 858 boundary triangles.

Figure 3.3a shows the potential distribution with logarithmic equipotential lines. Due to the cylindrical symmetry a slice is chosen at the x-z-plane through the major axis of the ellipsoid. The dashed line corresponds to the point source solution $u = 1\mathrm{V}/2\pi$ at a distance of 1 m.

Figure 3.3b shows the numerical result compared with the analytical solution (3.8) for the ellipsoidal electrode shape within a homogeneous half-space along the probe line in Figure 3.3a.

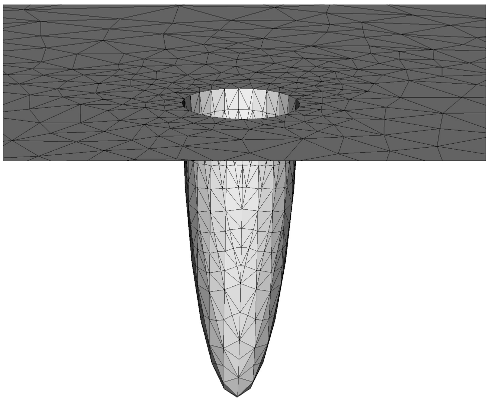

Figure 3.2.: Part of the mesh boundary with an ellipsoidal shaped electrode used for finite element modelling including CEM. Light grey triangle facets used for current injection (electrode), dark grey triangles represents the earth's surface with a homogeneous Neumann boundary condition.

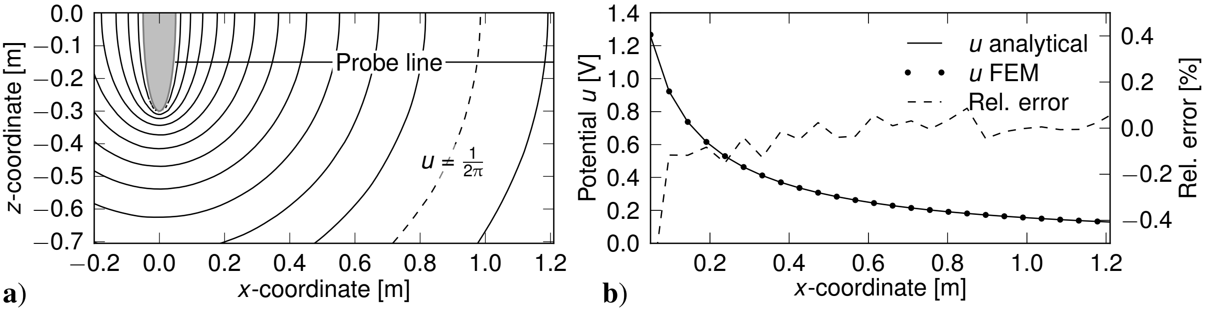

Figure 3.3.: **a**) Numerically calculated potential distribution for an electrode source with very low contact impedance. **b**) Direct comparison between the analytical solution for the ellipsoidal shaped electrode and the FEM solution along the probe line in (**a**).

There is a maximum misfit of 0.5% between the numerical and analytical solution close to the source electrode which is reduced to below 0.1% at a distance of 0.2 m. The comparison to the point source solution shows a difference of $\approx 2.4\%$ at the reference position $(x = 1.0, z = 0.0)$ for the layout given in Figure 3.3.

The effect of the contact impedance z can be studied by adding a second electrode. Figure 3.4 shows the potential distribution for two different values of z. Unfortunately the analytical solution is limited to a perfectly coupled source electrode, i.e., vanishing contact impedance, making only numerical comparisons available. The potential electrode with a low contact impedance (Fig. 3.4a) shows the electrode as a conductive inhomogeneity, whereas the high impedance in Figure 3.4b forces the potential lines to be orthogonal to the electrode surface as on the earth's surface or on a cavity.

The influence of the electrode can be quantified as an electrode effect $u_{\mathrm{CEM}}/u_{\mathrm{PEM}}$, comparable to the geometry effect in Chaper 2.6, as the ratio of the numerically calculated potential u_{CEM} using CEM and the potential u_{PEM} for a point source. This electrode effect can be expressed

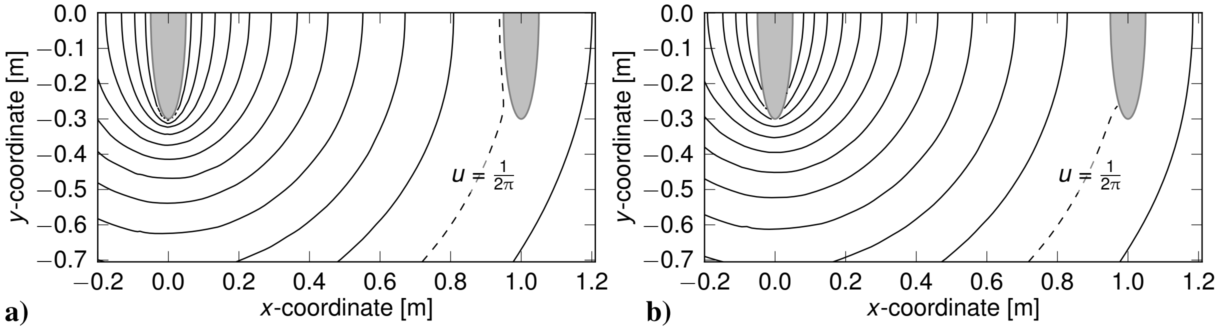

Figure 3.4.: **a**) Potential distribution for electrodes with low and **b**) high contact impedances.

by means of a trivial transformation as a percentage deviation in respect to u_{PEM}. The potential u_{PEM} can be calculated either analytically for some simple cases or numerically by using the conventional FEM approach.

Figure 3.5 shows the electrode effect for the electrode layout given in Figure 3.4 using two different electrode shapes and varying electrode diameters as a function of contact impedance. To get a generally valid comparison, unit values (1) are chosen for the distance between the electrodes, the background conductivity and the injected current.

For $z \to \infty$, i.e., without shunting on the electrode surface, the effect of both electrode shapes converges to the pure length effect and is about 5% and 7%. For high contact impedances the contribution of the electrode thickness to the effect seems to be very small. However, for small z a maximum contribution of d and z is about 3%. Surprisingly, there is a significant difference between the very similar sized electrode shapes caused by their contact angles that focus the

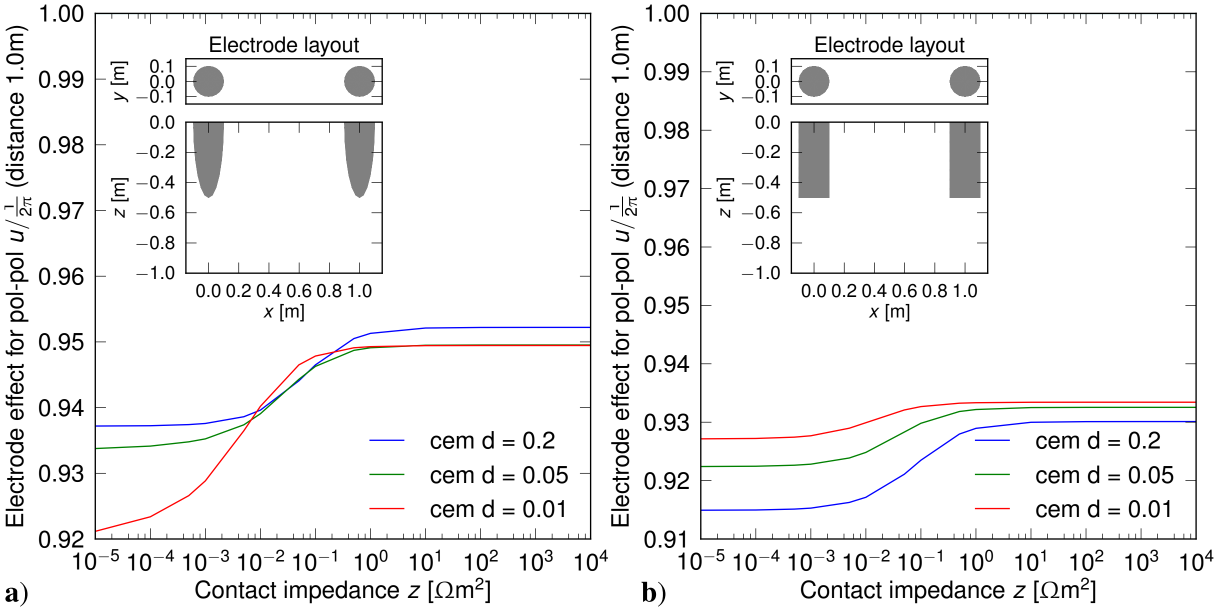

Figure 3.5.: Electrode effect for several electrode diameters and contact impedances for two different electrode shapes: **a**) ellipse and **b**) cylinder .

current. Whereas for a small d the electrode effect is maximized for the ellipse, it is minimized in case of the cylinder. The main change in contact impedance is between $Z = 0.01$ and $1\,\Omega\mathrm{m}^2$ for a homogeneous conductivity distribution of $1\,\Omega\mathrm{m}$.

For $z \rightarrow 0$ the effect converges to the perfectly coupled grounding resistance Z_E of the electrode. Therefore, a side-effect of the CEM solution is that Z_E within a homogeneous medium (σ_0) can be easily obtained for an arbitrarily shaped electrode (also systems of electrodes are possible):

$$Z_\mathrm{E}(\sigma_0) = \frac{U_l(\sigma_0, z_l)}{I_l} - \frac{z_l}{|E_l|} = \text{const for } E_l \tag{3.9}$$

with the potential $U_l(I_l)$, represented by the solution of (2.9) at electrode l with contact area $|E_l|$.

The contact impedance of an electrode may vary over time and cannot by directly determined by measurement (Heikkinen et al., 2002), thus a small uncertainty remains when simulating real measurements. Anyway, the effect of the contact impedance is small in comparison to the effect of the electrode shape itself, especially when assuming imperfectly coupled electrodes.

3.3.1. Influence on surface resistivity arrays

Practitioners might want to know how different electrode arrays are affected by finite electrodes. To answer this question, a line of 7 electrodes is considered using a spacing of 1 m suitable for 2 or 3 separations of the typical Wenner, dipole-dipole and pole-pole arrays. The electrode thickness is chosen to be 1 cm and the length is varied with the values of 10, 20, 30 and 40 cm. The electrodes are discretized by a prism with 8 segments and the contact impedance is defined to $z = 10^{-2}\,\Omega\mathrm{m}^2$.

Table 3.1 shows the results. Small but systematic effects can be found for an electrode size comparable to the spacing. A maximum effect of 11% and 8% is found for an electrode length of 0.4 m on the first separation using α and β type measurements, respectively. The effect vanishes rapidly for higher separations A rule of thumb can be derived, assuming the electrode length to be the plug-in depth of the steel sticks into the ground, so a plug-in depth of less than

Table 3.1.: Relative (negative) deviation of the CEM solution compared to the point solution (in %) for different electrode lengths and electrode arrays: Wenner-α (WA), Wenner-β (WB), dipole-dipole (DD) and pole-pole (PP). The number behind the array name denotes the separation factor.

Array	WA 1	WA 2	WB 2	DD 1	DD 2	DD 3	DD 4	PP 1	PP 2
$l = 0.1$ m	0.69	0.21	0.24	0.91	0.31	0.17	0.1	0.42	0.15
$l = 0.2$ m	2.5	0.68	0.89	3.3	1.2	0.64	0.41	1.4	0.42
$l = 0.3$ m	5.1	1.4	1.9	6.8	2.5	1.4	0.86	3	0.86
$l = 0.4$ m	8.3	2.4	3.2	11	4.3	2.3	1.5	4.9	1.4

20% to the electrode spacing should be a save choice to avoid systematic artefacts due to the electrode effect.

3.4. Examples

3.4.1. Model tank

ERT has been increasingly applied to investigate solute transport in porous media such as soils (e.g., Binley et al. (1996)). Either cylindrical or cubic lysimeters are used in which the soil is permanently installed. Electrode distances of a few centimetres are typical. So the relation of the electrode extend to the distance can be easily larger than for surface measurements. Furthermore, large geometry factors can occur since usually dipole-dipole measurements are applied using subsequently ordered electrodes. Up to now, only point electrodes have been considered. The electrodes have to possess a finite length and width to ensure a proper current injection and coupling for potential measurements.

A unit lysimeter of size $1 \times 1 \times 1\,\mathrm{m}^3$ is simulated to describe the influence of extended electrodes. The electrodes, 3 cm long and 1 cm thick, are mounted at the four vertical sides of the cube. The spacing between the electrodes is 20 cm, starting 10 cm from the boundary for all directions such that in total $4 \times 5 \times 5 = 100$ electrodes have been simulated. Every electrode is discretized by a regular prismatic cylinder with 8 segments. Figure 3.6 combines the input for the mesh generator with the electrodes as regular prisms orthogonal to the outer faces and the resulting mesh, which was obtained by TetGen (Si, 2004) using a quality constraint of 1.25 and comprised 346 868 nodes within 239 045 quadratic tetrahedrons.

For comparison reasons, a second tank model was created with point sources at the outer surfaces. According to Chapter 2.5.2, a local refinement of 1 cm at the electrodes was applied and quadratic shape functions were used. This resulted in a mesh of 136 219 nodes and 92 543 cells. A further refinement achieved almost identical results.

Figure 3.7 shows a logarithmic histogram of the obtained electrode effect for a complete dipole-dipole dataset containing 4 753 values. The maximum distribution occurs at an effect of $\pm 1\%$, i.e., both solutions are nearly identical within measuring accuracy. However, there is a significant number of deviations, both increases and decreases. The relative differences range from -57% to $+1214\%$, the standard deviation is 25.4%. More than 70% of the data show a deviation of less than 1%. However, there are a few outliers that are mainly related to dipoles crossing the electrode planes which show high absolute geometric factors. About 2% of the data are differ more than 10% in each direction. Deleting data with absolute geometric factors above 1 000 m entails a loss of 5% of the data, but effects between -44% and $+11\%$ remain with a standard deviation of only 2.8%.

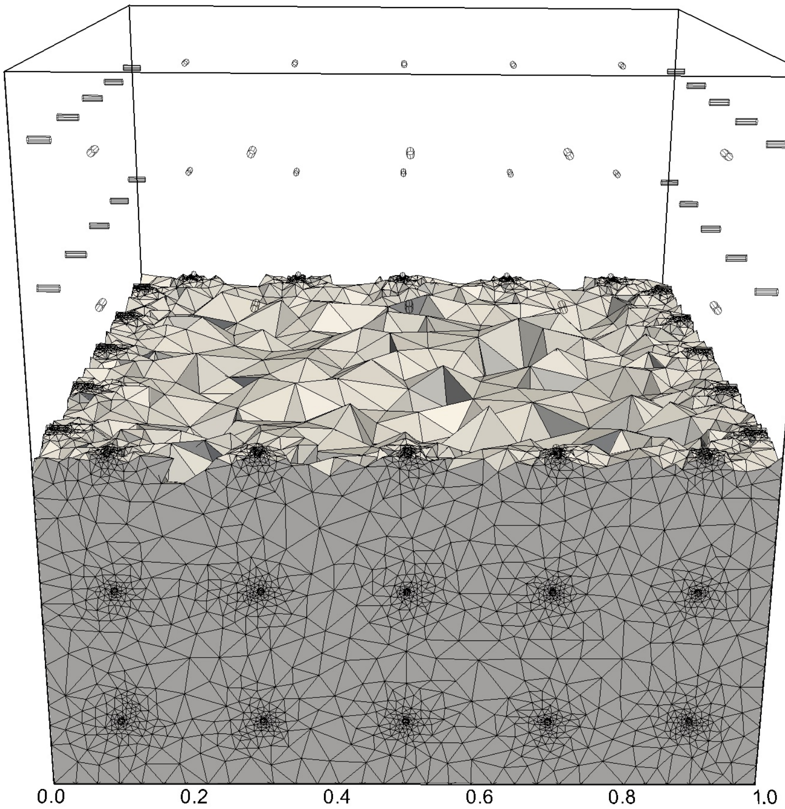

Figure 3.6.: Piece wise linear complex (upper half) and parts of the resulting mesh (lower half) of the tank model. The cylindrical electrodes are approximated by regular prisms with 8 side segments.

It could be argued that the point on the surface is not the perfect position for an equivalent replacement point source. For comparison, the replacement nodes were placed on different distances δx from the boundary along the axis of the electrode. Table 3.2 shows how the CEM solution can be approximated by these different point locations.

If only geometric factors $k < 1000$ m are considered, the best values, below 1%, are obtained for the intermediate positions between 50% and 66% of the electrode length. However, there are still errors above 10%. Note that whereas for the complete data the biggest absolute differences move towards the negative deviations, they seem to move towards the positive for the filtered data. Therefore, a replacement approximation point should be placed at about 60%. However, the behaviour suggests that systematic, albeit small, electrode effects are still being not considered by the replacement approach.

The previous study was carried out using large contact impedances ($z > 10^6$) to avoid the shunting effect. A computation with $z = 10^{-6}$ yields results very close to those with high z except for a few critical values with large geometric factors. For two values even the sign of the simulated values changed. This can happen, if the measured dipole is nearly parallel to the equipotential lines.

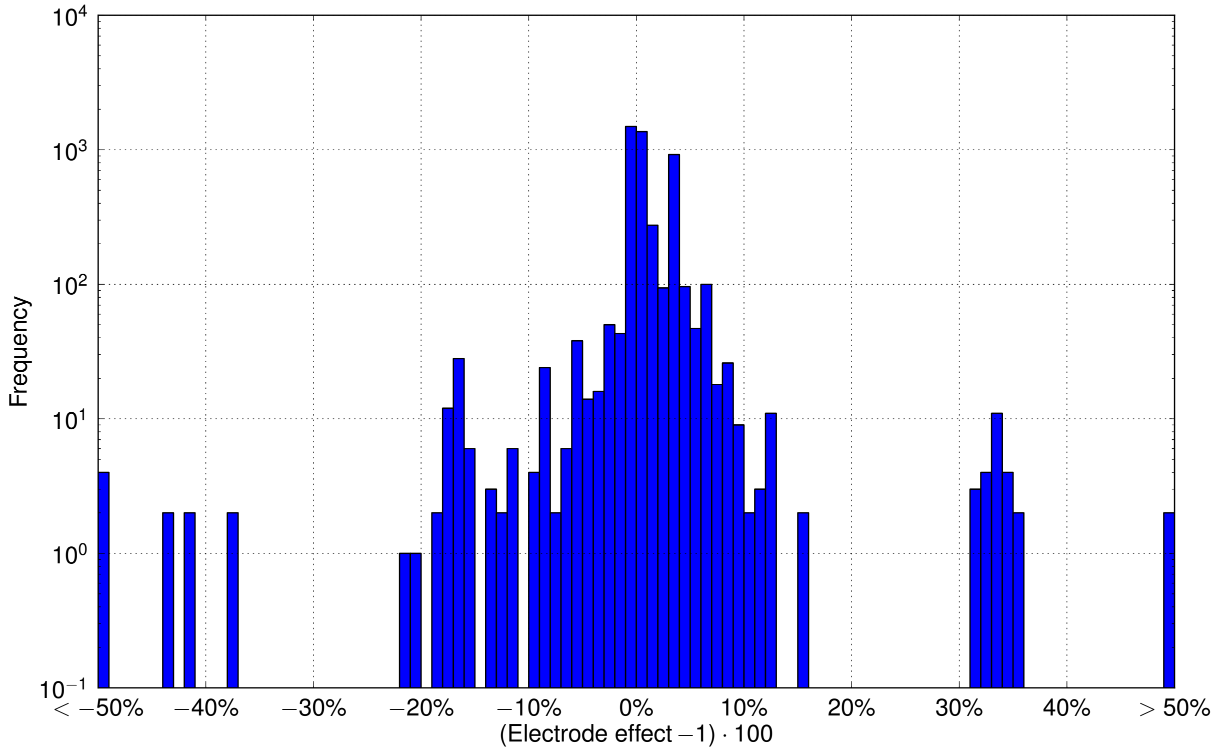

Figure 3.7.: Logarithmic histogram of the geometric effect in %, i.e., the distribution of the deviation between CEM and point solution, for the tank model.

Table 3.2.: Minimum, maximum and standard deviation of point source error (in %) for different replacement positions of the point along the electrode axis. All data (left) and geometric-factor corrected data with $|k| < 1000$ m (right).

	Complete data			Filtered data		
δx in %	min	max	std	min	max	std
0	-56.8	1214.4	25.4	-43.6	11.0	2.8
33	-39.2	843.6	17.6	-29.9	7.6	1.9
50	-17.2	373.1	7.7	-12.6	3.4	0.8
66	-290.6	13.8	6.1	-2.6	11.7	0.7
100	-2192.4	101.0	45.7	-19.6	79.0	4.7

Reliable results as a first order approximation are most probably obtained by an inversion with appropriate replacement point source positions, particularly if differences in time are regarded. However, since the remaining deviations are systematic, artefacts are still expected to appear. Note that the presented spacing between the electrodes are still rather big. If the spacing are $a = 10$ cm or less, or if bigger electrodes or other arrays are being used, then the CEM effects must be considered in the inversion process. As experience showed, the effects are smaller for cylindrical lysimeters, however large geometric factors can occur as well.

3.4.2. Plate-shaped electrodes

For obvious reasons non-penetrating pad electrodes are the electrodes of choice for medical EIT measurements. While in geophysical resistivity surveys generally stainless steel sticks are preferred, there are also several cases in which plate electrodes are applied (Pagliara and Vignoli, 2006; Athanasiou et al., 2007). A simulation of a dipole-dipole sounding above a two-layer case is performed to investigate how such plate electrodes affect measurements. The first layer thickness of 0.5 m equals half of the electrode spacing. The reference solution was obtained analytically (Telford et al., 1976).

Figure 3.8 shows the electrode effect for a dipole-dipole sounding using a fixed electrode spacing (1 m) between 13 quadratic plate electrodes. The plate length ($e = 0.1$, 0.25 and 0.5 m) as well as the resistivity contrast between the two layers are varied ($1/10, 1/1, 10/1$). While the dimension for electrode extent and spacing are scalable the effects remain equal. Each model is calculated with a high ($z_i = 100\,\Omega\mathrm{m}^2$, Fig. 3.8a–c) and a low ($z_i = 10^{-5}\,\Omega\mathrm{m}^2$, Fig. 3.8d–f) contact impedance.

Investigating Figure 3.8b (homogeneous conductivity distribution and no shunting effect due to high contact impedance) a maximum electrode effect of 5% can be found for the first dipole-dipole separation with plates extending to half of the electrode spacing. The effects for smaller electrodes can nearly be neglected. However, Figure 3.8a and c show quite different results for the heterogeneous models, e.g., up to 14% for the large plates with the resistive layer below the array. To the contrary, a conductive first layer reduces the electrode effect drastically.

The behaviour of the effects differ otherwise by considering the shunting effect (Fig. 3.8c–e) caused by a low contact impedance. For the homogeneous model as well as for the higher resistive first layer, a maximum effect at the 2nd separation of up to 30% can be found. The reason for this is the shortening effect of the unused electrode between the source and the transmitter dipole that significantly disturbs the electrical field.

The notable differences of the electrode effects for heterogeneous models can be expressed by the sensitivity function which is based on the current density distribution (Geselowitz, 1971). Hence, a simple correction of the apparent resistivity using a pre-calculated electrode effect can be misleading. The sensitivity distribution has to be considered for the inversion of the measured data using larger plate electrodes. However, unless the plate electrodes extend to more than 20% of the electrodes spacing the assumption of point like electrodes should be sufficiently accurate.

According to Kuras et al. (2006), a capacitively coupled line electrode can be regarded as an equipotential surface for static or slowly varying electrical fields. Besides the excellent resistivity mapping capability of such capacitive resistivity measurements such data should be evaluated using modern inversion strategies. Due to the fact that a suitable inversion code is not available that is able to recognize line electrodes geometry, a replacement point approximation

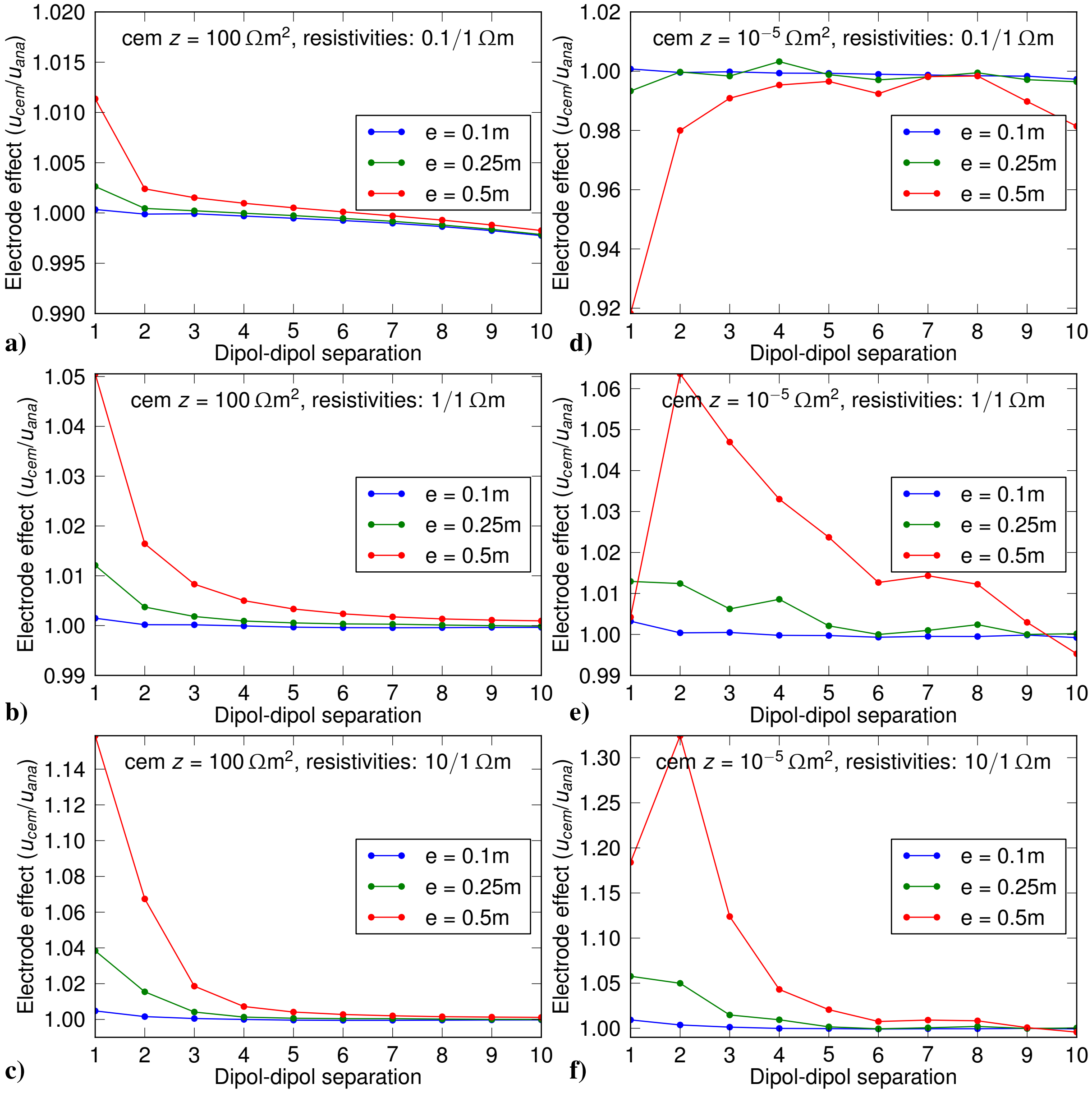

Figure 3.8.: Electrode effect for a dipole-dipole sounding using square plate electrodes with varying plate length e above a two-layer case with a 1st layer thickness 0.5 m. The left column (**a**,**b**,**c**) uses a high contact impedance ($z = 100\,\Omega\mathrm{m}^2$) and the right column (**d**,**e**,**f**) a low contact impedance ($z = 10^{-5}\,\Omega\mathrm{m}^2$). The resistivity ratio changes row-wise from 0.1/1 Ω m, 1/1 Ω m to 10/1 Ω m.

for the line antennas are suggested at the outer ends of the line (Geometrics, 2001), the centre of each line (Kuras et al., 2006) or at 80% (Neukirch and Klitzsch, 2010). However, the sensitivity distribution remains unattended. Neukirch and Klitzsch (2010) tried to simulate the sensitivity response for such a line array by super-positioning a huge amount of point sources along the electrode extent.

Assuming a non-galvanic contact to the ground, such capacitive electrodes may be simulated by using CEM plate electrodes with high contact impedance. Simulating a line electrode dipole-

dipole array using CEM plate electrodes with a size of 0.95×0.01 m, the geometric factor equals less than 1% with the analytical values from Kuras et al. (2006). The sensitivity can be easily calculated numerically using the element stiffness matrices and the potential distribution obtained from the FEM modelling (cf. Sec. 4.4.2).

Figure 3.9 shows the potential distribution and the electric current paths for a injection dipole using CEM line electrodes with low (a) and high (c) contact impedance as well as for point electrodes (e). The potential distribution between point and line mainly differs directly below the electrodes. The shortening effect for the electrodes with low contact impedance (Fig. 3.9a) can be clearly seen where the current is partially forced to flow into the passive electrodes.

The shortening nature of the perfectly coupled line electrode produces large differences in sensitivity (Fig. 3.9b) compared to the non-shunting line or the point electrode. Considering capacitive coupling for inversion, the differences in sensitivity between high contact impedance and point source are relevant. The area of negative sensitivity is smaller and the contrast of the sensitivity near the electrodes is smoother for the line electrode. A notable difference is the change of sign below the electrode. For the point source the change of sign matches the electrode position whereas for the line electrode there is no symmetry. This may result in a lack of accuracy by using a fixed replacement point approximation for the inversion of capacitive line electrode data, particularly for shallow structures.

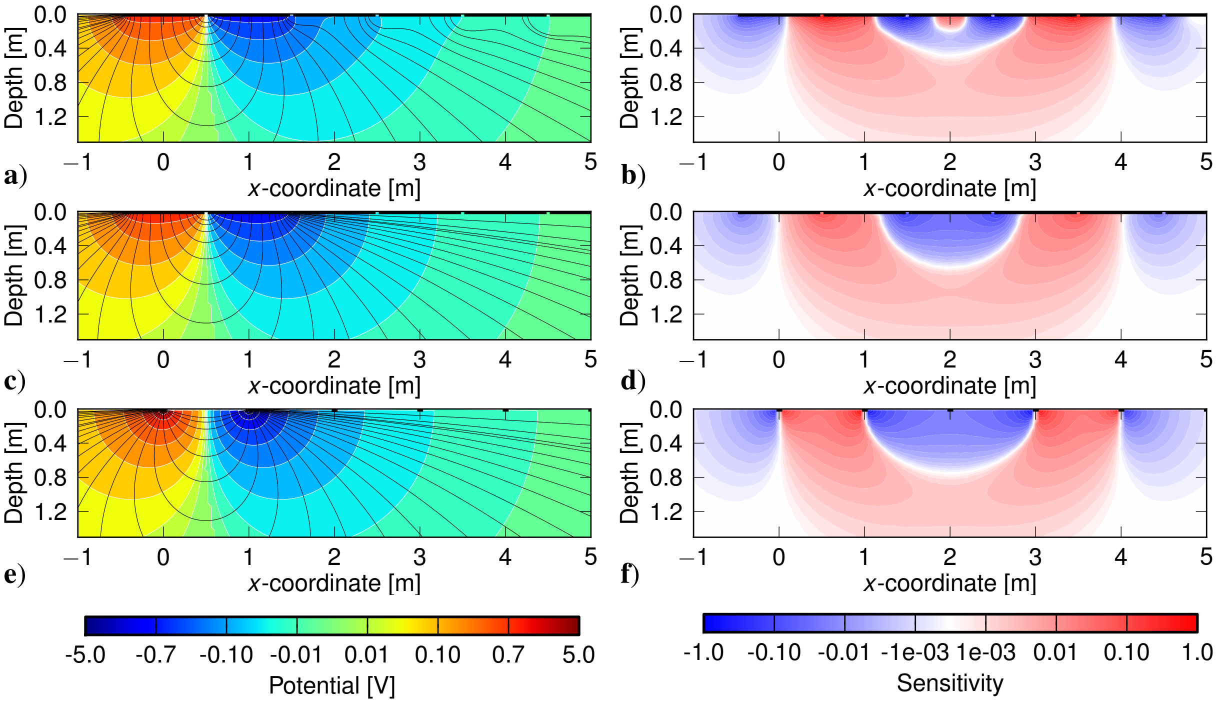

Figure 3.9.: Potential distribution (left) and sensitivity function (right) for a dipole-dipole array using line electrodes with low (**a**,**b**) and high (**c**,**d**) contact impedances and point electrodes (**e**,**f**). The lines (left) represent the current path, and the black lines at the surface denote the electrodes extend.

3.4.3. Modelling a good conductor with CEM

As seen before, in case of a small contact resistance a passive electrode behaves as good conductor. This can be used to avoid discretization problems and inaccuracies at the resistivity contrast of a conventionally discretized conductivity model. In the following example, a conductive body ($10 \times 200 \times 50$ m, rotated 45°) is assumed about 100 m below a current injection, e.g., this could be an ore body, graphite or a water-filled fault. Pole-dipole measurements are simulated with 10 m electrode spacing and a surrounding resistivity of 100 Ωm.

Figure 3.10a shows the potential distribution and the current paths from a point source. The latter are drawn into the good conductive body and disturb the potentials measured at the surface. As a result the influence of the body to the apparent resistivity of a dipole registration (Fig. 3.10b) is about $\approx 4\%$ and is thus close to the measuring accuracy. Furthermore, the minimum is very broad and far from injection and body.

Additionally to the passive electrode, a steel casing of a 150 m deep borehole (diameter 0.2 m) is assumed as a CEM electrode and used for current injection. The potential (Fig. 3.10b) in the

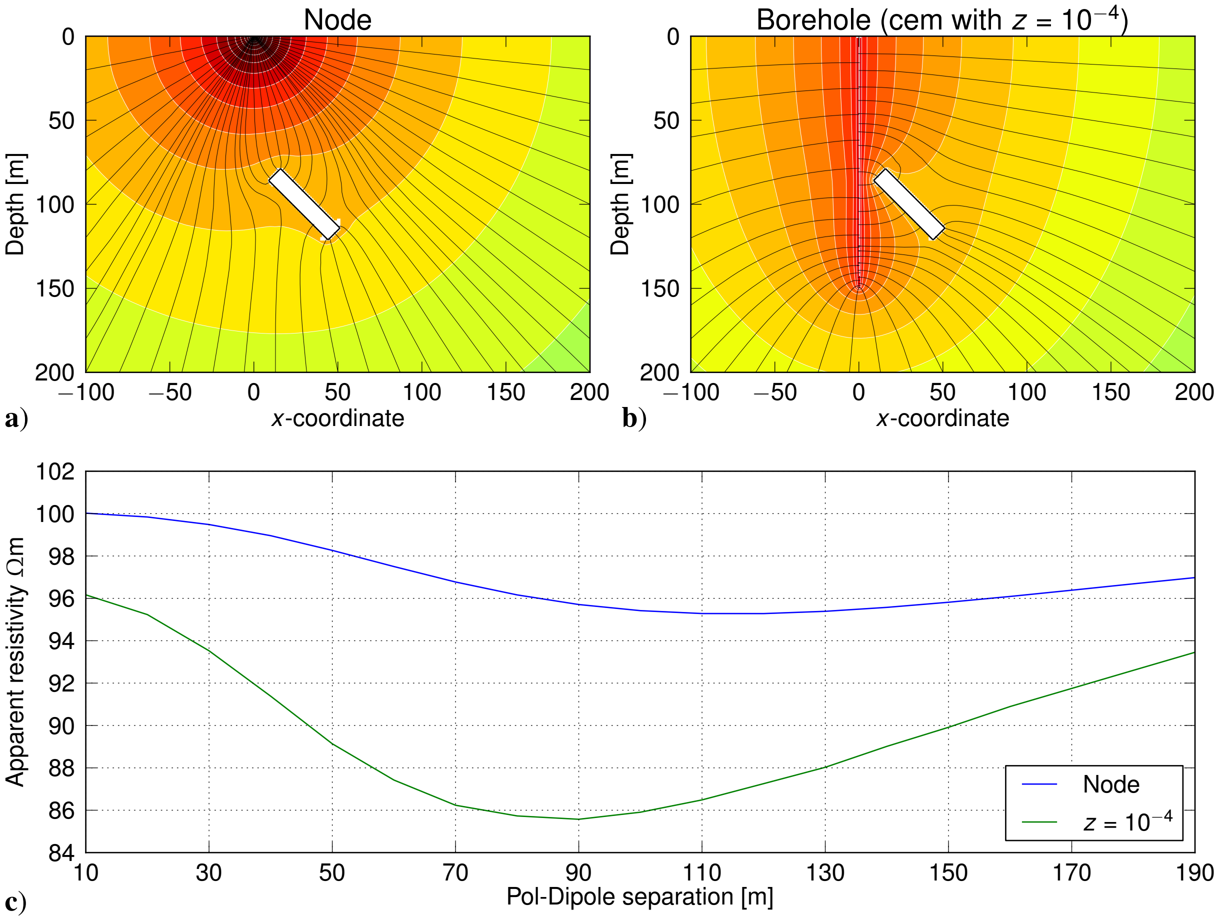

Figure 3.10.: Logarithmically spaced equipotential lines (white) and current paths (black) for **a**) a point source and **b**) for injecting the current into a borehole casing. **c**) Apparent resistivity of a pole-dipole sounding using both variants.

vicinity of the borehole is smaller due to the increased surface area and thus decreasing the current density. On the other hand, the potential is significantly bigger at greater depth and distance. The conductor, now in a region with a higher potential, changes the potential distribution of the whole subsurface. Consequently, the resulting apparent resistivity curve (Fig. 3.10c) shows a much bigger anomaly. Note that the geometric factors needed for the apparent resistivity values are calculated with the same electrode layout but omitting the passive body.

3.4.4. Vertical electrode chain

Surface ERT measurements are often unable to image slight changes in resistivity at greater depths. To monitor the salt/fresh-water boundary on a North Sea island, so-called vertical electrode chains were installed (Südekum et al., 2010). The whole is a combinable plastic cylinder with a 48 mm diameter. In a distance of 25 cm metal take-outs are mounted with a width of 25 mm. There are two significant differences to point electrodes in the full-space: Firstly, the electrodes are extended but only to 10% compared to the spacing. Secondly, the plastic void, where the cables are situated, cannot be used by the current to flow.

Additionally to the deep installed variant with $a = 0.25$ m, a shallow variant with a spacing of $a = 0.1$ m is considered for the monitoring of water saturation in the vadose zone. Usual geoelectric measuring configurations can be applied. A mesh was generated with an appropriate cylindrical borehole and 7 ring electrodes that are adapted by regular prisms with 12 segments. The inside of the electrodes and the drilling holes were defined such that homogeneous Neumann boundary condition are applied on the cylinder boundary. Figure 3.11 displays a section of the mesh used for the computation. It consists of 74 493 nodes and 53 403 tetrahedrons.

Table 3.3 shows the deviation to the point source solution for different electrode arrays for an undisturbed modelling domain. All simulated voltages are below the point source solution. The effect is surely bigger for small separations and slightly bigger for β than for α type measurements. For the deep variant effects of up to 7% occur, whereas for the shallow variant deviations of more than 17% can be observed.

The extension of the electrodes surface is small compared to the electrode spacing. According to the results of the plate-shaped electrodes example no notable contributions from the electrode shape to the results in Table 3.3 are expected, hence the main contribution to the effect stems

Table 3.3.: Relative (negative) deviation of CEM solution compared to point solution (in %) for electrode arrays Wenner-α (WA), Wenner-β (WB), dipole-dipole (DD), and pole-pole (PP). The number behind the array name denotes the separation factor.

Array	WA 1	WA 2	WB 2	DD 1	DD 2	DD 3	DD 4	PP 1	PP 2
a=0.25 m/d=48 mm	5.2	1.9	2.4	7.0	3.2	1.9	1.3	3.2	1.1
a=0.10 m/d=40 mm	14.5	7.2	8.8	17.2	10.3	7.2	5.6	10.5	5.1

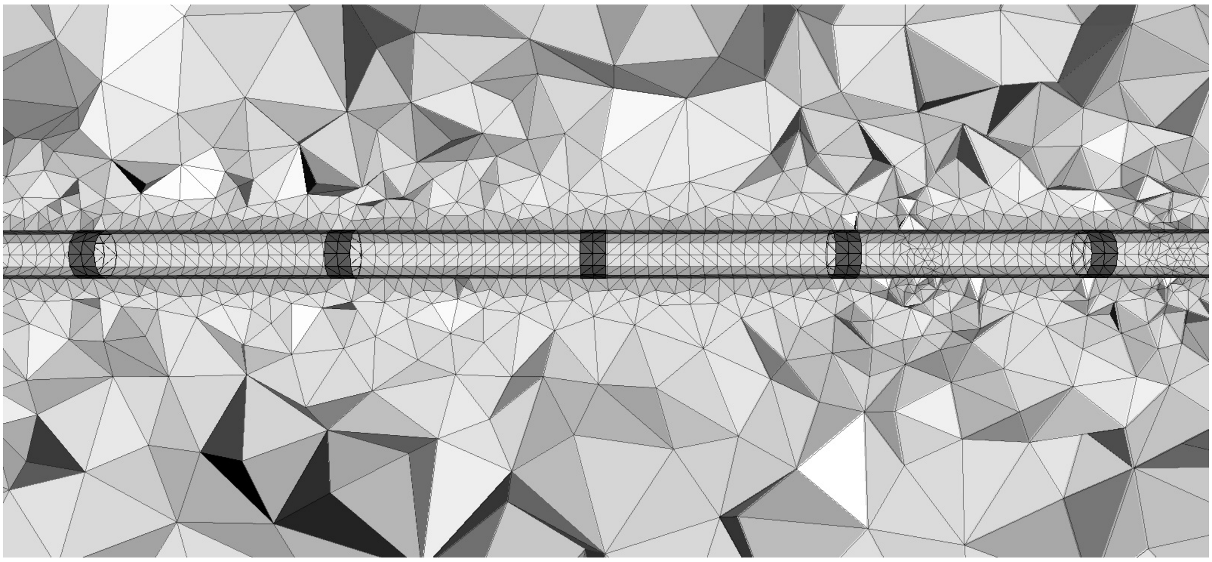

Figure 3.11.: Section of the mesh through the axis of the simulated vertical electrode chain. The dark grey cylinder pieces show the mesh discretization of the electrodes, and the plastic tube is situated in-between.

from the drilling hole. However, CEM is essential for a realistic simulation of such drilling effects, because using point electrodes instead (i.e., mounted at the boreholes boundary) will break the cylinder symmetry.

3.5. Conclusions

The complete electrode model (CEM) is a useful extension to the DC resistivity forward problem that is able to account for finite extend and contact impedance of electrodes by additional equations. The implementation into a finite element discretization allows for the computation of arbitrarily shaped electrodes.

Electrodes can play three roles: (a) active current injection, (b) measuring potentials over the whole electrode surface and (c) they can act as high conductive bodies within the potential field. The accuracy of the presented approach was proved by comparing the potential field of an ellipsoidal shaped electrode as for (a) with the analytical solution from the electrostatic equivalent problem that neglects (b) and (c). Therefore, the latter is only valid for a vanishing contact impedance and only for measuring point potentials. However, from a point of quality the calculated potential and current distribution are plausible.

In order to quantify the effect an electrode effect is defined as the ratio between CEM and the point solution or its percentage deviation. The contact impedance plays a subordinate role for all considered four-point measurements over a wide range of magnitudes. However, it is of utmost importance for the potential disturbance in role (c).

For surface resistivity arrays the electrode length becomes practically interesting only for electrode lengths/spacing> 0.2, e.g., for small-scaled soil measurements. The effects can significantly increase if measurements on closed objects such as soil probes are considered which can exhibit large geometric factors.

As alternative to sticks, non-penetrating plate electrodes with galvanic or capacitive coupling can also be simulated using CEM. The effects are generally very low even for large plate sizes. As for penetrating electrodes a ratio of electrode extend/spacing > 0.2 is the limit where the electrode effect can be larger as the accuracy of up-to-date measuring devices. However, the effects increase when considering an inhomogeneous resistivity distribution which is also illustrated by the sensitivity function.

Apart from the ability to consider finite electrodes for ERT, CEM with low contact impedance allows for the simulation of good conductive bodies. A synthetic experiment shows that if boreholes are used for current injection, anomalies can be amplified. The vertical electrode chain example shows that even if the pure electrode effects can be neglected, CEM can be useful to calculate notable effects of a geometrical disturbance due to a drilling.

The meshes used in this section obtain a huge number of nodes since they were created fine enough to avoid numerical problems and ensure accuracy. The discretization of electrodes, e.g., by cylinder segments, represent a substantial additional cost with regard to modelling preparation and leads to increased numerical effort due to additional elements. However, due to the finite electrode surface the singularity of the point current source is avoided and can possibly be treated by just moderate refinement. That opens up a couple of possible solutions to incorporate CEM into inversion which can be easily done using the triple-grid scheme presented in Chapter 4.

A first-order solution can be to avoid the effort of a CEM discretization. The lysimeter example shows a replacement point source for a penetrating electrode at about 60% of the electrodes cylinder axis may be a sufficient approximation for data with moderate geometric factors. However, experience from the plate electrode example shows that there can be a strong dependency on the conductivity distribution. As second-order solution is the use of a primary mesh containing CEM, thus a more accurate primary potential can be incorporated. The probably most accurate third-order solution would be incorporating the CEM electrodes into the inverse mesh as well and thus incorporating sensitivity calculation that depends on CEM. An example is given in Chapter 5.3.4

The presented technique is a very general solution and could be used for a wide range of applications where point approximations are not accurate enough. For example, sample holders for lab measurements can be computed. Borehole resistivity tools could be calibrated and designed but additional equations for focusing conditions would have to be implemented. A main improvement of the technique could be achieved by incorporation of complex resistivity to account for

IP effects. A realistic simulation should incorporate a Warburg type contact impedance but laboratory studies of electrodes and the coupling effect are needed for realistic assumptions. Much stronger effects on the phases can be expected, particularly for varying contact impedance.

Part II.

Inversion

4. Inversion on unstructured meshes

Abstract

A novel technique is presented for the determination of resistivity structures associated with arbitrary surface topography. The approach represents a triple-grid inversion technique that is based on unstructured tetrahedral meshes and finite element forward calculation. The three grids or respectively meshes are characterized as follows: A relatively coarse parameter mesh defines the elements whose resistivities are to be determined. On the secondary field mesh the forward calculations in each inversion step are carried out using a secondary potential approach. The primary fields are provided by a one-time simulation on a highly refined primary field mesh at the beginning of the inversion process. A Gauss-Newton method is used with inexact line search to fit the data within error bounds. A global regularization scheme is applied using special smoothness constraints. The regularization parameter is determined by compromising data misfit and model roughness by an L-curve method and is finally evaluated by the discrepancy principle. To solve the inverse subproblem efficiently, a least squares solver is presented.

The technique is applied to synthetic data from a burial mound to demonstrate its effectiveness. A resolution-dependent parametrization helps to keep the inverse problem small to cope with memory limitations of today's standard PC's. Furthermore, the secondary potential calculation reduces the computation time significantly. This is a crucial issue since the forward calculation is generally very time-consuming. Thus, the approach can be applied to large-scale three-dimensional problems as encountered in practice which is finally proved on field data.

4.1. Introduction

The direct current (DC) resistivity method gains information about subsurface conductivity structures by injecting electric currents into the ground and measuring electric voltages at different locations. Since the measured data do not provide the desired information directly, inversion techniques have to be formulated to reconstruct the spatial distribution of conductivity.

Although uniqueness has been proved by Druskin (1998), the inverse DC resistivity problem is generally ill-posed with respect to data errors and incomplete data sets.

While initially resistivity soundings used to be applied to determine horizontal layers of varying conductivity, nowadays profile measurements using pre-installed multi-electrode lines are state of the art to investigate two-dimensional (2D) structures. However, many objects of investigation exhibit three-dimensional (3D) features which limit a 2D interpretation.

As a result of the development of modern field equipment it is now possible to obtain several thousands of data per day. Thus, a target area can be covered by large electrode arrays or a large number of parallel profile lines to make feasible 3D investigations. Fortunately, computer facilities and numerical techniques are developing rapidly as well, allowing for the development and application of 3D modelling and inversion software.

Three-dimensional inversion of resistivity data is non-linear and usually solved in an iterative process that applies a forward modelling routine for nearly arbitrary resistivity distributions in every inversion step. The forward operator is generally obtained by finite difference (FD) or finite element methods (FE). The 3D FE forward operator presented in Chapter 2 is used as the forward operator for the modelling in the following. The calculation of the secondary potential may be carried out on coarse meshes which is particularly advantageous for the inversion. However, the reference primary potential must be determined once. This is obtained most efficiently on a locally refined unstructured mesh using quadratic shape functions, which represents the initial point of the inverse approach described here.

The first three-dimensional inversion scheme was published by Park and Van (1991) followed by Ellis and Oldenburg (1994); Zhang et al. (1995); Loke and Barker (1996b). Most of the inversion schemes are based on Gauss-Newton techniques, some avoid the storage of the Jacobian matrix (Zhang et al., 1995). In contrast, Ellis and Oldenburg (1994) introduced a non-linear conjugate gradient method, see also Zhdanov and Keller (1994). In all these approaches the model parameters are represented by orthogonal grids and the forward calculation is carried out using finite differences.

The first inversion scheme using a finite element forward calculation was presented by Sasaki (1989, 1994). However, like Brecque et al. (1995); Yi et al. (2001); Pain et al. (2003), they use structured grids of rectangular block orientation even if blocks are decomposed into tetrahedrons. There are very few references to unstructured tetrahedral meshes (Sugimoto, 1999). Zhdanov (2002) gives an overview on existing approaches.

In the following, a full 3D DC resistivity inversion scheme is presented, that involves three different unstructured tetrahedral meshes and is able to deal with arbitrary surface topography. It is shown that the parametrization can be adopted to the resolution properties of the inverse problem. Thus, the number of model parameters can be reduced significantly to save computing time and memory.

4.2. Motivation

One of the main problems to deal with is the mesh transformation between the inverse and the forward procedure. On the one hand, the parametrization mesh has to be relatively crude to limit the degrees of freedom and the ill-posedness of the inverse problem. On the other hand, the forward calculation requires a very fine mesh to provide sufficiently accurate results. In order to save computing time, the secondary potential (SP) technique has to be used for which the primary potentials are needed. If topography is present, those can only be assessed by numerical modelling on a highly refined mesh. However, this work has to be done only once in the beginning of the inversion. These considerations lead to the triple-grid technique as presented in the following.

The formulation of the mixed boundary condition for the solution of the geoelectrical forward problem (2.1) requires boundaries at the modelling domain that are generally far from the sources and parameter contrasts. This is often accomplished by adding cells of increasing size toward the boundaries. In contrast to the forward modelling mesh, the model parameters are usually represented in a parameter mesh restricted to the neighbourhood of the sensors. Its number of cells, i.e., the degrees of freedom, must not be too large due to limitations in run time and computer memory since the Jacobian matrix is dense. At best, the appropriate element size should be defined by the physical resolution. Resolution measures can be obtained by resolution analysis as pointed out by Friedel (2003). In summary, the meshes of the parameter representation and the forward calculation are connected by a refinement and prolongation operation (Fig. 4.1). The primary field mesh is independent of these but locally refined at the electrodes positions.

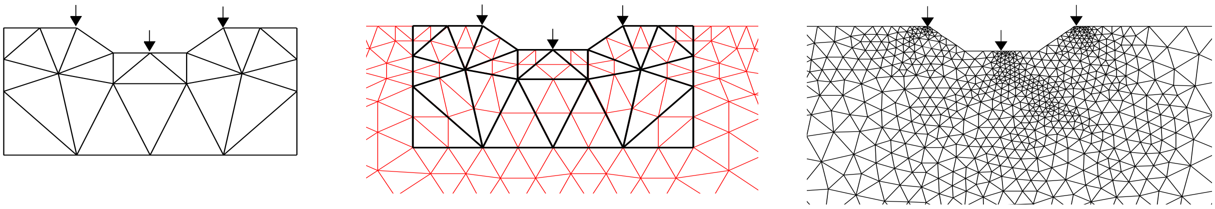

Figure 4.1.: The three meshes of inversion for a two-dimensional discretization: parameter mesh (left), secondary field mesh (centre) and primary field mesh (right). Arrows indicate the position of the electrodes.

4.3. The three meshes

The three meshes needed in the inversion procedure are constructed with respect to the input parameters. The mesh generation itself is a very complicated procedure. Therefore TetGen (Si, 2004) is applied, a non-commercial and flexible software for the generation of tetrahedral meshes.

The **parameter mesh** describes the cells whose resistivities are to be determined and includes the topography of the target area. The lateral model extension is determined by the electrode layout plus a small surrounding region in the dimension of several electrode spacings. To determine the model depth, the idea of Roy and Apparao (1971); Barker (1989) is extended to multi-electrode data. A 1D-sensitivity function for a homogeneous half-space is calculated and summed up for all data. A cumulative value of 90% depicts a reasonable model depth and can be applied to arbitrary electrode configurations (Günther, 2004). As an advantage of unstructured meshes their element size can be varied flexibly. An a-priori resolution analysis (Friedel, 2003) helps to get an idea of resolution radii as a function of space. Thus, the smallest elements appear near the electrodes and have typical edge lengths of $0.5-1$ times the electrode distance. The element size increases with depth such that the largest elements are created at depth or near the boundaries and have extensions of several electrode distances.

On the **secondary field mesh** the forward calculations are carried out for the secondary potential. It is obtained through a global $h-$refinement of the parameter mesh. To avoid effects of the boundary conditions, a mesh prolongation has to be applied. Additional boundaries are suggested with the size of a few times the electrode layout are suggested.

The **primary field mesh** is used to calculate the primary potentials as needed for the SP technique. A constant conductivity of $\sigma = 1\,\mathrm{S/m}$ is assumed and the potential is scaled with the individual value of σ_0. To cope with the large potential gradients, the mesh needs to be highly refined near the electrode positions to obtain accurate results. Additionally, higher order polynomial shape functions are used. This also increases the degrees of freedom but turns out to be more effective than purely spatial refinement (cf. Section 2.5.2). Consequently, the primary field mesh usually has a huge number of nodal points but the associated system of equations has to be solved only once at the beginning of the inversion process. The primary potential values for the related nodes of the secondary mesh are obtained by interpolation according to the FEM base functions of the primary mesh.

4.4. Inversion scheme

4.4.1. The objective function

A Gauss-Newton scheme with global regularization is used as described in the following. Let $\mathbf{m}$ be the model vector of $\mathcal{M}$ single model parameters $\mathbf{m} = (m_1, m_2, \dots, m_{\mathcal{M}})^{\mathrm{T}}$. The individual m_j denotes the physical properties of the individual tetrahedrons or a function of it. To ensure positivity of the resistivities ρ_j, the logarithms $m_j = \log \rho_j$ are used

In the same manner the logarithms of the measured apparent resistivities $\log(\rho_{\mathrm{a}_i}) = d_i$ are used to build up the data vector of $\mathcal{D}$ single data $\mathbf{d} = (d_1, d_2, \dots, d_{\mathcal{D}})^{\mathrm{T}}$. Each data is associated with an error ε_i, which is used for weighting. Using an ℓ_2-norm of the weighted residual between data and model response $\mathbf{f}(\mathbf{m}) = (f_1(\mathbf{m}), f_2(\mathbf{m}), \ldots, f_{\mathcal{D}}(\mathbf{m}))$ obtained by the forward operator, the data functional Φ_d to be minimized is defined by

$$\Phi_d(\mathbf{m}) = \sum_{i=1}^{\mathcal{D}} \left| \frac{d_i - f_i(\mathbf{m})}{\varepsilon_i} \right|^2 = \|\mathbf{D}\left(\mathbf{d} - \mathbf{f}(\mathbf{m})\right)\|_2^2 \quad \text{with} \quad \mathbf{D} = \operatorname{diag}\left(1/\varepsilon_i\right).$$

If the errors are not measured, they have to be estimated appropriately. Following Friedel (2003) the errors are assumed to be composed of a percentage error of several $(p)\%$ and a voltage error δU,

$$\frac{\delta\rho_a}{\rho_a} = p\% + \frac{\delta U}{U} \,. \tag{4.1}$$

Note that the use of logarithmic apparent resistivities ρ_a leads to the error estimate $\varepsilon_i = \log(1 + \delta\rho_{\mathrm{a}_i}/\rho_{\mathrm{a}_i})$ for $i = 1 \ldots \mathcal{D}$ (Friedel, 2003).

Since the minimization of Φ_d represents a highly ill-posed problem, a regularization is imposed by introducing an additional model functional Φ_m (Tikhonov and Arsenin, 1977). It is weighted by the regularization parameter λ yielding the functional to be minimized

$$\Phi = \Phi_d + \lambda \Phi_m \rightarrow \min \,. \tag{4.2}$$

Equation (4.2) can also be obtained by the minimization of Φ_m while fitting the data down to the error level $\Phi_d^* = N$. Thus, the regularization parameter has to be chosen to satisfy $\Phi_d = \Phi_d^*$.

Φ_m is a squared norm of a product of a constraint matrix $\mathbf{C}$ and the difference between the model $\mathbf{m}$ and a reference model $\mathbf{m}^0$

$$\Phi_m(\mathbf{m}) = \|\mathbf{C}(\mathbf{m} - \mathbf{m}^0)\|_2^2 \,. \tag{4.3}$$

From here two ways are possible: If $\mathbf{m}^0$ is a model containing a-priori information and $\mathbf{C}$ is the identity or a diagonal weighting matrix, the model is kept close to $\mathbf{m}^0$. The other way is to treat $\mathbf{m}^0$ as a constant vector and to use $\mathbf{C}$ to control the model characteristics. Since the problem is highly under-determined and the measurements are usually carried out at the surface, the application of smoothness constraints (Constable et al., 1987; de Groot-Hedlin and Constable, 1990) seems to be the method of choice. Both methods may also be combined, e.g., if a layered half-space is given as reference model $\mathbf{m}^0$ and the inhomogeneities are expected to be smooth.

For a regular mesh the smoothness matrix $\mathbf{C}$ represents a discrete approximation of a partial differential operator of first or second order. Here, special smoothness constraints for an unstructured mesh have to be defined taking into account the neighbouring relations. Two tetrahedrons i and j are referred to being neighbours, if they share a common triangle face. For each face f $C_{f,i} = -1$ and $C_{f,j} = +1$ are set, instead of 1 the face area size may be inserted. Thus, $\mathbf{C} \in R^{B \times \mathcal{M}}$ is a sparse matrix with $2\mathcal{M}$ entries, where $\mathcal{B}$ is the number of boundaries.

The model vector is updated in an iterative procedure,

$$\mathbf{m}^{k+1} = \mathbf{m}^k + \tau^k \Delta\mathbf{m}^k \,, \tag{4.4}$$

with the line search parameter τ^k, the superscript denotes the iteration number.

The application of the Gauss-Newton scheme on minimizing Φ leads to (Park and Van, 1991)

$$\begin{aligned} \left(\mathbf{S}^{\mathrm{T}}\mathbf{D}^{\mathrm{T}}\mathbf{D}\mathbf{S} + \lambda\mathbf{C}^{\mathrm{T}}\mathbf{C}\right)\Delta\mathbf{m}^k &= \mathbf{S}^{\mathrm{T}}\mathbf{D}^{\mathrm{T}}\mathbf{D}(\mathbf{d} - \mathbf{f}(\mathbf{m}^k)) \\ &- \lambda\mathbf{C}^{\mathrm{T}}\mathbf{C}(\mathbf{m}^k - \mathbf{m}^0) \,, \end{aligned} \tag{4.5}$$

where $\mathbf{S}$ is the Jacobian matrix.

4.4.2. Sensitivity calculation

The sensitivity or Jacobian matrix $\mathbf{S} \in R^{\mathcal{D} \times \mathcal{M}}$ contains the partial derivatives of the model responses f_i with respect to the model parameters m_j

$$S_{i,j}(\mathbf{m}^k) = \frac{\partial f_i(\mathbf{m}^k)}{\partial m_j} \,. \tag{4.6}$$

There exist several methods to obtain sensitivities or Frechet derivatives (McGillivray and Oldenburg, 1990). Sensitivity studies have been extensively carried out to obtain concepts of detection and resolution properties. Spitzer (1998) described sensitivities for various configurations and gave an overview on methods for the numerical calculation.

From the reciprocity theorem by Geselowitz (1971) can be derived an analytic expression for the sensitivity of the impedance Z with respect to a conductivity change $\delta\sigma$

$$\delta Z = -\delta\sigma \iiint\limits_{\Omega_i} \frac{\nabla u^S}{I^S} \cdot \frac{\nabla u^R}{I^R} \,\mathrm{d}^3 r \,, \tag{4.7}$$

where Ω_i is the anomalous region. u^S is the potential caused by the source electrodes and u^R is the one obtained from interchanging source and receiver electrodes. The corresponding currents are denoted by I^S and I^R.

The potential gradients are known from the finite element forward simulation and are constant within each element for linear shape functions. In the following the formulation of Kemna

(2000) is adapted, going back to Sasaki (1989)

$$\frac{\partial u}{\partial \sigma^{(e)}} = -\frac{1}{\sigma^{(e)} I} \sum_i \sum_j S_{i,j}^{(e)} u_i^S u_j^R \,,$$

in which the sensitivity is obtained by summation over the potentials and the entries in the element stiffness matrix $\mathbf{S}^{(e)}$ that is introduced in Chapter 2.2.1

However, problems arise for elements adjacent to electrode positions. The infinite potential on this node has to be replaced by a finite one to restrict the sensitivity values. Note also that the formulation approximates the potential by piecewise linear functions, which is satisfying for the secondary but not for the total potential on the moderate secondary field mesh.

In the course of iterations, the sensitivity matrix can be recalculated. Alternatively, quasi-Newton methods may be applied that use a rank-one update mechanism (Broyden, 1972). Since the difference is negligible, Broyden's method is used in the following examples to save computing time.

4.4.3. Solution of the inverse subproblem

The system of equations (4.5) has to be solved in every iteration step. In contrast to ray tomography the matrix **S** is dense. For large-scale problems it is sometimes useful to neglect small absolute values to represent **S** as a sparse matrix.

To avoid the storage of the left-hand side matrix and the transpose of the Jacobian, conjugate gradient techniques are used for solving equation (4.5) approximately. The presented algorithm denoted as CGLSCD is an adaptation of the CGLS algorithm (Press et al., 1992) introducing data weighting and model constraints (Günther, 2004). For the solution of

$$(\hat{\mathbf{S}}^{\mathrm{T}}\hat{\mathbf{S}} + \lambda \mathbf{L})\mathbf{x} = \hat{\mathbf{S}}^{\mathrm{T}}\mathbf{b} - \lambda \mathbf{L}\delta\mathbf{x}$$

it reads in the initialization ($\mathbf{x}_0$ - initial guess)

$$\mathbf{z}_0 = \mathbf{b} - \hat{\mathbf{S}}\mathbf{x}_0$$
$$\mathbf{p}_0 = \mathbf{r}_0 = \hat{\mathbf{S}}\mathbf{z} - \lambda \mathbf{L}\delta\mathbf{x}$$

and computes in every iteration $k+1$

$$\begin{aligned}
\mathbf{q}_k &= \hat{\mathbf{S}}\mathbf{p}_k \\
\alpha_{k+1} &= \left\|\mathbf{r}_k\right\|^2 / (\mathbf{q}_k^{\mathrm{T}}\mathbf{q}_k + \lambda \mathbf{p}_k^{\mathrm{T}}\mathbf{L}\mathbf{p}_k) \\
\mathbf{x}_{k+1} &= \mathbf{x}_k + \alpha_{k+1}\mathbf{p}_k \\
\mathbf{z}_{k+1} &= \mathbf{z}_k - \alpha_{k+1}\mathbf{q}_{k+1} \\
\mathbf{r}_{k+1} &= \hat{\mathbf{S}}^{\mathrm{T}}\mathbf{z}_{k+1} - \lambda \mathbf{L}(\mathbf{x}_{k+1} + \delta\mathbf{x}) \\
\beta_{k+1} &= \left\|\mathbf{r}_{k+1}\right\|^2 / \left\|\mathbf{r}_k\right\|^2 \\
\mathbf{p}_{k+1} &= \mathbf{r}_{k+1} + \beta_{k+1}\mathbf{p}_k
\end{aligned}$$

until the residual vector $\mathbf{r}_k$ falls below a given limit. In every occurrence, $\hat{\mathbf{S}}$ is replaced by $\mathbf{DS}$, the vector $\mathbf{b}$ is initialized with $\mathbf{D}(\mathbf{d}-\mathbf{f}(\mathbf{m}^k))$, $\delta\mathbf{x} = \mathbf{m}^k - \mathbf{m}^0$ and $\mathbf{L} = \mathbf{C}^{\mathrm{T}}\mathbf{C}$. The result is the sought model update $\Delta\mathbf{m}^k$. Note that all scalars and vectors may be overwritten in each iteration. The only exception is to save $\left\|\mathbf{r}_k\right\|^2$ before $\mathbf{r}_{k+1}$ is computed. A further improvement may be achieved by preconditioning (Haber, 2005).

4.4.4. Choice of the regularization parameter

The regularization parameter λ is a trade-off between data fit and model roughness and must therefore be chosen accordingly. Small values lead to highly rough-textured models with good data fit, whereas large values correspond to smooth models with weak data fit (Tikhonov and Arsenin, 1977). There exist several methods to compromise data fit and model constraints (Farquharson and Oldenburg, 2004). A very simple but not always stable method is referred to as L-curve method ((Hansen and O'Leary, 1993), see Vogel (1996) for instabilities). By plotting the data misfit Φ_d against the model roughness Φ_m for a series of λ_i a curve is constructed, which has often an L-shaped appearance. Figure 4.2 shows such an L-curve as arising from the first synthetic example of Chapter 4.5.1. A reasonable trade-off between Φ_d and Φ_m occurs near the 'corner'. The location may be determined, e.g., by estimating the curvature Li and Oldenburg (1999).

Since the system is better conditioned for strong regularization, the solving of equation (4.5) is starting using a relatively large λ and decrease it successively by a fixed factor until the curvature of the L-curve begins to decrease again. This point indicates the optimum λ. Since solutions $\Delta\mathbf{m}$ corresponding to neighbouring λ_i yield similar results, the result for one value of λ is used as starting vector $\mathbf{x}_0$ for the next smaller value. This reduces the number of iterations in the CGLSCD algorithm drastically (Frommer and Maass, 1999). In order to construct the global L-curve, the forward responses are needed for all values of λ. To avoid this, the L-curve is investigated of the linearised inverse problem.

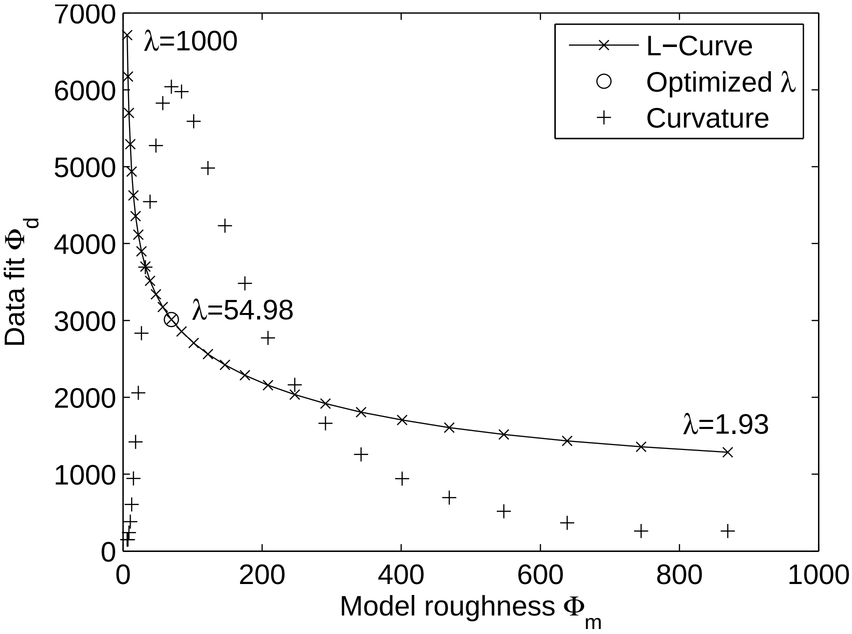

Figure 4.2.: L-curve (data fit against model roughness) derived from the synthetic example of Chaper 4.5.1. The optimum regularization strength may be determined searching the maximum of the curvature.

Note that finally the discrepancy principle (fitting data within error bounds) dictates the regularization strength. However, in non-linear inversion many runs would be necessary to iterate until $\Phi_d = \Phi_d^*$. On the other hand, data errors are seldom known accurately and have to be estimated. In practice, values of 1 to 5 for the chi-squared misfit $\chi^2 = \Phi_d/\mathcal{D}$ show reliable results without over-fitting or under-fitting the data.

4.4.5. Line search

In each iteration the step length parameter τ^k has to be determined to prevent the model from overshooting due to non-linearity. Initially, the forward response is computed for the full step length $\mathbf{f}(\mathbf{m}^k + \Delta\mathbf{m}^k)$. To avoid the forward calculation for many values τ_i^k, a linear interpolation is used between the old and the new model response

$$\mathbf{f}(\mathbf{m}^k + \tau\Delta\mathbf{m}^k) \approx \tilde{\mathbf{f}}(\tau) = \mathbf{f}(\mathbf{m}^k) + \tau[\mathbf{f}(\mathbf{m}^k + \Delta\mathbf{m}^k) - \mathbf{f}(\mathbf{m}^k)]\,,$$

which is a poor approximation but sufficient to obtain an appropriate step length Günther (2004). The parameter τ^k is determined such that $\Phi_d(\tilde{\mathbf{f}}(\tau)) + \lambda\Phi_m(\tau))$ is minimized. Then, the model is updated $\mathbf{m}^{k+1} = \mathbf{m}^k + \tau^k\Delta\mathbf{m}^k$ and the forward response $\mathbf{f}(\mathbf{m}^{k+1})$ is calculated exactly. Thus at least two forward runs are needed per iteration step.

4.4.6. Triple-grid inversion scheme

Figure 4.3 displays the inversion scheme. The following steps are passed through:

1. Read data & topography, estimate errors
2. Triangulate topographical surface
3. Generate parameter mesh by resolution estimates
4. Generate secondary field mesh by prolongation and global refinement
5. Generate primary field mesh
6. Calculate primary potentials for $\sigma = 1$ and interpolation to the secondary mesh nodes
7. Determine geometric factors and apparent resistivities
8. Choose starting model and constraints

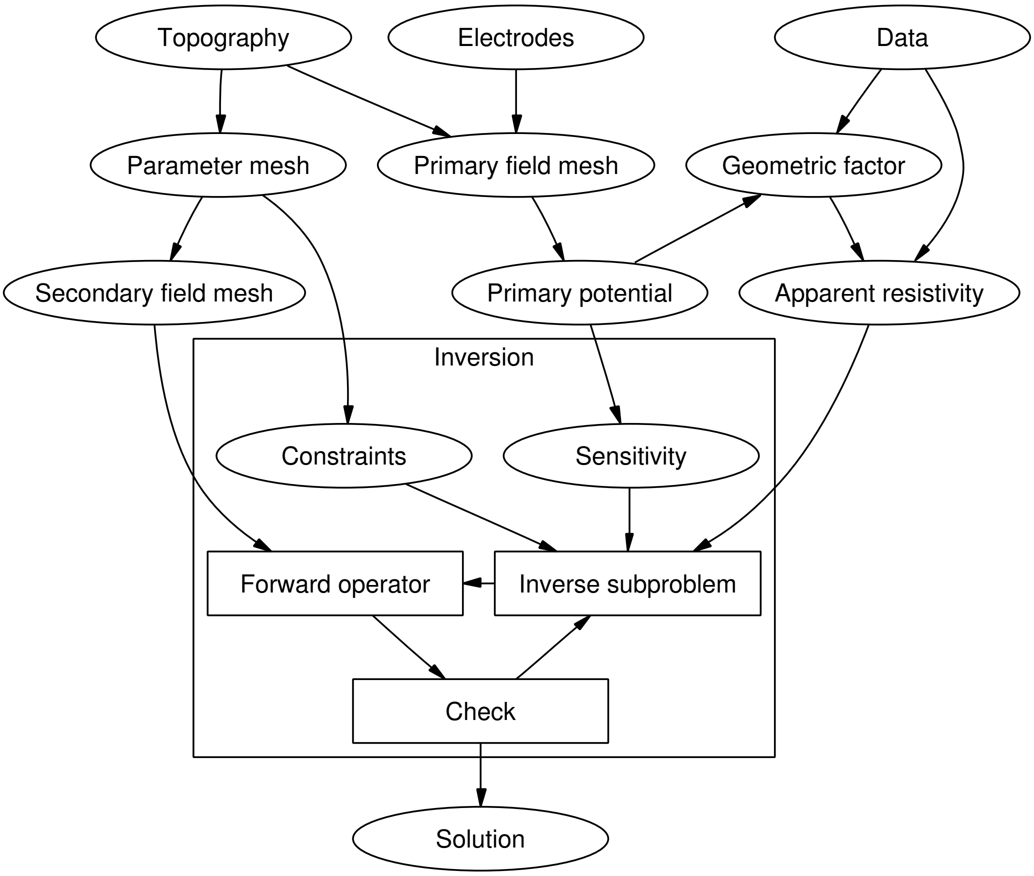
Topography
Electrodes
Data
Parameter mesh
Primary field mesh
Geometric factor
Secondary field mesh
Primary potential
Apparent resistivity
Inversion
Constraints
Sensitivity
Forward operator
Inverse subproblem
Check
Solution

Figure 4.3.: Inversion scheme. The topography is used to build the meshes. The primary potential defines the geometric factors and thus the apparent resistivities. The forward calculation is carried out on the secondary mesh. The frame indicates the central loop of the forward and inverse step until the stopping criterion is reached and a solution is obtained.

9. Approximate Jacobian matrix from potential
10. Calculate model update vector by solution of equation (4.5), use L-curve criterion to determine λ at a first step
11. Determine step length by inexact line search
12. Update model and calculate forward response
13. Repeat last four steps until the stopping criterion is fulfilled

The stopping criterion applies if (a) the functional Φ stagnates or (b) the data are fitted within errors, i.e. $\chi^2 = \Phi_d/N \approx 1$. If necessary, the regularization parameter λ may be adjusted and the inversion is continued.

4.5. A synthetic example

4.5.1. Synthetic model and data

The following example is derived from the investigation of a burial mound and illustrates the flexibility of handling a complicated geometry. The topography is built up by intersection of an ellipsoid with a plane. Its footprint is an ellipse of 20×15 m extent, the top of the mound is located 5 m above ground level. It is shown in the following, that the steep topography, particularly at the foot of the slopes, affects the direct current measurements severely and cannot be neglected in the inversion process.

Figure 4.4 shows the topography and the electrode layout. 9 profiles are placed in x-direction and 13 profiles in y-direction. The electrode distance is 1 m on all profiles, the profile distance is 2 m. 487 electrodes are used in total.

The mound itself is supposed to have a resistivity of 200 Ωm whereas for the underground 100 Ωm are assumed. Additionally, a cavity inside the mound is considered. It has an ellipsoidal shape with half-axes of 1.5, 1.0 and 0.5 m in x, y and z direction, respectively, and is described by Neumann boundary conditions. Its centre is located 2.5 m below the top of the mound. Figure 4.5 shows the synthetic model and the mesh used for calculating the synthetic data. The positions of the electrodes are clearly indicated by the high refinement. According to Chapter 2.5.2 quadratic shape functions are used on a mesh with 634 242 nodes to calculate the synthetic data.

Dipole-dipole configurations are considered on all profiles. To counteract the growing geometric factor and redundancy, the dipole lengths are enlarged with increasing separation factor n. In fact, the dipole length is calculated by $\Delta e = (n + 3 \bmod 4)a$, where a is the initial dipole length and $n = 1, 2, 3,$ etc. A total of 3 439 single data is simulated. The synthetic data are noisified

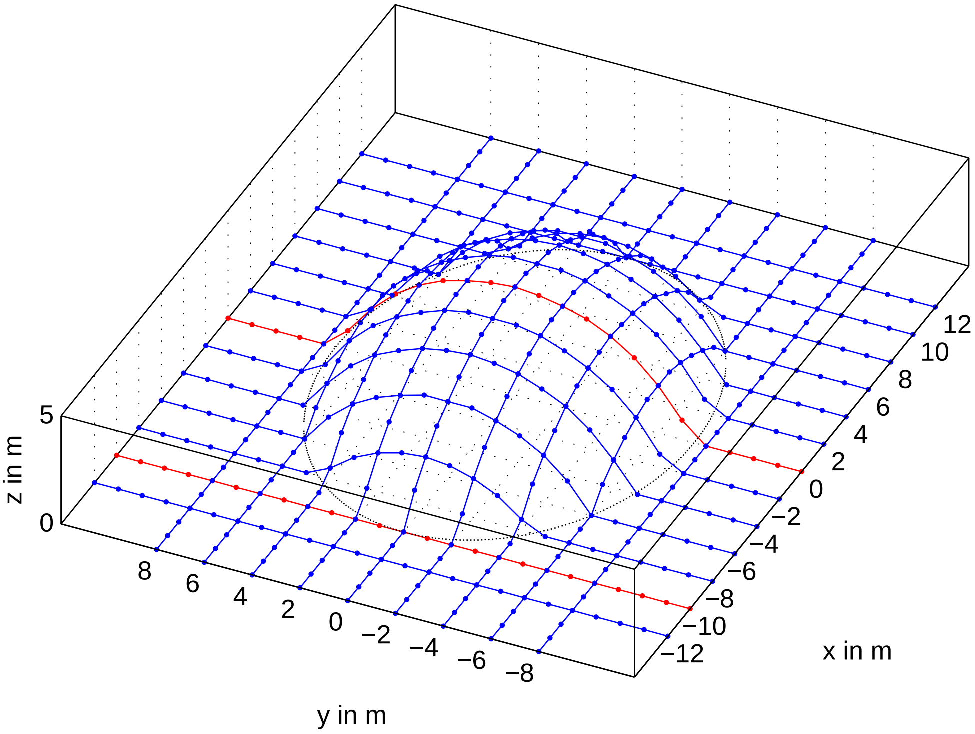

Figure 4.4.: Topography and electrode layout of the synthetic example. The two red profiles will be discussed in the following.

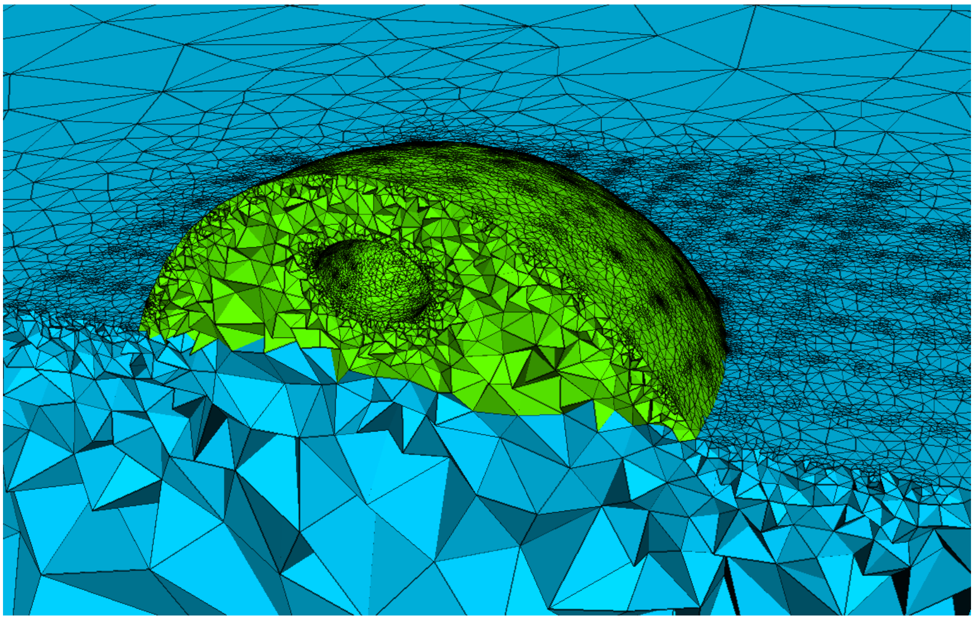

Figure 4.5.: Synthetic model of a burial mound of 200 Ωm over a homogeneous half-space of 100 Ωm. An ellipsoidal cavity is located in the centre of the mound.

with Gaussian random values. According to equation (4.1), a standard deviation is used of 3% plus a voltage-dependent noise of 100 μV at an assumed current of 100 mA for both noise and weighting. The two profiles at $x = 0$ m and $x = -10$ m are further investigated in the following.

4.5.2. Geometry effect

The influence of the topography on the response along the example profiles is shown in Figure 4.6. Note that this is done only for illustration since the geometric factors are known due to numerically calculation. The wrong flat-earth geometric factors are used for the calculation of the apparent resistivities ρ_a (Figure 4.6a) on purpose. Strong anomalies can be seen both in the profile aside the mound (top) as well as in the central profile (bottom), which are mostly caused by the topography as can be seen right away.

To eliminate the geometry effects, the real geometric factors were derived from the primary potentials. The effects are very strong and produce an increase as well as a decrease in the apparent resistivity of a factor of 3 to 4. The mound shows up with increased apparent resistivities at the central part of the profile, whereas decreased values are indicated at the slopes. Compared to the raw data in (Fig. 4.6a) nearly identical structures can be seen. Hence, the data are dominated by the geometry effect.

Using the simulated geometric factor the data can then be transformed such that the geometry effect is removed (Fig. 4.6c). The remaining anomalies can be clearly associated with the parameter structure. In the central part of the central profile (Fig. 4.6c bottom) the pseudo-section shows the resistivity of the mound (200 Ωm), whereas the data at both ends of the profile represent the background resistivity of 100 Ωm. Additionally, the high-resistive cavity can be clearly observed in the data by isolated high resistivities in the central part.

4.5.3. Inversion result

An automated mesh generation is used merely based on the topographical information. The meshes created in the following are independent of the one used for producing the synthetic data set in Chapter 4.5.1 to avoid an inverse crime (Wirgin, 2004). The parameter mesh contains 23 109 parameter cells whose resistivities are to be determined. The secondary field mesh obtains 112 040 nodes and the primary field mesh 421 157 nodes so that the first one may be solved directly by Cholesky decomposition and the latter iteratively by conjugate gradients.

Figure 4.7 shows the parameter mesh and the secondary field mesh. The primary field mesh is similar to the one shown in Figure 4.5 but lacking the cavity and therefore not shown.

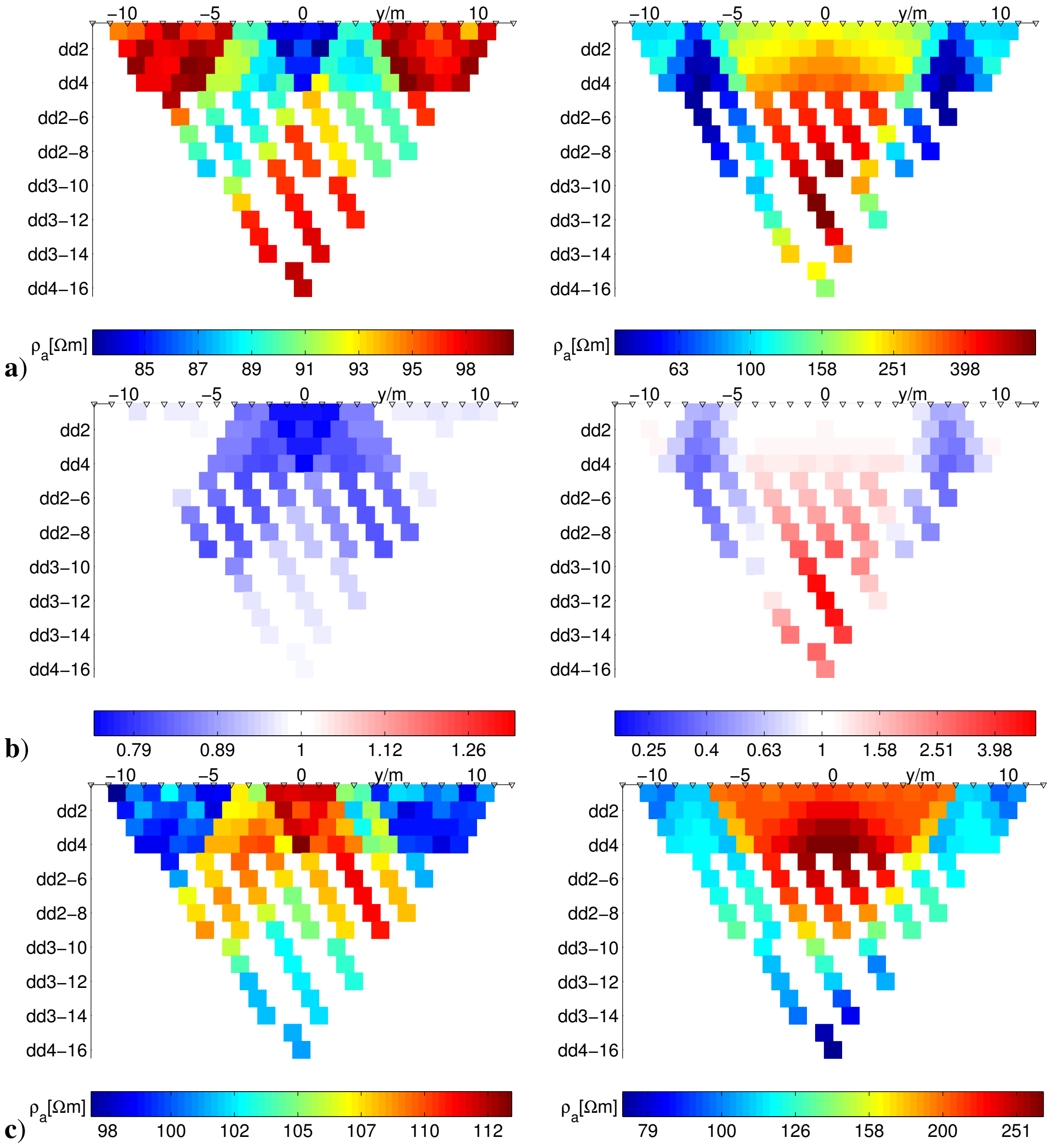

Figure 4.6.: Topography effect for two example profiles $x = -10\,\mathrm{m}$ (left) and $x = 0\,\mathrm{m}$ (right) of the synthetic model from Figure 4.5: ρ_a based on flat-earth geometric factors (**a**), geometry effect (**b**) and ρ_a using simulated geometric factors (**c**).

The inversion is initiated with a starting model of a homogeneous resistivity of 200 Ωm. The regularization parameter has been chosen according to the L-curve criterion in the first iteration (Fig. 4.2) to be $\lambda = 55$. Table 4.1 shows the inversion facts for each iteration. The chi-squared misfit (weighted data functional per data) was decreased from 117 to 1.1 in 5 steps. The line search procedure indicates an essential non-linearity. The main reduction of the misfit is achieved by just one iteration. Due to the global regularization technique the maximum model parameter range (column 3 and 4 of Table 4.1) does not increase in the further course of inversion. Finally, the inversion stagnates at the expected level of 1, i.e. the data are fitted within the (known) noise level.

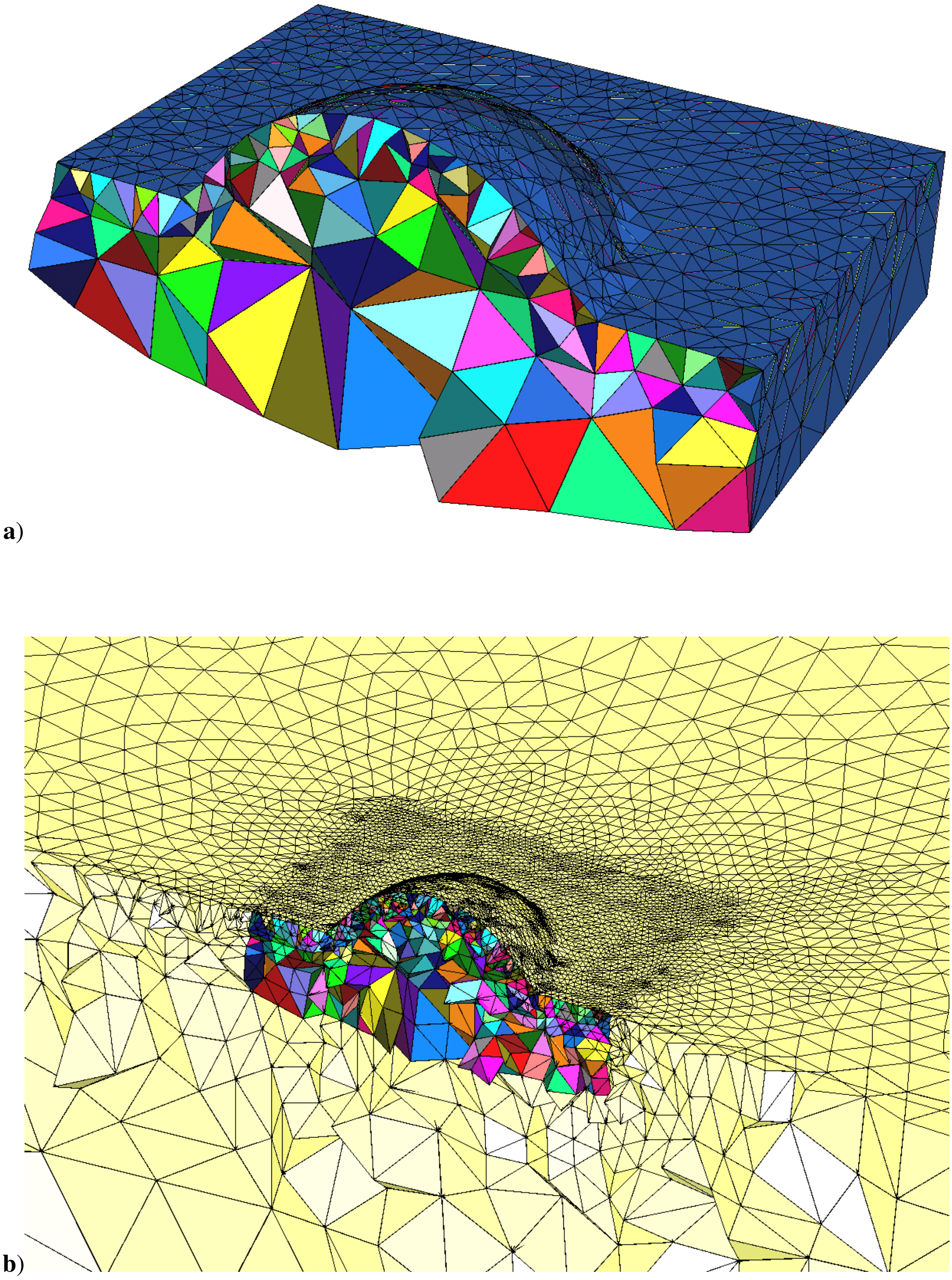

Figure 4.7.: Meshes used for the inversion. **a**) The parameter mesh is embedded into **b**) the secondary field mesh which is globally refined and prolonged.

Figure 4.8 displays the inversion result. An iso-surface with the value of 300 Ωm clearly depicts the location of the cavity. Also, the resistivity contrast between the mound and the underground is clearly visible.

Table 4.1.: Line search parameter τ, model range and chi-squared data fit in the course of iterations

Iteration	τ	$\min(\rho)$	$\max(\rho)$	χ^2 misfit
0	-	110	110	117.0
1	0.93	77	524	3.1
2	0.90	73	508	2.0
3	0.75	77	513	1.5
4	0.36	77	516	1.3
5	0.05	77	514	1.1

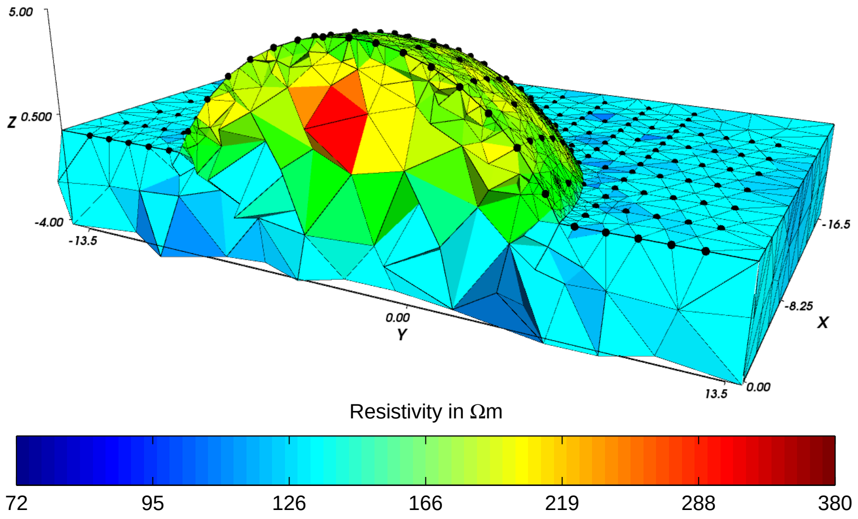

Figure 4.8.: Inversion result of the synthetic model data. The iso-surface is determined by a value of 300 Ωm.

4.5.4. Comparison with even surface

The question arises if the data might be explained without incorporation of topography. Therefore, the locations of the electrodes are projected onto a horizontal surface at $z = 0$m (ground level) and the same approach as before is used except that the primary potentials were calculated analytically. Due to the simpler geometry the number of parameter cells reduces to 7 448. The inverted the apparent resistivities based on flat-earth geometric factors. However, the inversion process became unstable and parameter values exceeded the range of 1 to 100 000 Ωm without reaching a data fit of less than 20%. Therefore, these results are not shown.

Thereafter, the flat parametrization is used to invert the apparent resistivities based on the simulated geometric factors since they already include the topography effect. Consequently, the data can be fitted approximately ($\chi^2 = 2.5$). Figure 4.9 shows a section of the corresponding inversion result.

It shows the main features of the resistive mound in conductive background and the cavity can also be seen. However, the latter anomaly is weaker and smeared over a larger region. Moreover, stronger artefacts arise at the surface. To summarize, although the simulated geometric factors

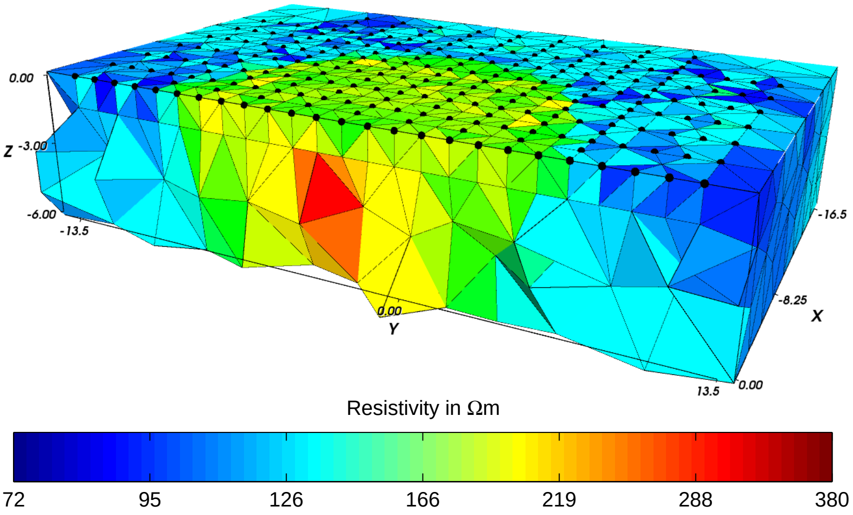

Figure 4.9.: Inversion result using the calculated apparent resistivities on even parametrization.

allow for easy inversion methods, the topography needs to be involved into the parametrization to obtain a geometrically reliable model. Note that the determination of geometric factors by calculating the primary potentials is already the main portion of runtime (see Table 4.2).

Presupposing the topography is sufficiently smooth so that their effects can be neglected, block-oriented grids are usually used for inversion. In order to compare the results from the triple-grid technique with a block-oriented discretization, an equidistant grid is created with $\mathrm{d}x = \mathrm{d}y = 1\,\mathrm{m}$. Using 8 layers a number of $34 \times 28 \times 8 = 7\,616$ parameters are obtained which is comparable to the size of the unstructured parameter mesh. However, with the latter the model can be described more accurately since the elements are smaller at the surface where the physical resolution is better. Hence, the unstructured meshes seem more efficient even for a flat surface, particularly if refinement and prolongation of the forward mesh is considered.

4.6. Application to field data

As a field example, the technique is applied to the investigation of an abandoned mining dump which contains slag material originating from steel production[1]. The deposition has been ceased in 1995. Hardpans formed when the dump material was exposed to precipitation and evaporation thus leading to alteration of the material and the development of silicate gels. DC resistivity measurements have been carried out by the Federal Institute for Geosciences and Natural Resources, Hannover. The aim of the survey was to delineate the hardpan thickness, its function as a sealing agent, and, furthermore, to determine internal structures of the dump.

---

[1] The data were kindly provided by U. Noell, M. Furche and C. Grissemann from Federal Institute of Geosciences and Natural Resources, Hannover

The dump is about 200 m long, 70 m wide and the maximum height is 14 m above ground level. Figure 4.10 shows the topography and the used electrode layout. The top profile has an electrode separation of 1 m, whereas the 13 cross profiles have electrode separations of 2 m. The profile distance is 10 m, which is five times the electrode separation and, thus, just sufficient to try a three-dimensional reconstruction of the dump's interior.

Summing up 4 245 data have been collected with the Wenner array using in total 577 different electrode positions. Figure 4.11 shows the raw data (a), the topography effect (b) and the apparent resistivities (c) obtained by the simulated geometric factors for the profile at $x = 220$ m. Some of the main features in the raw data can be recognized by the geometry effect which shows deviations from the flat earth case of up to 30% in both directions. For example, the low values of the topography effect along the lower left-hand flank of the pseudo-section in Figure 4.11b show up as high values in the flat earth apparent resistivities of Figure 4.11a. They do not appear in the apparent resistivities with simulated geometric factors (see Figure 4.11c). Although the topography effect is not very pronounced it will account for possible misinterpretations. Hence, the topography is included in the inversion.

The parameter mesh contains a number of 62 045 tetrahedrons. This is far more than the number of data but it is needed to describe the topography sufficiently. 422 980 nodes are obtained for the primary mesh with quadratic shape functions. Such a large number requires an approximate solution of the system of equations for which the ICCG method Kershaw (1978) is chosen. The primary field calculation needs about 18 seconds for each electrode on a 2.4 GHz PC such that the whole calculation is done in 3 hours and 18 minutes including the preconditioner.

In contrast, the secondary mesh contains only 111 096 nodes. The resulting system of equations can thus be solved directly. The multi-frontal Cholesky decomposition takes about 21 seconds.

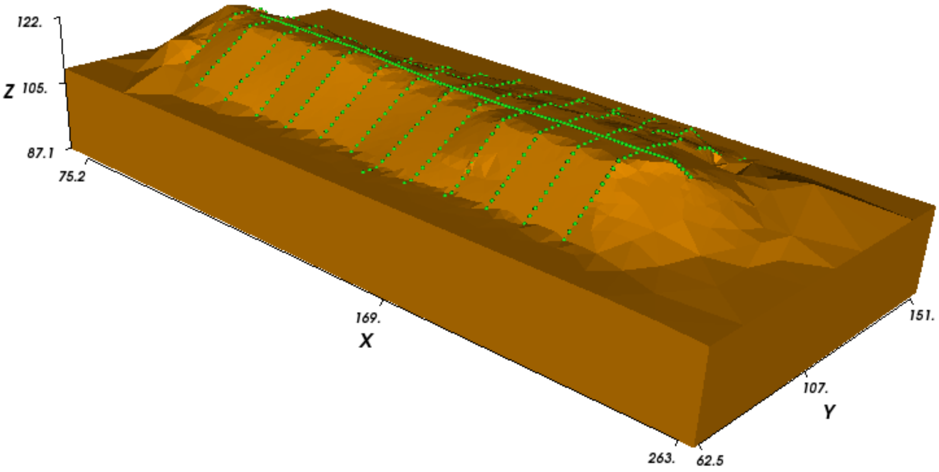

Figure 4.10.: Topography and electrode layout of the mining dump. Electrodes were located along 13 cross profiles and one along the top.

One back-substitution for a single source is carried out in less than a second such that the total forward modelling procedure needs about 8 minutes.

For the error weighting according to equation (4.1) $p = 5\%$ is used and a voltage uncertainty of $\delta U = 50\,\mu$V. By the application of the L-curve criterion a regularization strength of $\lambda = 22.5$ can be obtained. After 7 inversion steps the chi-squared misfit was decreased from 1433 to 4.7 which corresponds to a relative root mean square between data and model response of 7%. Table 4.2 assembles the time needed for the individual inversion parts. The number of 14 forward calculations is due to the inexact line-search procedure in every iteration. Note that for any further run, e.g., with changed regularization type or strength, only the last two tasks in Table 4.2 have to be carried out.

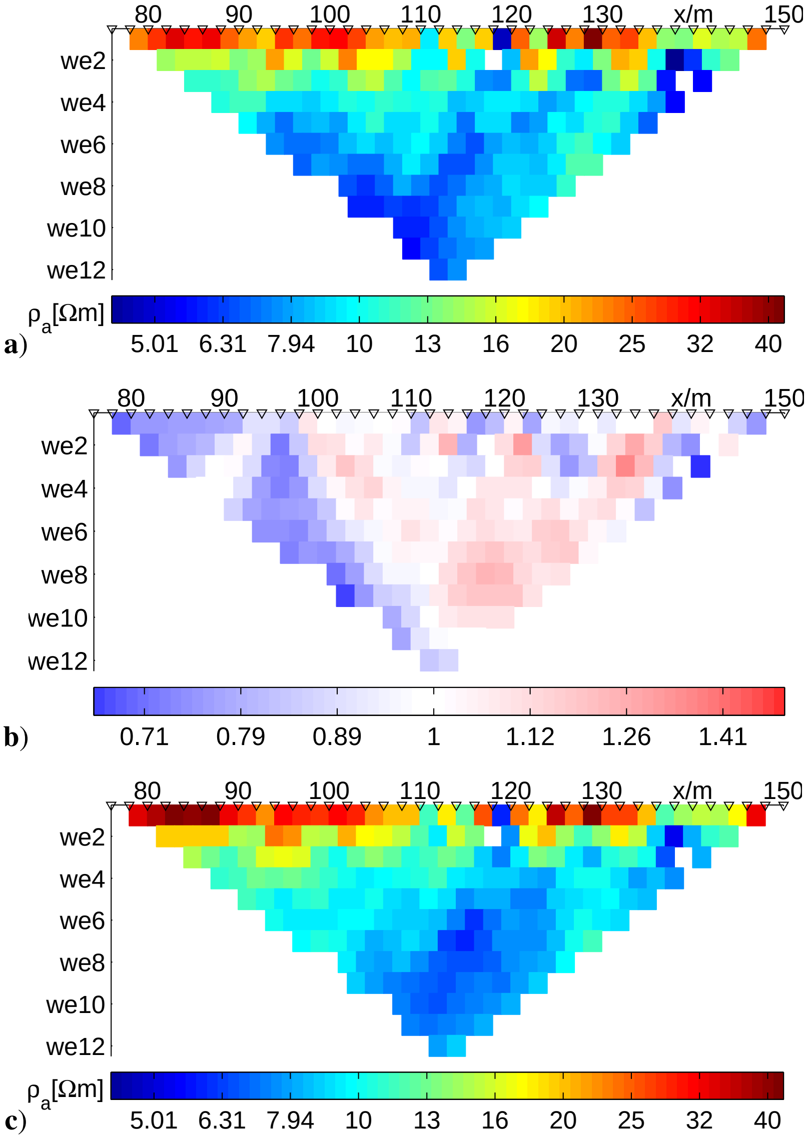

Figure 4.11.: Sample of the field data in terms of **a**) flat earth apparent resistivity data, **b**) geometric effect and **c**) apparent resistivities taking the topography into account for the cross profile at x = 220 m.

Table 4.2.: Runtime needed for the inversion of the field data for an abandoned mining dump

Procedure	Runtime	Multiplied by	Total time
Mesh generation	18 min	1	18 min
Primary potential	3 h 18 min	1	3 h 18 min
Sensitivity	1 h 42 min	1	1 h 42 min
Inverse subproblem	13 min	7	1 h 31 min
Forward calculation	8 min	14	1 h 52 min
Total			8 h 41 min

Figure 4.12 shows the inversion result. Two iso-surfaces delineate the conductive dump material ($< 6\,\Omega$m) and a resistive dump cover ($> 20\,\Omega$m), possibly due to hardpan development. In regions of missing or thinner hardpan, bulges in the low resistivity body are noticeable. No obvious internal structure of the dump is revealed which at this stage is interpreted as a hint for a homogeneous dump body as far as resistivity is concerned.

The large amount of data and parameter cells goes beyond the capacity of standard PC's to store the values of the sensitivity matrix. Since many of the values are expected to be very small, e.g., small cells at large distance from the four electrodes used, the absolute values below a certain threshold can be neglected to save memory. Consequently, **S** is stored as a sparse matrix. Note that 12 bytes are used for the indices and the value of each non-zero element in contrast to 8 byte for a full matrix element.

The threshold value is decreased logarithmically from 10^{-2} down to 10^{-6}. To avoid effects of the forward calculation the difference is computed between the first iteration model (without

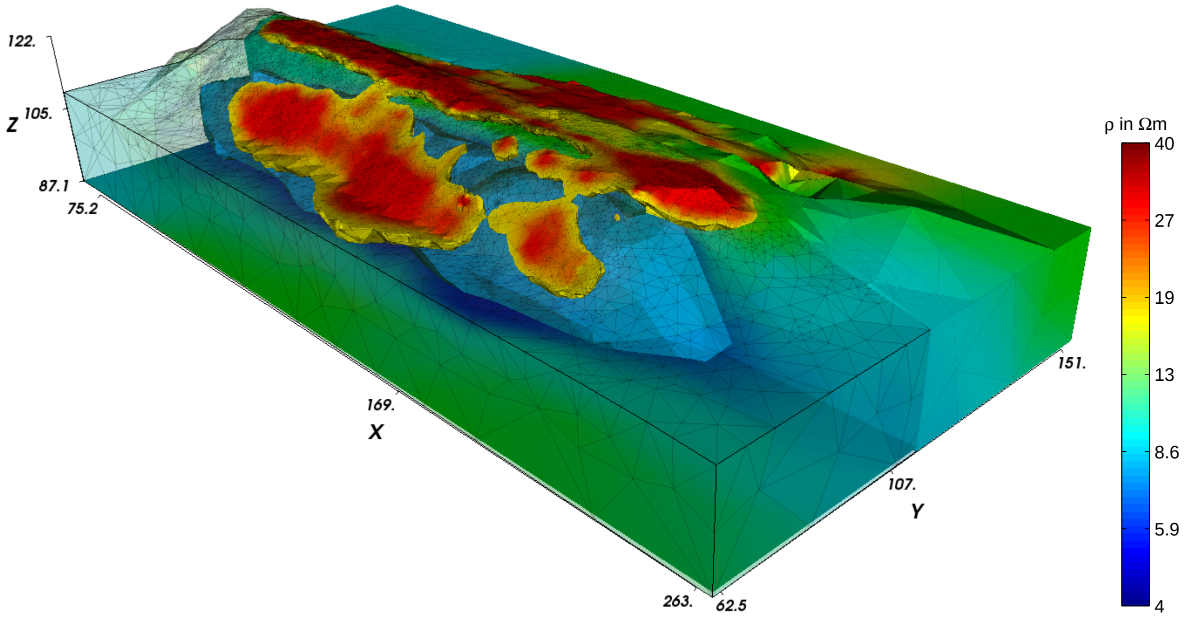

Figure 4.12.: Inversion result of the abandoned mining dump. An iso-surface of $20\,\Omega$m is used to delineate the hardpan formation. The dump body is indicated by resistivities below $6\,\Omega$m.

line search) with and without sensitivity sparsing. Table 4.3 shows the non-zero values and the model difference as a relative root mean square. A very good accordance is observed for a threshold tol $= 10^{-5}$ or below. Thus, accurate results can be obtained with 10 to 20% of the memory requirements, which is supported by comparing the final models for various data sets.

Table 4.3.: Effect of sparsing the sensitivity matrix on the result of the inverse subproblem for different threshold values. The number of non-zero elements is also given as the fraction of the full matrix and required memory. Model rms is the relative root mean square of the first iteration model with and without sparsing.

Threshold	Non-zeros	Fraction	RAM	Model rms
10^{-2}	81 809	0.02%	<1 MB	35.7%
10^{-3}	1 661 792	0.5%	19 MB	13.7%
10^{-4}	9 104 548	2.8%	104 MB	4.0%
10^{-5}	28 134 833	8.5%	322 MB	1.0%
10^{-6}	61 528 436	18.7%	704 MB	0.1%
0	329 649 720	100%	2.5 GB	0

4.7. Discussion and conclusions

An inversion strategy is presented for the reconstruction of the resistivity from DC measurements for arbitrary topography. It is an enhancement of existing techniques and combines the fast convergence of regularized Gauss-Newton methods with accurate finite element forward calculations. Unstructured tetrahedral meshes are used in order to describe the topography of the measurement area with high accuracy. Special attention is paid to an efficient forward simulation using a secondary potential approach. Therefore, the forward process is split up into two parts: the time-intensive calculation of the primary potential and the fast calculation on the moderate secondary field mesh.

A Gauss-Newton approach is used with inexact line search for solving the inverse problem. Thus a solution is guaranteed after a small number of iterations. To stabilize the solution first-order smoothness constraints are applied. However, other regularization methods have already been implemented such as second order smoothness constraints. The introduction of a-priori information as well as weighting mechanisms for different model regions will be given in Chaper 5. A further enhancement may be obtained by active constraint balancing (Yi et al., 2003). A type of focused inversion (Portniaguine and Zhdanov, 1999) may also be introduced to obtain models with sharp boundaries.

The strategy was applied to noisified synthetic data as well as to field data. The run time is strongly decreased by the singularity removal technique and the use of fast direct equation solvers. In addition, the use of unstructured meshes provides a resolution-dependent parametrization which finally saves computing time and memory. Thus, the approach is especially interesting for surveys with steep topography or large geometry contrasts. Moreover, the approach is well suited well for complicated model geometries, e.g., underwater surveys, model tank experiments or measurements on cylindrical geometries.

In cases of strong conductivity contrasts, particularly near the electrodes, errors arise in the forward calculation that can only be diminished by further refinement. In order to achieve high speed and low memory consumption, the refinement should be carried out adaptively such that only regions of weak approximation are locally refined. Another possibility of improving the forward calculation is a grid hierarchy used for multi-grid solvers or preconditioners. Since in the presented technique the Jacobian matrix needs to be stored, the memory capacities of standard PCs may by the limiting factor for many large-scale problems. Thus, methods are sought that avoid the explicit storage of the Jacobian matrix. One solution could be the technique of Zhang et al. (1995) or the non-linear conjugate gradients (NLCG) method (Ellis and Oldenburg, 1994). Due to the slower convergence of NLCG much more iterations are needed to find the minimum of the objective function. However, since the forward calculation is very fast once the primary potential has been calculated, this technique is particularly promising for large-scale problems. Other memory-saving techniques are quasi-Newton methods as proposed by Haber (2005) where the Jacobian is approximated by a sum of rank-two update matrices each stored by two vectors. Thus, the method starts with the slow convergence of gradient methods and ends up with the quadratic convergence of Newton-type methods.

The method can be further developed by incorporating induced polarization effects using complex conductivities Kemna (2000). Since the imaginary part is generally small, the primary potentials may remain real, only the secondary potentials have to be obtained complex. Moreover, the use of electric in-hole, hole-to-surface and cross-hole measurements can restrict the ambiguity of the surface data. Finally, appraisal techniques as presented by Alumbaugh and Newman (2000) or Friedel (2003) may help to find the reliability of the models.

5. Advanced electrical resistivity tomography

Abstract

ERT is a widespread technique but has limitations due to the ambiguity of the potential field problem. Therefore, additional information or assumptions are required. So far, smoothness-constrained schemes lack resolution and are too inflexible to include information.

A very flexible regularization scheme based on unstructured meshes is presented that is able to include both structure and parameter information into the inversion. Information about the model structure such as known material interfaces known from other geophysical techniques, e.g., reflection seismics or ground penetrating radar, are incorporated as allowed sharp resistivity contrasts. Additionally, the global model smoothness can be weighted individual to allow anisotropic constraints, e.g., to prefer horizontal structures. The Parameter behaviour can be controlled individual by logarithmic transformations to allow lower and upper resistivity boundaries. Model weighting functions can define the allowed deviation of the final resistivity model from given start or reference values.

As a consequent further development, the region concept, is presented where the parameter domain is subdivided into lithological or geological units, called regions. The inversion behaviour and all regularization parameters can be controlled individually on these regions. In Addition, a region can be treated as a single parameter, which can reduce the amount of unknown parameter for the inversion.

Several examples from engineering and hydrology demonstrate that the definition of interfaces such as seismic lines and regions, e.g., containing borehole information, can significantly improve the ERT images. A further example shows how a complicated three-dimensional problems with a limited dimensionality of the inverse problem can be treated efficiently be using the region concept. Finally the concept is applied to invert a very sparse dataset that is usually not interpretable by classical inversion strategies.

5.1. Introduction

Electrical resistivity tomography (ERT) is a very popular geophysical technique since resistivity is related to lithological and hydrological parameters and shows often sufficiently large contrasts. The rapid development of multi-electrode equipment in the 1990s lead to a wide spreading of ERT and made it a fast standard method for engineering problems (e.g., Knödel et al., 2007) and hydrogeophysical questions (e.g., Binley and Kemna, 2005). Applications reach from the cm-dm scale on soil probes (e.g., Binley et al., 1996) over typical near-surface targets with some tens of meters investigation depth (e.g., Loke et al., 2003) to large-scale investigations (e.g., Flechsig et al., 2010).

With the increasing amount of gained data the demand for inversion software grew. There are numerous papers on the inversion of 2D profiles on the basis of finite difference (FD) forward calculation and discretization (e.g., Tripp et al., 1984; Loke and Barker, 1996a). Comparable, FD-based 3D inversion techniques developed as first data sets were available (Park and Van, 1991; Loke and Barker, 1996b). Finite elements (FE) calculations (Coggon, 1971; Zhou and Greenhalgh, 2001) were introduced later and were used in 2D (Kemna, 2000) and 3D (Sasaki, 1994) inversion. All have in common that the subsurface is being discretized by a large number of model cells. However, up to now they are mostly regularly arranged even if FE forward calculations are used (e.g., Kemna, 2000; Sasaki, 1994). Alternatively, irregularly distributed triangles (2D) or tetrahedrons (3D) allow a more flexible incorporation of topography (Günther et al., 2006). Most algorithms use smoothness constraints (Constable et al., 1987; Brecque et al., 1995) in order to overcome the ambiguity of the inverse problem. However, although the results are very stable, the smooth nature of the results can make the interpretation inaccurate. Moreover, artefacts can appear due to the regularization technique (e.g., Clément et al., 2009).

There are several approaches to overcome overly smoothed models. Yi et al. (2003) use active constraint balancing to enhance the resolving power. A model-side robust, so-called blocky, minimization scheme based on L1 minimization (Farquharson and Oldenburg, 1998) can yield models with accentuated gradients (Loke et al., 2003). Portniaguine and Zhdanov (1999) and Blaschek et al. (2008) use focusing techniques to obtain sharp interfaces. Clément et al. (2009) observe much more reliable time-lapse results when incorporating structural constraints and Lelièvre and Oldenburg (2009) investigate options to incorporate structural orientation information into the inversion. In a cross-borehole experiment, Doetsch et al. (2010) use completely decoupled model parts to remove smoothing between borehole drilling fluid and subsurface, which leads to a significantly improved image. In all cases mentioned above, a-priori information is added to the inverse problem and thus improves the resolution (Pous et al., 1987).

A-priori information can be about structural character of the model, e.g., by reflection seismics or ground penetrating radar (GPR) data or from borehole descriptions. However, it can also represent resistivity data, e.g., from borehole logs or from other measurements. Even if the true resistivity of a unit is not known, its range can be limited based on experience or petrophysical considerations. This additional constraint can be achieved by additional regularization terms or a transformed model function. For example, the logarithm is often used to ensure positive resistivity. It can be further restricted by combining different log functions (Günther, 2004). However, this knowledge may only related to specific parts of the model. In order to incorporate all present information, a very specific regularization scheme is required.

A very flexible regularization approach is presented based on regions created by structural interfaces. Unstructured meshes (Shewchuk, 2002; Si, 2004) are used to incorporate arbitrary lines (2D) or faces (3D). The subsurface can so easily be subdivided into regions whose behaviour can be controlled very flexibly. Several applications with real data demonstrate how the inversion results can be improved by a-priori information. The introduction of a seismic reflection into a bedrock detection leads to a very simple model. A 2D measurement on the bottom of a shallow lake demonstrates how regions (the water and the sediments) can be treated specifically. An application with borehole resistivity data demonstrates how both structural and resistivity information significantly improve the interpretation of the resistivity image. The 3D nature of a basically 1D inverse problem from vertical electrodes is solved by the region concept. Finally, the region concept helps to find a very coarse resistivity model for a sparse data set that represents a highly under-determined inverse problem.

5.2. Method

5.2.1. Generalized minimization approach

The presented inversion scheme represents an extension of the triple-grid ERT inversion described in Chapter 4. A very common global minimization scheme is used (Menke, 1989):

$$||\mathbf{D}(\mathbf{d}-\mathbf{f}(\mathbf{m}))||_2^2 + \lambda ||\mathbf{C}\mathbf{m}-\mathbf{h}|| \rightarrow \min \tag{5.1}$$

where $\mathbf{d}$ is the vector of $\mathcal{D}$ individual data d_i, $\mathbf{m}$ is the sought model vector with $\mathcal{M}$ model parameters m_i and $\mathbf{f}(\mathbf{m})$ its forward response calculated for 3D cases using the forward operator described in Chapter 2 and 3. For the presented 2D cases, the model response is calculated according to Kemna (2000) and adapted for the triple-grid technique by using mixed unstructured triangle/quadrangle meshes. Assuming uncorrelated data variances $\delta {d_i}^2$ the misfit between the latter is weighted by a data weighting matrix $\mathbf{D} = \mathrm{diag}(1/\delta d_i)$.

Very common regularization schemes are smoothness constraints (Constable et al., 1987) where $\mathbf{C}$ is a derivative matrix and $\mathbf{h} = 0$. Figure 5.1 shows a minimalistic 2D mesh containing both triangles and rectangles. It consists of six model cells with six inner boundaries between them. Unstructured meshes can be used flexibly to describe surface or subsurface topography and

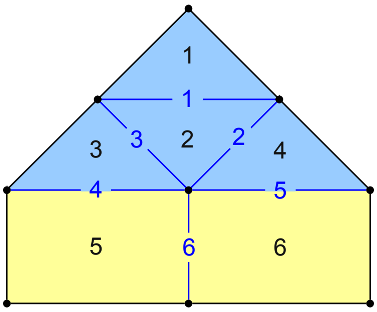

Figure 5.1.: Minimalistic model consisting of four triangles and two rectangles.

are more efficient for boundary prolongation. Furthermore, the element sizes can be controlled according to the resolution properties and thus an intrinsic regularization is achieved already. In some cases, structured meshes may be advantageous, e.g., to follow horizontal layering. However, a combination of structured and unstructured meshes can also be used.

The corresponding derivative matrix for the minimalistic mesh example in Figure 5.1 reads:

$$\mathbf{C} = \mathbf{C}_1 = \begin{pmatrix} -1 & +1 & 0 & 0 & 0 & 0 \\ 0 & -1 & 0 & +1 & 0 & 0 \\ 0 & -1 & +1 & 0 & 0 & 0 \\ 0 & 0 & -1 & 0 & +1 & 0 \\ 0 & 0 & 0 & -1 & 0 & +1 \\ 0 & 0 & 0 & 0 & -1 & +1 \end{pmatrix} \tag{5.2}$$

and has a line for each boundary and a column for each model cell.

Another common scheme is to use minimum length, i.e. the deviation from a reference model $\mathbf{m}^r$ is minimized. In this case, $\mathbf{C} = \mathbf{C}_0$ is the identity matrix and $\mathbf{h} = \mathbf{m}^r$. In cases like process monitoring, the difference to a reference model may be constrained by smoothness. Different parts of the model can have different constraints by vertically appending their $\mathbf{C}_n$ matrices and $\mathbf{h}$ vectors.

In order to control boundaries and cells individually, the scheme is expanded by multiplying the basic constraint matrix $\mathbf{C}_1$ with two diagonal weighting matrices (Günther and Rücker, 2009):

$$\mathbf{C} = \mathrm{diag}(w_i^{\mathrm{s}})\mathbf{C}_1\,\mathrm{diag}(w_j^{\mathrm{m}}) \quad \text{for} \quad i = 1 \ldots \mathcal{S}, \quad \text{and} \quad j = 1 \ldots \mathcal{M}\,. \tag{5.3}$$

The model weight $\mathbf{w}^{\mathrm{m}} = \mathrm{diag}(w^{\mathrm{m}})$ holds a weight for all $\mathcal{M}$ model cells. So the degree of smoothness or the difference to a reference model can be controlled individually. Higher values will enforce a locally smoother (or less deviating) model, whereas lower values allow for a more contrasted (more deviating) model.

On the other hand, the structural weight $\mathbf{w}^\mathrm{s} = \mathrm{diag}(w^\mathrm{s})$ holds weights for $\mathcal{S}$ individual structural constraints, i.e. model boundaries in case of smoothness constraints, and 1 otherwise. There are various ideas where a locally modified structural weight can represent the expectations to the model:

- Anisotropic constraints, associate a lower weight to horizontal compared to vertical boundaries. A vertical weight w_z for the boundary is defined which is α_z/α_x in the sense of Constable et al. (1987). For each boundary with the normal vector $\boldsymbol{n} = (n_x, n_y, n_z)$ the structural weight can be determined by a linear function of its vertical component n_z:

  $$w^\mathrm{s} = 1 + (w_z - 1)|n_z| \,. \tag{5.4}$$

  For the mesh in Figure 5.1 and $w_z = 0.1$ the values of $\mathbf{w}^\mathrm{s} = [0.1, 0.27, 0.27, 0.1, 0.1, 1.0]$ can be calculated.

- A known sharp contrast between lithological units may be known from boreholes, seismics or GPR measurements. The interface $\mathcal{I}$, consisting of inner cell boundaries, is included into the mesh and ${w^\mathrm{s}}_i = 0$, or a small quantity, is assumed for all $i \in \mathcal{I}$.

- Sharp interfaces at unknown positions may be enforced iteratively using a robust weighting scheme (Farquharson and Oldenburg, 1998) using $\mathbf{w}^\mathrm{s} = \mathrm{IRLS}(\mathbf{Cm})$ with the L_1/L_2 mapping function

  $$\mathrm{IRLS}(r_l) = \frac{|r_l|/\sum|r_i|}{r_l^2/\sum r_i^2} = \frac{\sum c_i^2}{c_l \sum |c_i|} \,, \tag{5.5}$$

  such that large gradients obtain a low weight and vice versa.

Note that a multiplication from the left, $\mathbf{w}^\mathrm{s}$ simply amplifies the strength of the smoothness constraints. A multiplication from the right, however, between different model weights leads to an unsymmetrical smoothness and would enforce model gradients. Therefore, $\mathbf{w}^\mathrm{m}$ is only used within separated parts of the model (regions) or for minimum length constraints.

5.2.2. Transformation functions

In most ERT inversions, the logarithm of the resistivity ρ is inverted. This represents a-priori information about the valid range, e.g., prohibit negative resistivity and is often supported by the statistical distribution or interpretation schemes. Instead of zero, the lower boundary of ρ^l can be restricted by using $\log(\rho - \rho^\mathrm{l})$. In the same manner, an upper boundary ρ^u can be defined and even combined with ρ^l using the model transformation

$$m_i = \log(\rho_i - \rho^\mathrm{l}) - \log(\rho^\mathrm{u} - \rho_i) \;, \;\; \text{for} \;\; i = 1 \ldots \mathcal{M} \tag{5.6}$$

with the individual resistivity ρ_i for model m_i. Note that a transformation of the model parameter affects the elements of the sensitivity or Jacobian matrix which has to be divided by the derivative of the transformation function.

The Gauss-Newton minimization scheme is applied for equation (5.1) to solve the inverse subproblem

$$(\mathbf{S}^{\mathrm{T}}\mathbf{D}^{\mathrm{T}}\mathbf{D}\mathbf{S}+\lambda\mathbf{C}^{\mathrm{T}}\mathbf{C})\Delta\mathbf{m}^{k+1}=\mathbf{S}^{\mathrm{T}}\mathbf{D}^{\mathrm{T}}\mathbf{D}(\mathbf{d}-\mathbf{f}(\mathbf{m}^{k})+\lambda\mathbf{C}^{\mathrm{T}}(\mathbf{C}\mathbf{m}^{k}-\mathbf{h}) \tag{5.7}$$

for every iteration k for the model update $\Delta\mathbf{m}^{k+1}=\mathbf{m}^{k+1}-\mathbf{m}^{k}$.

The inverse subproblem is solved by a modified version of the CGLSCD solver (cf. Chap. 4.4.3. Neither the Jacobian **S** nor the constraint matrix **C** are formed explicitly. The multiplication of a matrix **A** is extended by the left and right vectors **l** and **r** multiplication such that

$$[\mathrm{diag}(\mathbf{l})\mathbf{A}\,\mathrm{diag}(\mathbf{r})]\cdot\mathbf{x}=[\mathbf{A}\cdot(\mathbf{x}*\mathbf{r})]*\mathbf{l}, \tag{5.8}$$

where $*$ denotes an element-wise multiplication and $\cdot$ a matrix-vector multiplication. This applies to both the Jacobian matrix and the constraint matrix. Since vector-vector multiplications are of lower order, the performance of the solver is not slowed down significantly.

5.2.3. Region concept

Since for large-scale problems the properties of individual cells cannot be controlled efficiently due to practical reasons, the so-called region concept is applied. A region is a sub-mesh mesh of the model discretization and is created by incorporating fixed separation interface lines/facets into the mesh generation process. Alternatively, regions can be defined by clustering mesh cells of previously generated meshes. Regions have the following (constant) properties as inversion control parameters:

- starting (and possibly reference) model $\mathbf{m}_0$ and model weighting $\mathbf{w}^{\mathrm{m}}$
- lower and upper resistivity bounds ρ^{l} and ρ^{u}
- vertical weight w_z
- constraint type (smoothness or minimum length)
- individual model transformation

Additionally, a region can be defined as a single region, i.e., the cells within the region are treated as one parameter by summing up the Jacobian elements. The resistivity of a single region can be constrained against a reference or not. Another special type is a background region whose cells are excluded from inversion but used in the forward calculation. The background region corresponds to the prolonged part of the secondary field mesh described in Chapter 4.

Additionally to the regularization terms within the individual regions so-called inter-region constraints can be easily appended to the constraints, i.e., smoothness terms for cell boundaries between the regions. For smoothness constraints between regions with different model control the ± 1 values in equation (5.2) changes to $1/w^{\mathrm{m}}$ in order to prevent an asymmetric gradient. For example, the triangles and rectangles in Figure 5.1 are treated as two separate regions. Then the lines 4 and 5 of $\mathbf{C}$ from equation (5.2) vanish unless inter-region constraints are defined. Together with a vertical weight $w_z = 0.1$ and a large model control $\mathbf{w}^{\mathrm{m}} = \text{const.} = 5$ in the quadrangle region the resulting constraint matrix is

$$\mathbf{C} = \begin{pmatrix} -0.1 & +0.1 & 0 & 0 & 0 & 0 \\ 0 & -0.27 & 0 & +0.27 & 0 & 0 \\ 0 & -0.27 & +0.27 & 0 & 0 & 0 \\ 0 & 0 & 0 & 0 & -5 & +5 \end{pmatrix}$$

In case of minimum lengths constraints in the triangle region (a) or its use as single region with inter-region constraints (b) $\mathbf{C}$ changes to

$$\mathbf{C}^{(\mathrm{a})} = \begin{pmatrix} 1 & 0 & 0 & 0 & 0 & 0 \\ 0 & 1 & 0 & 0 & 0 & 0 \\ 0 & 0 & 1 & 0 & 0 & 0 \\ 0 & 0 & 0 & 1 & 0 & 0 \\ 0 & 0 & 0 & 0 & -5 & 5 \end{pmatrix} \quad \text{and} \quad \mathbf{C}^{(\mathrm{b})} = \begin{pmatrix} 1 & 0 & 0 \\ 0 & -5 & 5 \\ -1 & 1 & 0 \\ -1 & 0 & 1 \end{pmatrix} \text{, respectively.}$$

The GIMLi software library provides a method-independent region manager which assembles the matrix $\mathbf{C}$, the various transformation ($\mathbf{t}^{\mathrm{m}}$, $\mathbf{t}^{\mathrm{d}}$) and the weighting vectors ($\mathbf{w}^{\mathrm{m}}$, $\mathbf{w}^{\mathrm{s}}$) which are controlling the inverse solver and are needed by the inverse subproblem. The forward calculation can be done on a hierarchical derivative of the parameter domain as described in Chapter 4 or on a completely independent mesh by using conformal mapping of the parameter distribution.

5.3. Examples

5.3.1. Incorporating structural constraints from seismics

Often there are ideas about the rough structure of the subsurface. The information for this might be derived from reflection seismics or GPR measurements in form of piece-wise continuous lines. These lines can be interpreted as material interfaces which represent high velocity/density or permittivity/conductivity contrasts. It might be expected that high resistivity contrasts appear at such material interfaces. Such interfaces can also be derived from borehole lithology or logs where the resistivity is expected to jump at least in the neighbourhood of the borehole.

The following example[1] was taken from a bedrock detection, a typical task for shallow geophysical techniques ahead of digging activities or within stability investigations. The ERT data comprises 392 points measured with Wenner-α array at 50 electrodes with a spacing of 10 m. The data noise was approximately 2%. Additionally to the geoelectric measurements, seismic refraction data were acquired with a geophone spacing of 10 m and 8 shots with 50 m interval. Refraction is a standard tool for bedrock detection, however, in case of heterogeneous overburden many shots are needed to carry out a tomography. Fortunately, it was easy in this case to fit the data by a two-layer model with a varying interface between a depth of 20 and 50 m.

Figure 5.2a shows the result of the resistivity inversion without additional information. The bedrock is clearly shown high resistive, however, a very clear distinction of the correct depth cannot be made with the resistivity alone.

---

[1] The data were kindly provided by Thomas Schicht (K-UTec Sondershausen)

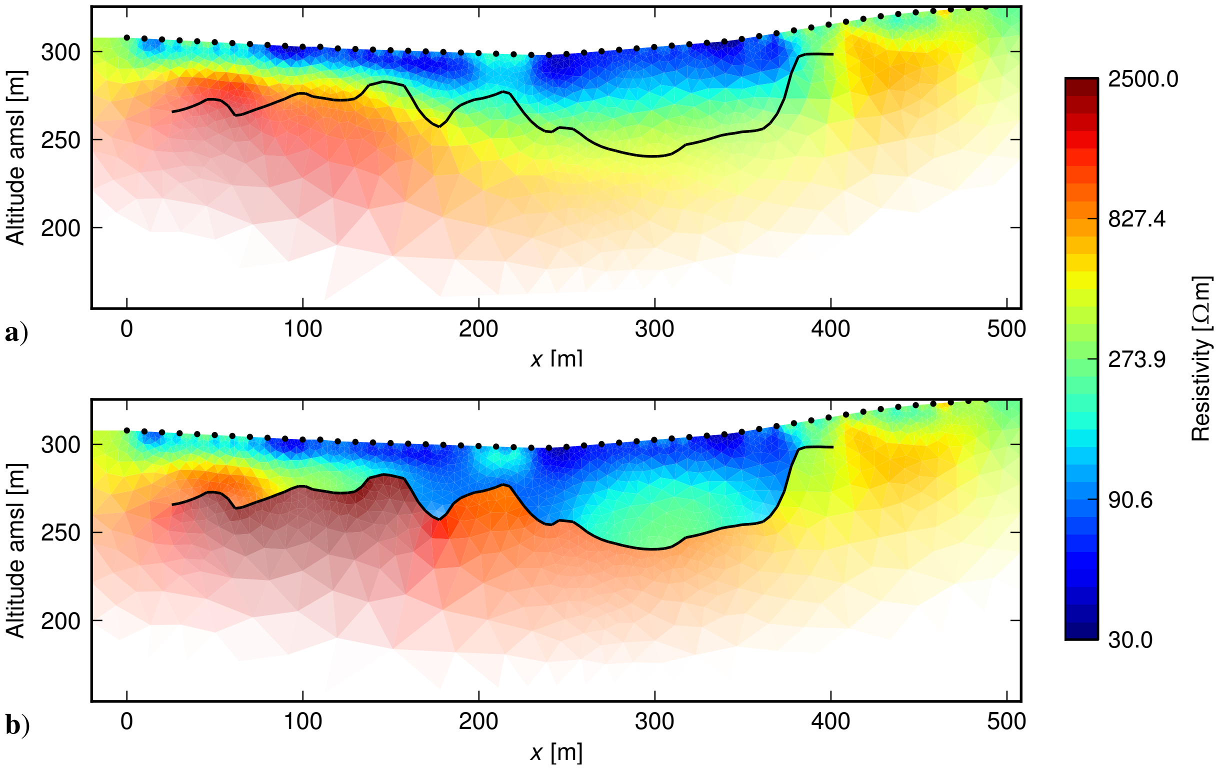

Figure 5.2.: Inversion result without (**a**) and with (**b**) refractor (black line) as a known boundary. The opacity of the used colours corresponds to the coverage of the measured data, i.e., the row-wise summation of the absolute entries of the Jacobian matrix which decrease with increasing depth. The dots denote electrode positions.

The seismic interface is now included as a structural information in order to obtain a more reliable resistivity model. The polygon is added as a constraint to the piece-wise linear complex (PLC), the input of the mesh generator Triangle (Shewchuk, 2002). As a result, the complete polygon consists of known edges between each two triangles. Since a marker is incorporated to the input of the edges, they can be easily identified and their corresponding structural weights w_i^s can be set to zero such that resistivity contrasts are admitted (but not forced).

Figure 5.2b shows the resulting resistivity model. The most dominant change coincides with the seismic refractor (black line). It shows abrupt jumps from about 100 to a few 1 000 Ωm at the main part of the interface. However at the left part, the sediments seem to be divided into two layers, presumably silt and sand. A horizontal change between the same sediments happens at the right margin of the interface, where the jump was already visible in the normal inversion (Fig. 5.2a). At about $x = 300$ m the depth of the refractor might be slightly too deep causing in an increase of the resistivity above.

Note, the model response for both inversion results fits the measured data within the data error ($\chi^2 = 1.0$), hence both models are in the sense of inversion equivalent.

5.3.2. Demonstration of the region concept by an underwater survey

In order to investigate sediments to give hints of the historic vegetation on the alleged site of the Varus Battle the LIAG institute carried out ERT measurements on the bottom of a shallow lake. Two borehole electrode cables were combined each with 24 take-outs and 2 m electrode spacing across the lake. The first and last two electrodes were coupled to steel sticks on the shore, whereas the other take-outs were laying in the water on the bottom of the ≈2 m deep lake. The resistivity of the water was measured at 22.5 Ωm with only few lateral and vertical variations.

A combined data set, consisting of 657 values, using Wenner-α and Wenner-β array was acquired in order to improve the resolution. 2% were added to the stacking error for weighting the individual data. Despite lacking reciprocal measurements this choice turned out to be very plausible and controlled all subsequent inversions such that the data was fitted within noise ($\chi^2 = 1$). In order to enhance sedimentary, i.e., more or less layered structures, the vertical weight w_z was chosen to be 0.1.

Figure 5.4a shows the normal inversion result with only one inversion region. It shows a conductive (≈ 30 Ωm) lake over a medium resistivity subsurface with the highest values on the left. The meaning of the individual anomalies will not be discussed here, but it will be shown how to improve the image by using the region concept. The water table shows far too high resistivities due to the symmetry with respect to the electrode line. Apparently the lake itself must be treated differently. Thus, the model is subdivided into two regions along the lake bottom line, the lake region (1) and the sediment region (2).

Figure 5.3 shows a section of the used PLC. The inverse box is created inside the bigger outer box and the line across the electrode nodes (dots) is the region separator. Note that the electrodes are refined locally by a quarter electrode distance to account for the higher resolution in their vicinity. There is one region marker in each of the three regions so that the elements of the resulting mesh (Fig. 5.3) obtaining them. Note that the mesh stays the same for the following computations but different from the normal inversion since the lake bottom was not discretized there.

The outer region (3) is used as background for the forward calculation. The sediment region (2) has constant properties with the bounds $\rho^{\mathrm{l}} = 10\,\Omega\mathrm{m}$ and $\rho^{\mathrm{u}} = 1000\,\Omega\mathrm{m}$, a constant starting model of $\mathbf{m}_0 = 30\,\Omega\mathrm{m}$, smoothness constraints with $w_z = 0.1$ and a constant model weight $\mathbf{w}^{\mathrm{m}} = 1$. The behaviour of the lake region is changed step by step by the parameters summarized in Table 5.1. In total six parameter variants are selected which produce the inversion results in Figure 5.4b-g. Note that for all variants λ was chosen such that the model fits the data with $\chi^2 = 1$.

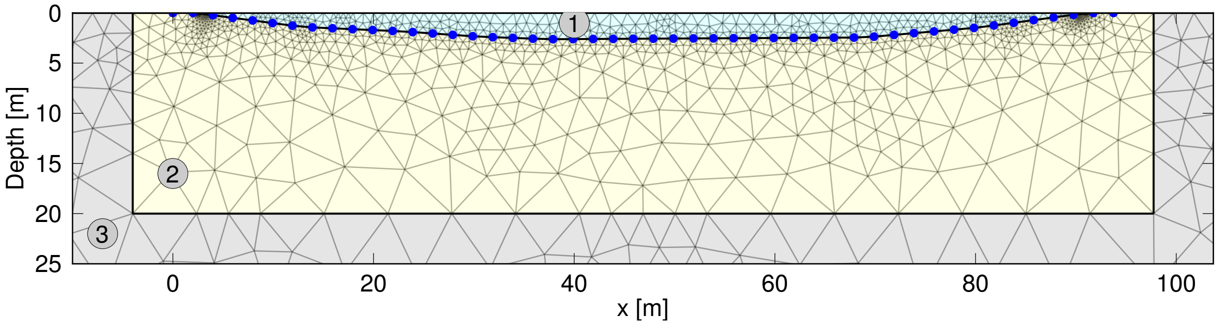

Figure 5.3.: Input PLC for the mesh generator whereas the bold black lines denote region separators and the blue dots represents fixed electrode nodes. The resulting mesh elements differentiate the regions 1–3.

Table 5.1.: Lake region (1) parameters for different regularization strategies: region type, lower/upper resistivity bound $\rho^{\mathrm{l}}/\rho^{\mathrm{u}}$, model control MC and inter-region control IRC.

Variant	Subfigure	Region type	$\rho^{\mathrm{l}}[\Omega\mathrm{m}]$	$\rho^{\mathrm{u}}[\Omega\mathrm{m}]$	$\mathbf{w}^{\mathrm{m}}$ (const.)	IRC
0	a	no regions				
1	b	multi	10	1000	1	0
2	c	multi	20	30	1	0
3	d	single	10	1000	1	0
4a	e	single	22	23	1	0
4b	f	single	10	1000	10	0
5	g	single	10	1000	10	0.1

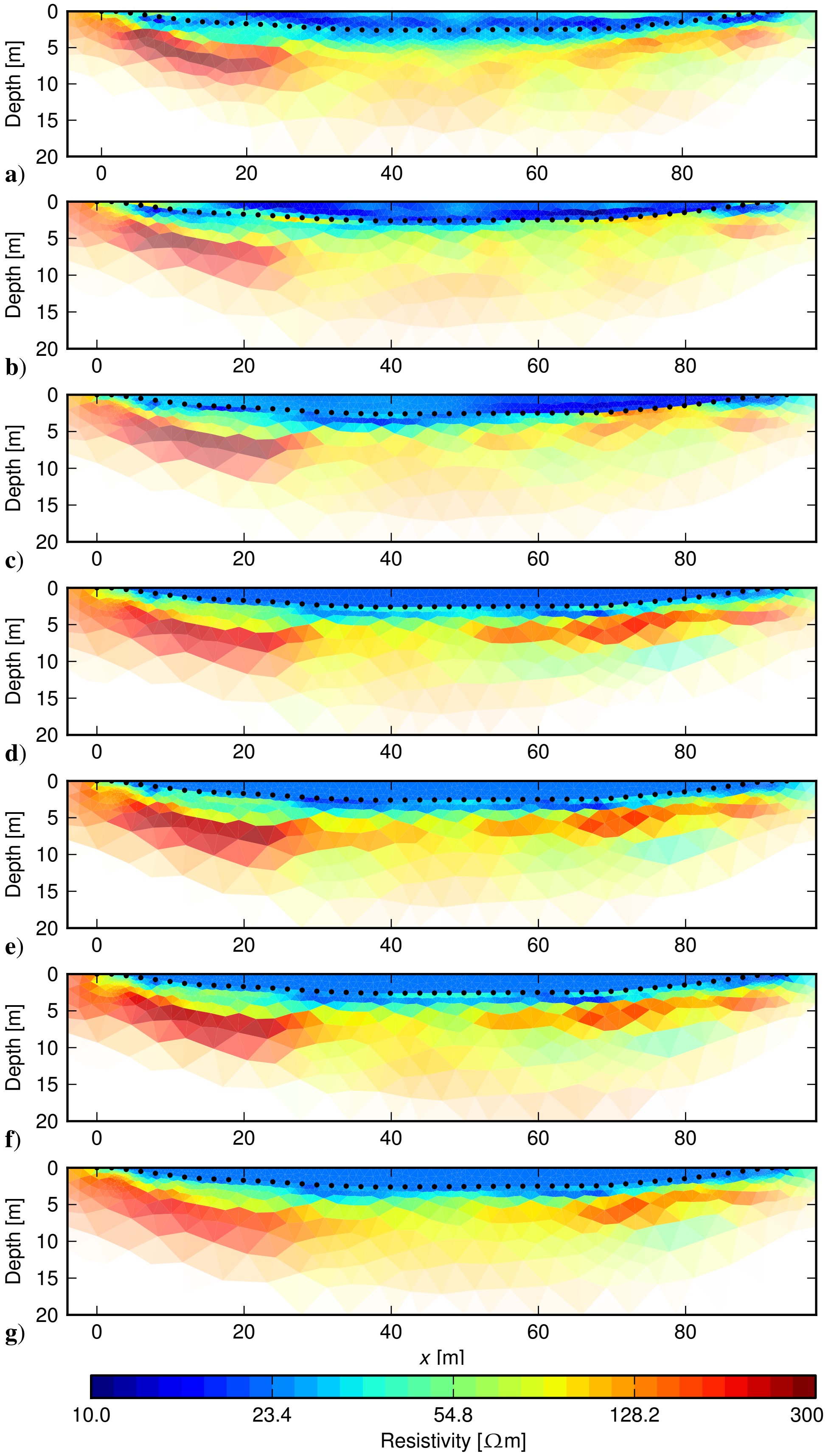

Figure 5.4.: Inversion results of different regularization strategies according to Table 5.1.

At first, variant 1, both regions are assumed to be equal what corresponds to a decoupling at the bottom line as in the structural example (Fig. 5.2). Consequently, in Figure 5.4b sharp contrasts appear but the lake still shows anomalous resistivity. Hence, in variant 2 the lake water resistivity is limited to 10 – 30 Ωm and Figure 5.4c is obtained. In doing so, the symmetry artefacts are being avoided while variability is still present. The resistivity range could of course be limited further by using even tighter bounds. Alternatively (variant 3, Fig. 5.4d) the lake could be treated as a single region but with identical resistivity bounds as in variant 1. This results in a constant water resistivity of about 30 Ωm which is slightly too high. Two ways are possible to incorporate the directly measured resistivity values of the water, Variant 4a (Fig. 5.4e) restricts the resistivity to the interval 22–23 Ωm and variant 4b (Fig. 5.4f) uses a large model control to constrain the resistivity to a starting model of the lake region of $\mathbf{m}_0 = 22.5\,\Omega\mathrm{m}$. Both results are practically identical since the same information is added just by two different technical variants.

It could now be argued, that there is no sharp interface between pure water and the mud at the bottom which is supposed to have a resistivity similar to the water. Therefore, additional (inter-region) constraints can be put in to allow for slight changes across the lake bottom line. Variant 4a cannot serve as a basis as it uses different model transformations. Therefore, variant 4b is used and altered by defining an IRC value of 0.1 for the lake/sediment boundary, corresponding to w_z. The resulting model (Fig. 5.4g) is similar to variant 4a (Fig. 5.4f) but some of the higher resistivity values at the lake bottom, e.g., at $x = 20$ m, are vanished. Finally, all images are similar and the interpretation of the sediment layers does not change significantly among the variants. However, an improved model can be found by incorporating additional information or expectations, respectively.

5.3.3. Incorporating borehole parameter information

External information are not always available for the whole extended region as in the case of the water body resistivity from the preceding example. Boreholes are frequently present in order to support or calibrate imaging of geophysical surface data. On the one hand, the borehole lithology can provide structural information about existing layers, at least in the vicinity of the borehole. Small interface lines can improve the result as shown in Figure 5.2. On the other hand, measurements can either be extended to use sensors in boreholes or to drive logs.

In the following, a DC resistivity measurement is presented originating from a bedrock detection problem[2]. A total of 1 223 single data were acquired with Wenner-α/Schlumberger array using 64 electrodes with a spacing of 5 m. Data errors were estimated using a 2% fixed error plus 100 μV voltage error. Additionally, a resistivity probe was conducted in the middle of the profile with a two-point array every 0.25 m. Figure 5.5 shows the measured distribution as a function of depth (blue). The profile starts with a fairly conductive (10 Ωm) clayey overburden. At a depth

---

[2] The data were kindly provided by Thomas Schicht (K-UTec Sondershausen)

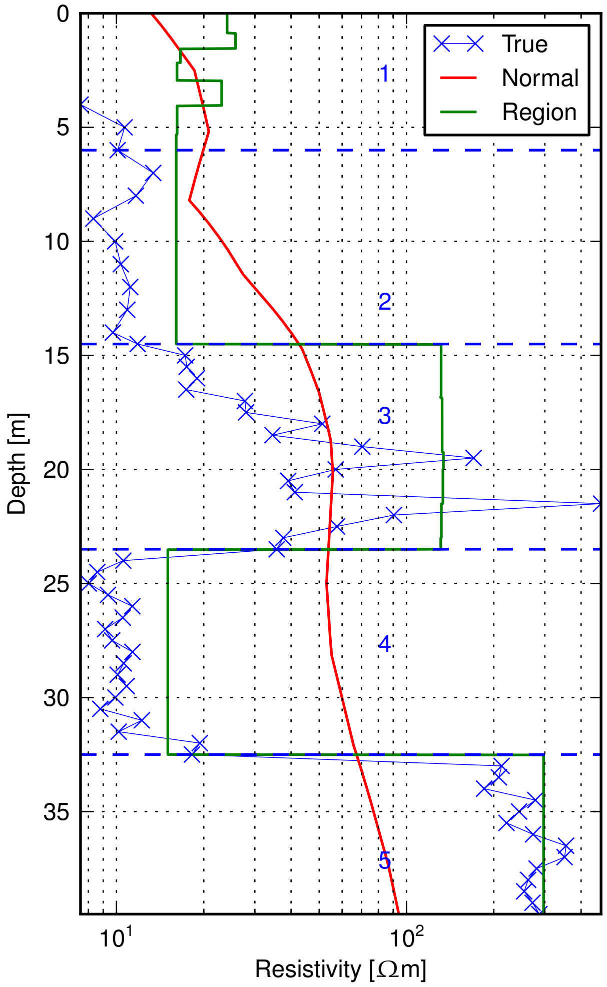

Figure 5.5.: Resistivity measured in the borehole (blue), results of a normal inversion (red) and using borehole region boxes (green), the dashed blue line denotes the region boundaries with the written numbers.

of 15 m follows a highly variable, mostly resistive fresh-water sand. Then the resistivities go back to about 10 Ωm before the bedrock is reached with resistivities beyond 200 Ωm. The log is subdivided by four interfaces at 6, 14.5, 23.5 and 32.5 m depth (dashed lines in Fig. 5.5) into five regions which represents the most obviously resistivity changes.

First, a normal inversion with a vertical weight of $w_z = 0.1$ was done yielding Figure 5.6a. Upper and lower resistivities were set to $\rho^{\mathrm{l}} = 8\,\Omega\mathrm{m}$ and $\rho^{\mathrm{u}} = 500\,\Omega\mathrm{m}$, respectively. The data were fitted within noise level ($\chi^2 = 1$). The clayey overburden can by clearly seen as well as the sand below and the bedrock at the depth but not the conductive clay layer in-between. At the borehole position, the bedrock is too deep and seems to be over-thrusting which is probably an artefact from the extremely anisotropic regularization. To improve the model, the structural and parameter knowledge from the borehole is incorporated into the inversion by defining regions as 10 m wide boxes at the borehole position. Table 5.2 shows their parameters additionally to the global $\rho^{\mathrm{l}}/\rho^{\mathrm{u}}$.

Table 5.2.: Parameters for the borehole regions.

Region	Depth $z =$	Type	Constraint type	$\mathbf{m}_0$ (const.)	w_z	$\mathbf{w}^{\mathrm{m}}$ (const.)
1	0 – 75 m	multi	1	200	0.01	1
2	6 – 14.5 m	single	0	15	-	2
3	14.5 – 23.5 m	multi	1	60	0.01	2
4	23.5 – 32.5 m	single	0	15	-	5
5	32.5 – 42.0 m	single	0	300	-	2

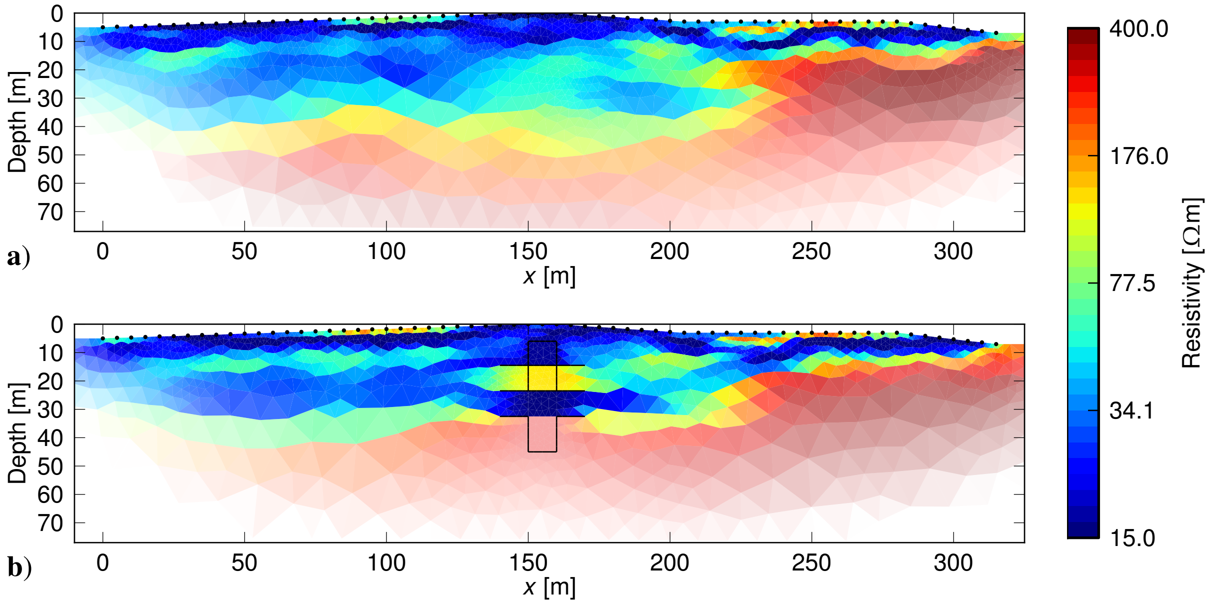

Figure 5.6.: **a**) Standard inversion result and **b**) result with a-priori borehole data.

The outer region (1) adopts all parameters from the normal inversion. Regions 2, 4 and 5 are fairly constant and are treated as single regions constrained against the absolute deviation from the starting model of 15, 15 and 300 Ωm, respectively. Region 3 is defined as a multi-region like region 1 because variations in its resistivities are expected. Since it is to be expected that the model in the borehole neighbourhood will be affected by the several borehole regions, inter-region constraints are defined with $\mathrm{IRC} = 1$ between all boxes and region 1. An $\mathrm{IRC} = 0$ is set between the boxes because they should not affect each other. Additionally to the boxes, small vertical interfaces are installed at the left and right side at the borehole for each region boundary to support the idea of layering. Figure 5.6b shows the resulting resistivity image.

The mostly resistive fresh-water sand layer at depth $= -20$ m is visible in the neighbourhood of the borehole but disappears with increasing distance. This could be real or just a problem of the low resolution of the relatively thin resistive layer within a high conductive background. At the left part of the profile, the fresh-water sand layer seems to reappear at a lower depth but it is not clear whether the layers are connected. In contrary to the normal inversion, the low resistive layer above the bedrock, which is known from the borehole log, is now clearly visible.

The bedrock itself can now be better followed and is slightly ascending to increasing x values as expected from other measurements, which is a clear improvement over the normal inversion due to the borehole data. On the left hand side of the profile, the image tends more to the normal inversion.

The results of the two inversions are plotted together with the borehole log in Figure 5.5. The normal inversion shows only a very smooth curve that tends to the log, the region-based inversion does a much better job. For the latter, the resistivity is constant at the starting values in regions 2, 4 and 5. Region 3 shows a maximum value that is similar to that from the log.

5.3.4. Solving a 1D inverse problem while modelling in 3D

ERT is three-dimensional by nature but can sometimes be interpreted only one- or two-dimensionally. If the forward calculation cannot be reduced to lower dimensions, a model transformation has to be sought between a 3D forward mesh and a 1D/2D inverse mesh. The presented example uses data from a vertical electrode chain with extended electrodes and a complicated 3D subsurface lacking the space used by the installed tool (cf. Chap. 3.4.4). Südekum et al. (2010) installed a fixed system with ring electrodes in order to monitor changes of the fresh/salt-water interface below the North Sea island Borkum.[3] 78 electrodes with $a = 0.25\,\mathrm{m}$ spacing gained 917 data values using Wenner-α array.

For a static resistivity image, the 3D geometry of the electrodes as well as the borehole geometry has to be considered. A fine tetrahedral primary mesh for the forward calculation is needed to ensure accurate responses and to include the ring geometry. The forward calculation is carried out using the CEM model described in Chapter 3 which exactly simulates current injection and potential shunting along the electrode faces. The primary mesh contains 116 582 nodes and 695 889 tetrahedrons. To keep the number of unknowns for the inversion within reasonable limits a coarse parameter mesh was generated with 1 792 nodes and 10 349 tetrahedrons.

The current source positions within the parameter mesh are represented by nodes at replacement positions for the ring electrodes. The lacking drilling inside the parameter mesh leads to different geometries which both meshes span over. Therefore, the parameter mesh has to be mapped onto the primary mesh. The nearly 700 000 primary mesh cells must be clustered to match the ten thousand parameters cells. Each cluster will be used accordingly as a single region for the inversion. This allows for an accurate forward response that incorporates the finite electrodes as well as the borehole geometry.

Some additional effort is needed for mapping the parameter cells. Every cell of the parameter mesh is numbered consecutively representing the marker for the resulting model cluster. For every cell of the primary mesh the corresponding (resp. primary cell centre) parameter cell, i.e., the marker of the model cluster, has to be found. Therefore, a search of nearly 700 000 search requests has to be done within a search pool of 10,000 elements. To make this search efficient, a *kd*-tree nearest neighbour search (Bentley, 1975) was applied reducing the total search time drastically. After the search, all cells of the primary mesh with an identical marker are clustered into single parameter regions. Figure 5.7 shows parts of the used primary mesh, the parameter mesh, and one resulting cluster as example. Note, the presented clustering approach is similar to the clustering methods described in Blome (2009). However, the approach of mapping the two meshes seems to be more flexible.

---

[3] The data were kindly provided by Wolfgang Suedekum from Leibniz Institute for Applied Geophysics, Hannover

Figure 5.8a shows the result of the inversion. The transition zone from fresh-water (80 Ωm) down to the salt-water saturated sand (3 Ωm) is interrupted by clay layers that are known to be at depths of 48.5–49.7 m, 52.4–53.8 m and 56–62.3 m. However, the model is cylindrically symmetric because the data from one borehole array cannot differentiate between directions. Only a few unknowns per layer can be resolved representing different distances from the borehole. As a consequent continuation, a 2nd parameter mesh was created that only contains 78 layered cylindrical discs (one for each electrode) representing a 1D parameter distribution.

Figure 5.8b shows the resulting resistivity distribution as a function of depth together with two resistivity probe lines extracted from the tetrahedral model at distances of 0.1 and 2 m from the borehole axis, respectively. Generally, the same behaviour can be observed, but while the 2 m line from the borehole is very smooth the line at the borehole over-accentuates the real distribution. The 1D model shows a distribution that agrees best with the lithological description containing sand (white) and clay (grey) layers. Since the 1D result does not lack regularization artefacts, the resistivities are much more reliable and can be used to derive fluid conductivities using Archie's law and thus salt concentrations, whose temporal behaviour can describe the hydraulic system of the island.

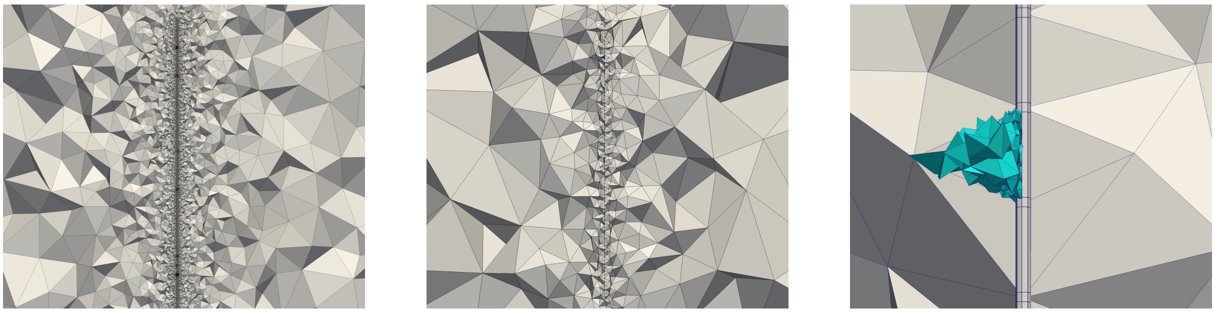

Figure 5.7.: Part of the highly refined primary mesh containing CEM electrodes (left), coarse parameter mesh that reflects a simple discretization for inversion without electrodes (middle) and a selected single region based on clustering (right).

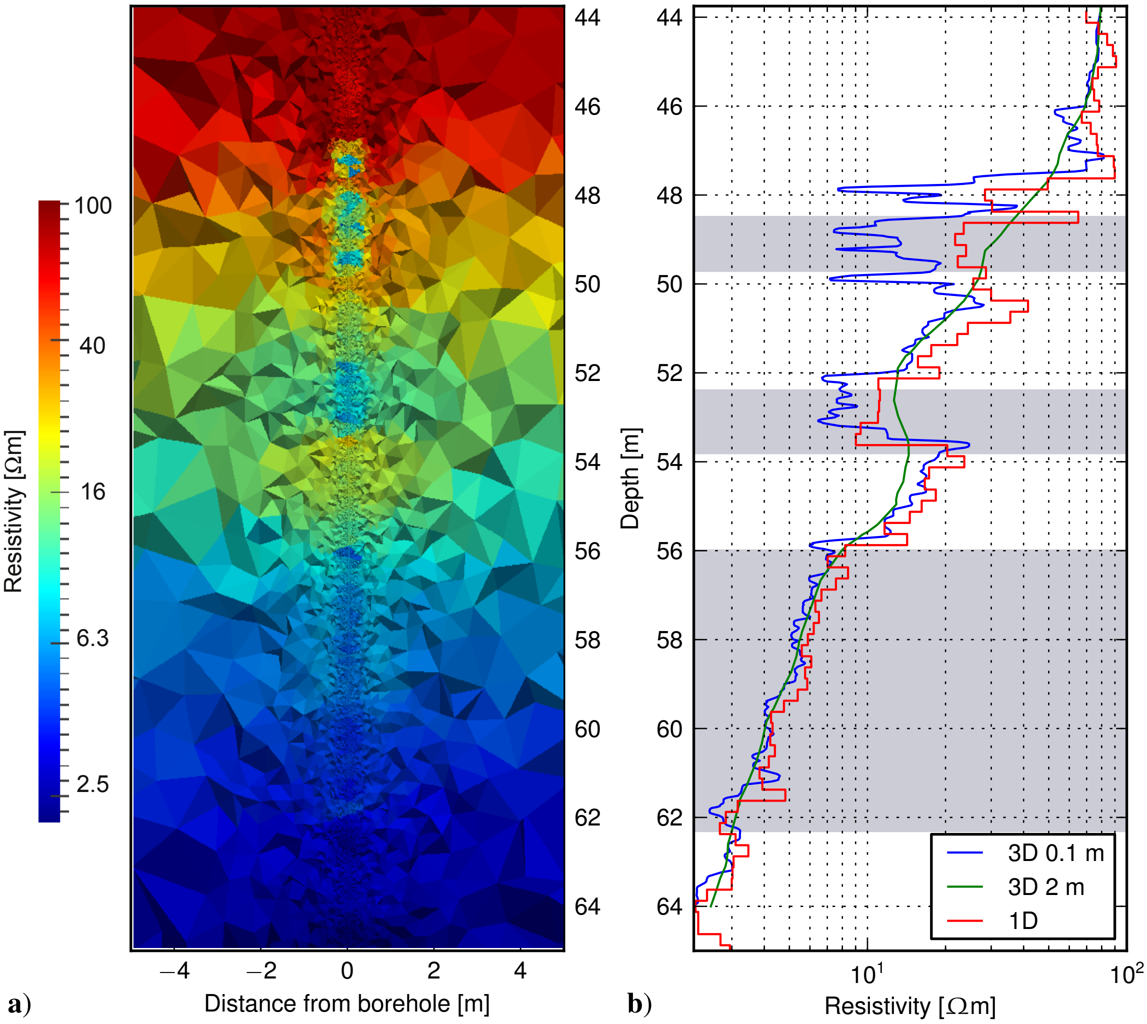

Figure 5.8.: **a**) 3D inversion result for the tetrahedral parametrization including borehole geometry and CEM. **b**) Vertical probe lines at distance 0.1 m and 2 m from the borehole and the result from 1D single region inversion. Lithological description containing sand (white) and clay (grey) layers.

5.3.5. Geological block inversion

In 2008, a regionally scaled DC resistivity survey was carried out by the University of Leipzig in the Cheb Basin, located in the western Eger (Ohře) Rift, Czech Republic. The measurements were designed as a feasibility study for a continuing study to image the conductivity distribution of the upper crust with an investigation depth of 4–5 km (Flechsig et al., 2010). The main purpose of this test was to check whether and in what quality artificial electrical signals are detectable over distances of about 15 km within the western Eger region, which is characterized by high industrial electrical noise.

The data acquisition was performed using dipole-dipole configuration. A current of up to 8 A was injected at three transmitter dipole locations (T1, T2 and T3) using three different feeding dipole lengths (200 m, 400 m and 600 m). The potential signal was measured at 9 different receiver dipoles (P1 . . . 9) with a length of 500 m and 1000 m. The transmitter and the receiver dipoles were spatially distributed and do not follow a survey line. In total 91 different measurements were obtained, whereas only 27 usable data values remained after signal processing with a maximum dipole separation of 14.5 km.

The region concept is applied to obtain a coarse model of the resistivity distribution. A parameter domain with a few geological units is created based on a-priori knowledge about the geological situation, i.e., a few main tectonic faults (Mariánské Lázně Fault Zone (MLF), SW and SSW Eger Rift and its flanks), the sedimentary structure of the Cheb Basin and deposits of granites and phyllites in the subsurface (Škvor and Sattran, 1974; Švancara et al., 2000; Špičáková et al., 2000; Bankwitz et al., 2003; Mlčoch and Skácelová, 2009).

This results in 8 regions, 1 background plus 7 parameter regions, clustered from the tetrahedrons which build up the unstructured forward mesh and contains the boundary of the geological units as well as the electrode positions. All region were assumed as being single parameter regions.

Figure 5.9a shows the regional setting, the transmitter and receiver positions as well as the boundary used for the regions. The resistivity model (Figure 5.9b) consists of seven blocks with inherent resistivity values. One of the blocks is located below the sedimentary fill of the Cheb

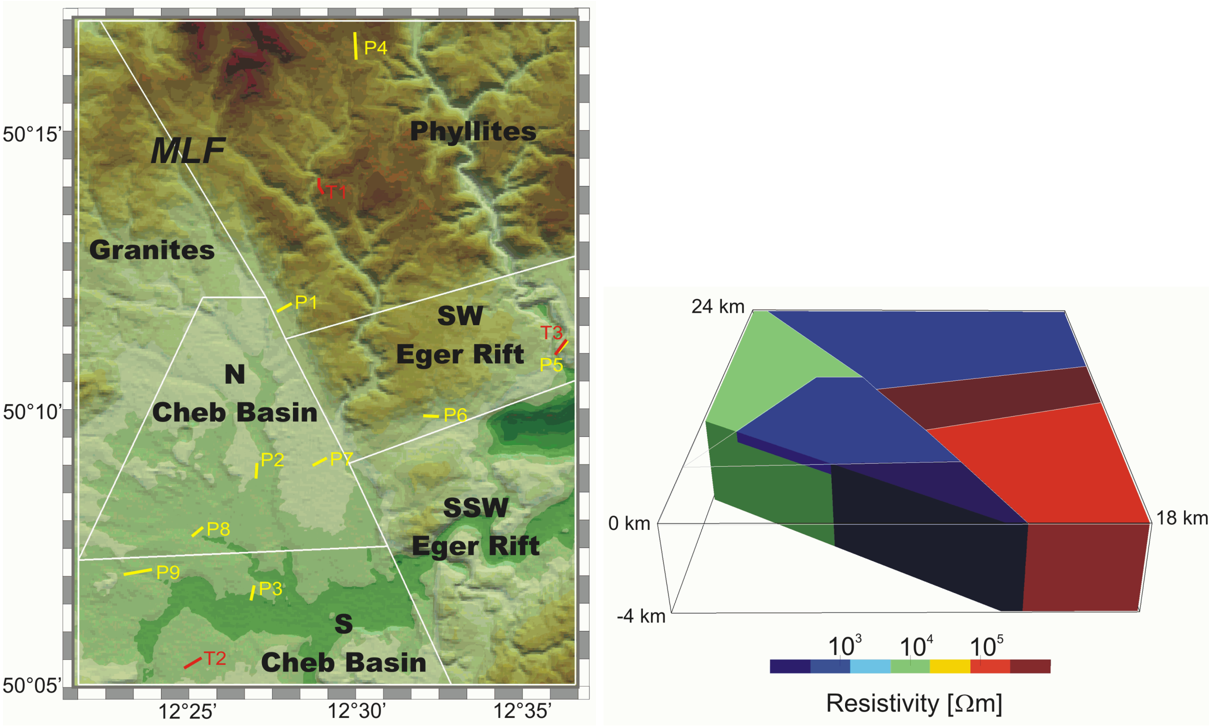

Figure 5.9.: Left: Digital elevation model with the seven selected parameter regions according to geological, geomorphological and geoelectrical a-priori information. The locations denoted as T(1–3) for the three transmitter dipoles(red) and P(1–9) for the nine receiver dipoles (yellow). Right: The result of the single region inversion.

Basin. The mica schists of the southwest part of the Eger Rift and the granites are characterized by high resistivities, whereas the (weathered?) phyllites in the north eastern and the sediments in the Cheb Basin are both represented by lower resistivity values. The high conductivity of the southern part of the Cheb Basin is predominately influenced by the river (Ohře).

Its true that, the very coarse 3D resistivity model does only permit a rather rough first impression of the regional resistivity setting. However, the model structure might gradually be improved and refined by incorporating the results of further geoelectrical investigations and structural data (seismic, velocity models, geology).

5.4. Conclusions

A very flexible regularization scheme is presented that applies individual weights for each cell and each boundary within flexible unstructured meshes. The boundary weight is controlled by an anisotropic smoothness factor or by predefined interfaces in the mesh generation. Those interfaces could be derived from reflection data or borehole data and can be arbitrarily shaped. By lowering the weight to zero, much more contrasted models are obtained that are less affected by smoothness artefacts and whose parameters can be interpreted more easily. However, by neglecting boundary weights, high resistivity gradients can be enhanced but not enforced, if they are not supported by the data.

Contrary to boundary information, the model can be separated into so-called regions. Regions are created in the mesh generation process and reflect a-priori knowledge on the behaviour of specific lithological units of the subsurface. For each region, a model weight and also a vertical smoothness factor, the starting value as well as upper and lower resistivity bounds can be defined. The latter are achieved by using a model transformation function that combines two logarithmic functions. Regions can either be constrained by a spatial derivative (smoothness) or by the absolute deviation to a reference model. The resistivity of a region can be fixed either by the use of very close lower/upper bounds or by applying large model weights. Furthermore, a region can be condensed to a single unknown parameter, e.g., a constant resistivity of a water body. A limited number of single regions can be used to find a three-dimensional model in case of a highly under-determined inverse problem (e.g., Flechsig et al., 2010). On the other hand, single regions can reflect expectations about the model, e.g., simulate 1D resistivity behaviour depending on a 3D environment.

Regions are decoupled to avoid smoothness where changes occur, e.g., in case of borehole fluids (Doetsch et al., 2010) or other sharp contrasts (Clément et al., 2009). However, regions can be coupled using inter-region constraints. By the latter, resistivity information can be incorporated from boreholes using borehole boxes and neighbouring structural constraints. Further applications in ERT could be particularly found in hydrogeophysics, where the main units (unsaturated zone, saturated zone and aquiclude) may be known but changes in the aquifer are of interest. Time-lapse ERT is frequently applied in order to monitor hydraulic processes (Kuras et al., 2009; Oldenborger et al., 2007) or tracer flows (Singha and Gorelick, 2005). After inverting for the initial step, resistivity changes could easily be restricted to an aquifer region.

In all presented cases, the resistivity images are improved by introducing additional information, either about structures or parameters. This information represents a-priori information, assumptions or expectations. However, the inversion result can only be as good as the included data and the preciseness of the a-priori data. It has to be investigated how sensitive the data are with respect to inaccuracies. Furthermore, the effect of additional information has to be quantified by resolution analysis (Friedel, 2003; Günther, 2004).

6. Summary and Outlook

In this work modelling and inversion techniques are presented for the three-dimensional electrical resistivity tomography (ERT) using unstructured discretizations. It is shown that the combination of the described techniques fulfils the requirements for nowadays DC geoelectrical interpretation software. Both, modelling and inversion can be applied to arbitrarily shaped geometries, which allows three-dimensional resistivity surveys at all scales for realistic environments.

Part I describes the modelling of the geoelectrical forward problem, which is solved by the finite element method for tetrahedral meshes with linear and quadratic shape functions. It is shown that the unstructured meshes are suitable for modelling domains with complicated surface and subsurface topography. A moderate problem-adapted a-priori based mesh refinement with global quadratic shape functions allows the best trade-off between accuracy and numerical effort. It is addressed that the resulting system of equations is solved most efficiently using modern multi-frontal direct solvers in combination with matrix reordering strategies. Unstructured discretizations also allow the consideration of spatial extended finite electrodes. Due to a corresponding extension of the forward operator using the complete electrode model, a study about the influence of such electrodes to geoelectrical measurements is given. It is shown that for the most classical ERT survey designs an electrode extent of less than 20% of the electrode spacing allows a valid interpretation by using the common point like electrode approximation. However, the effects become more noticeable for closed geometries such as modelling tanks or lysimeters.

Part II describes the inversion of the geoelectrical data using the previously developed forward operator. The so-called triple-grid-technique is introduced to solve the geoelectrical inverse problem by using a resolution dependent parametrization on arbitrarily shaped three-dimensional domains. Its effectiveness is shown on two examples. An advanced regularization scheme is presented as an extension for the ERT, which allows the flexible incorporation of a-priori information. Structural information such as material interfaces known from other geophysical techniques (e.g., reflection seismics or ground penetrating radar) are included as allowed sharp resistivity contrasts. Model weighting functions can define the allowed deviation of the final resistivity model from given start or reference values. As a consequent further development, the region concept is presented where the parameter domain is subdivided into lithological or geological regions. The inversion behaviour and all regularization parameters can be controlled individually on these regions. It is shown on several examples how the incorporation of a-priori information can significantly improve the resulting ERT images.

The presented modelling and inversion strategies can be improved by further development. A a-posteriori mesh refinement for the forward operator may enable an increase in efficiency and better scalability for accuracy needs in the future. Automated self-adapted parametrization based on resolution analysis will increase the effectiveness of the inversion procedure. To exploit the tendency to increasingly multi-core architecture of nowadays PCs, the efficiency of the modelling and inversion will enormously profit from parallelization.

The method independent inversion framework GIMLi that is originated during this work allows a further way to decrease the ambiguity of the inverse problem, the so-called joint inversion. The incorporation of complete datasets from multiple geophysical disciplines can simple be achieved by the combination of the forward operators to reconstruct a common material parameter, e.g., electrical resistivity from ERT and electromagnetic methods. The advanced regularization scheme provides the basics for the structurally constrained joint inversion, e.g., refraction seismics and ERT by using the structural weights of the gradients from one model as the weight for the other and vice versa. Together with the model transformations, it opens the way to a petrophysical joint inversion for combined parameters, e.g., ground penetrating radar and ERT can be jointly inverted for water content or porosity. By the use of the region concept this can be restricted to predefined regions, e.g., the aquifer.

A. Element integration and shape functions

The contributions for the local element matrices are sought:

$$\text{stiffness matrix }\ \mathbf{S}^{(e)} = \int\limits_{\Omega^{(e)}} \nabla N_k \nabla N_l \,\mathrm{d}\Omega \ \text{ and}$$

$$\text{load vector }\ \mathbf{l}^{(e)} = \int\limits_{\Omega^{(e)}} N_k \,\mathrm{d}\Omega \ \text{ for element } (e) \text{ with } k,l = 1\ldots\mathcal{N}^{(e)} \ \text{ as well as}$$

$$\text{the mass element matrix }\ \mathbf{M}^{(b)} = \int\limits_{\partial\Omega^{(b)}} N_k N_l \,\mathrm{d}\partial\Omega \ \text{ for boundary } (b) \text{ with } k,l = 1\ldots\mathcal{N}^{(b)}$$

for tetrahedral elements and the according triangle boundary facets where $\mathcal{N}^{(e)}$ denote the number of nodes for element (e) and $\mathcal{N}^{(b)}$ the number of nodes for boundary (b), respectively.

The global base functions N_k for a global node P_k are represented by the linear combination of polynomial interpolation rules, the shape functions $N_i^{(e)}$ (i.e., local base functions) which are given for a node P_i of the element (e):

$$N_k = \begin{cases} \sum N_i^{(e)} \forall (e) & \text{for} \quad P_k = P_i^{(e)} \\ 0 & \text{else} \end{cases} \quad \text{for } \ k = 1\ldots\mathcal{N} \ \text{ and } \ i = 1\ldots\mathcal{N}^{(e)}\,.$$

The assembly of the local element matrices are based on three major steps. Firstly, a coordinate transformation, secondly the definition of the shape functions and finally a numerical integration.

Coordinate transformation

The shape functions can be easily described in local element coordinates ζ that can be obtained by a coordinate transformation from the Cartesian coordinates of the element shape. For a tetrahedron ($\mathbb{R}^3$) with the node positions $P_i(x_i, y_i, z_i)$ with $i = 1\ldots4$, the relation between Cartesian and natural or local coordinates ζ are given by:

$$\begin{pmatrix} 1 \\ x \\ y \\ z \end{pmatrix} = \begin{pmatrix} 1 & 1 & 1 & 1 \\ x_1 & x_2 & x_3 & x_4 \\ y_1 & y_2 & y_3 & y_4 \\ z_1 & z_2 & z_3 & z_4 \end{pmatrix} \begin{pmatrix} \zeta_1 \\ \zeta_2 \\ \zeta_3 \\ \zeta_4 \end{pmatrix} . \tag{A.1}$$

Note, the transformation for a triangle is straight forward but not needed for the sought mass element matrix. The local coordinates of an arbitrary tetrahedron can easy be obtained by the solution of the system of equations (A.1) and provide some interesting properties:

Let f be the minimal value of the local coordinates $\zeta_i(x,y,z)$ of an arbitrary point $P(x,y,z)$ for an tetrahedron with the node positions P_i with $i = 1\ldots4$. The position P

1. is outside the tetrahedron of if $f < 0$ and inside for $f > 0$
2. is on the boundary facet (P_i, P_j, P_k) if $f = 0$ for ζ_l
3. equals P_i for $\zeta_i(x,y,z) = 1$ and $\zeta_j = \zeta_l = \zeta_k = 0$.

Shape functions

Shape functions are linear independent functions that are defined on the nodes of an element with the major property that the value of the functions is 1 for the corresponding node and 0 for the remaining nodes:

$$N_i = \begin{cases} 1 & \text{at } P_i \\ 0 & \text{at } P_j \end{cases} \quad \text{for } \; i,j = 1\ldots\mathcal{N}^{(e)} \; \text{ and } \; j \neq i\,. \tag{A.2}$$

Note that, the superscript $^{(e)}$ for the shape functions N (i.e., local base functions) is avoided in the following for convenience.

The shape functions are interpolation rules for the function behaviour within the element. Linear interpolation in local coordinates reads:

$$N_i(\zeta_1, \zeta_2, \zeta_3, \zeta_4) = \zeta_i \;\text{ for }\; i = 1\ldots4 \text{ for a tetrahedron} \tag{A.3}$$

$$N_i(\zeta_1, \zeta_2, \zeta_3) = \zeta_i \;\text{ for }\; i = 1\ldots3 \text{ for a triangle}\,. \tag{A.4}$$

The corresponding quadratic shape functions reads for a tetrahedron :

$$\begin{aligned} N_i =& \zeta_i(2\zeta_i - 1) \quad \text{for} \quad i = 1\dots 4 \\ N_5 =& 4\zeta_1\zeta_2, \quad N_6 = 4\zeta_2\zeta_3, \quad N_7 = 4\zeta_3\zeta_1 \\ N_8 =& 4\zeta_1\zeta_4, \quad N_9 = 4\zeta_2\zeta_4, \quad N_{10} = 4\zeta_3\zeta_4\,, \end{aligned} \tag{A.5}$$

and for a triangle:

$$\begin{aligned} &N_i(\zeta_1,\zeta_2,\zeta_3) = \zeta_i(2\zeta_i - 1) \;\text{ for }\; i = 1\dots 3 \\ &N_4(\zeta_1,\zeta_2,\zeta_3) = 4\zeta_1\zeta_2, \quad N_5(\zeta_1,\zeta_2,\zeta_3) = 4\zeta_2\zeta_3, \quad N_6(\zeta_1,\zeta_2,\zeta_3) = 4\zeta_3\zeta_1\,. \end{aligned} \tag{A.6}$$

Due to the defined shape functions, a function value u can be easily interpolated for an position (x,y,z) within a tetrahedral element by applying the fundamental FEM principle (2.7):

$$u(x,y,z) = \sum_{i=1}^{\mathcal{N}_N} N_i(\zeta_1(x,y,z),\zeta_2(x,y,z),\zeta_3(x,y,z),\zeta_4(x,y,z))u(x_i,y_i,z_i)\,, \tag{A.7}$$

with $\mathcal{N}_N$ the amount of shape functions for the element and $u(x_i,y_i,z_i)$ the known potential values for the corresponding element nodes. In the same manner the gradients of a function can be determined inside an element:

$$\frac{\partial u(x,y,z)}{\partial x} = \sum_{i=1}^{\mathcal{N}_N} \frac{\partial N_i(\zeta_1(x,y,z),\zeta_2(x,y,z),\zeta_3(x,y,z),\zeta_4(x,y,z))}{\partial x} u(x_i,y_i,z_i)\,. \tag{A.8}$$

The partial derivatives of the shape functions in Cartesian coordinates can be obtained by the chain rule:

$$\frac{\partial N_i(\zeta_1(x,y,z),\zeta_2(x,y,z),\zeta_3(x,y,z),\zeta_4(x,y,z))}{\partial x} = \sum_{j=1}^{4} \frac{\partial N_i}{\partial \zeta_j}\frac{\partial \zeta_j}{\partial x}\,, \tag{A.9}$$

and correspondingly for y and z.

Numerical integration

The integration of the element contributions can be done analytically for the most basic element types. However, a numerical integration is more general and based on the Gaussian quadrature rule:

$$\int_{(e)} f(x,y,z)\,\mathrm{d}x\,\mathrm{d}y\,\mathrm{d}z = |(e)| \sum_{i=1}^{n} w_i f(x_i,y_i,z_i)\,, \tag{A.10}$$

using n weights w_i and discrete function values for the sampling positions $f(x_i, y_i, z_i)$ whereas $|(e)|$ denotes the volume of the element or the area of the boundary, respectively

The Integration is exact to an order of $2(p-m)$ whereas p is the polynomial degree of the base function and m denotes the order of the differential operator within the integrand. For tetrahedrons an integration order of 1 for linear and 2 for quadratic base functions are sufficient for the Stiffness matrix and an order of 2 for the load vector. The integration of the mass element matrix for triangle shaped boundary elements needs an integration order of 2 and 4 for linear and quadratic base functions, respectively.

The assembling of the load vector and the local matrices is done element wise according to their shape functions and applying equation (A.10):

$$\mathbf{l}^{(e)} = \int\limits_{\Omega^{(e)}} N_k \,\mathrm{d}\Omega \;\text{ with }\; [l_k] = |(e)| \sum_{i=1}^{n} w_i N_k(i) \tag{A.11}$$

$$\mathbf{M}^{(b)} = \int\limits_{\partial\Omega^{(b)}} N_k N_l \,\mathrm{d}\partial\Omega \;\text{ with }\; [m_{kl}] = |(b)| \sum_{i=1}^{n} w_i N_k(i) N_l(i) \tag{A.12}$$

$$\begin{aligned}\mathbf{S}^{(e)} &= \int\limits_{\Omega^{(e)}} \nabla N_k \nabla N_l \,\mathrm{d}\Omega \;\text{ with}\\ &[s_{kl}] = |(e)| \sum_{i=1}^{n} w_i \frac{\partial N_k(i)}{\partial x}\frac{\partial N_l(i)}{\partial x} + \frac{\partial N_k(i)}{\partial y}\frac{\partial N_l(i)}{\partial y} + \frac{\partial N_k(i)}{\partial z}\frac{\partial N_l(i)}{\partial z}\,.\end{aligned} \tag{A.13}$$

with $k, l = 1 \ldots \mathcal{N}^{(e)}$ and $N(i)$ denotes the shape function $N(\zeta_{1_i}, \zeta_{2_i}, \zeta_{3_i}, \zeta_{4_i})$ for the ith integration sample points in local coordinates. The Integration values that are necessary for the 3D geoelectrical problem using quadratic shape functions are given in Table A.1.

Due to the special nature of the Dirac's delta:

$$\int f(x)\delta(x)\,\mathrm{d}x = f(0)\,, \tag{A.14}$$

a specific handling of the load vector $\mathbf{l}^{(e)}$ which is associated to the DC point source term is necessary:

$$\mathbf{l}^{(e)} = \int\limits_{\Omega^{(e)}} N_k \delta(\mathbf{r}-\mathbf{r}_\mathrm{s}) \,\mathrm{d}\Omega \;\text{ with }\; [l_k] = N_k(\zeta_1(\mathbf{r}_\mathrm{s}), \zeta_2(\mathbf{r}_\mathrm{s}), \zeta_3(\mathbf{r}_\mathrm{s}), \zeta_4(\mathbf{r}_\mathrm{s})) \tag{A.15}$$

This allows node independent source positioning for the total and primary potential calculation. Note, if the source position $\mathbf{r}_\mathrm{s}$ equals a node P_i of the element (e), the entry for $\mathbf{l}^{(e)}$ can be simple expressed as:

$$[l_k] = \begin{cases} 1 & \text{for} \quad \mathbf{r}_s = P_k \\ 0 & \text{else} \end{cases} \quad \text{for } k = 1\ldots\mathcal{N}^{(e)}, \tag{A.16}$$

due to the fundamental property (A.2) of the shape functions.

Table A.1.: Integration weights and abscissas for the tetrahedron and the triangle

Tetrahedron:

Order		Weights w	Coordinates $(\zeta_1, \zeta_2, \zeta_3, \zeta_4)$	
1 [1]	$n = 1$	1.0	a, a, a, a	$a = 0.25$
2 [1]	$n = 4$	0.25	a, b, b, b	$a = 0.585410196$
			b, a, b, b	$b = 0.138196601$
			b, b, a, b	
			b, b, b, a	

Triangle:

Order		Weights w	Coordinates $(\zeta_1, \zeta_2, \zeta_3)$	
2 [1]	$n = 3$	1/3	a, a, b	$a = 0.5$
			b, a, a	$b = 0.0$
			a, b, a	
4 [2]	$n = 6$	0.109951743	a, b, b	$a = 0.816847572$
			b, a, b	$b = 0.091576213$
			b, b, a	
		0.223381589	a, b, b	$a = 0.108103018$
			b, a, b	$b = 0.445948490$
			b, b, a	

[1] Zienkiewicz (1977)

[2] Dunavant (1985)

Bibliography

Alumbaugh, D. L. and Newman, G. A. (2000). Image appraisal for 2-D and 3-D electromagnetic inversion. *Geophysics*, 65(5):1455–1467.

Amestoy, P. R., Davis, T. A., and Duff, I. S. (1996). An Approximate Minimum Degree Ordering Algorithm. *SIAM Journal on Matrix Analysis and Applications*, 17(4):886–905.

Athanasiou, E. N., Tsourlos, P. I., Vargemezis, G. N., Papazachos, C. B., and Tsokas, G. N. (2007). Non-destructive DC resistivity surveying using flat-based electrodes. *Near. Surf. Geophys.*, 5(4):263–272.

Bankwitz, P., Schneider, G., Kämpf, H., and Bankwitz, E. (2003). Structural characteristics of epicentral areas in Central Europe: study case Cheb Basin (Czech Republic). *J. Geodyn.*, 35(1-2):5–32.

Barker, R. D. (1989). Depth of investigation of collinear symmetrical four-electrode arrays. *Geophysics*, 54(8):1031–1037.

Bentley, J. L. (1975). Multidimensional binary search trees used for associative searching. *Communications of the ACM*, 18(9):509–517.

Binley, A., Henry-Poulter, S., and Shaw, B. (1996). Examination of solute transport in an undisturbed soil column using electrical resistance tomography. *Water Resour. Res.*, 32(4):763–769.

Binley, A. and Kemna, A. (2005). *Hydrogeophysics*, chapter Electrical Methods, pages 129–156. Springer, The Netherlands.

Blaschek, R., Hördt, A., and Kemna, A. (2008). A new sensitivity-controlled focusing regularization scheme for the inversion of induced polarization data based on the minimum gradient support. *Geophysics*, 73(2):F45–F54.

Blome, M. (2009). *Efficient measurement and data inversion strategies for large scale geoelectric surveys*. PhD thesis, Swiss Federal Institute of Technology Zürich.

Bock, M., Regenauer-Lieb, K., Lotze, M., Wilke, T., and Rücker, C. (2010). Analysis of thermally induced flows in the laboratory by geoelectrical 3-D tomography. *J. Geophys. Res. Solid Earth*, xx:xxx–xxx. Accepted for publication.

Brecque, D. L., Morelli, G., Daily, B., Ramirez, A., and Lundegard, P. (1995). Occam's inversion of 3D ERT data. In *Proceedings I. International Symposium on Three-Dimensional Electromagnetics in Ridgefield, CT, Oct 4 – 6, 1995*, pages 471–477. University of Utah.

Broyden, C. G. (1972). Quasi-Newton methods. In Murray, W., editor, *Numerical methods for unconstrained optimization*. Academic Press.

Chen, Y., Davis, T. A., Hager, W. W., and Rajamanickam, S. (2009). Algorithm 887: CHOLMOD, supernodal sparse Cholesky factorization and update/downdate. *ACM Trans. Math. Software*, 35(3):No.: 22.

Cheng, K.-S., Isaacson, D., and Gisser, J. N. D. (1989). Electrode models for electric current computed tomography. *IEEE Trans. Biomed. Eng.*, 36(9):918–924.

Clément, R., Descloitres, M., Günther, T., Ribolzi, O., and Legchenko, A. (2009). Influence of shallow infiltration on time-lapse ERT: Experience of advanced interpretation. *Compt. Rendus Geosci.*, 341(10-11):886–898.

Coggon, J. H. (1971). Electromagnetic and electrical modeling by the finite element method. *Geophysics*, 36:132–155.

Constable, S. C., Parker, R. L., and Constable, C. G. (1987). Occam's inversion: A practical algorithm for generating smooth models from electromagnetic sounding data. *Geophysics*, 52:289–300.

Daily, W., Ramirez, A., Newmark, R., and Masica, K. (2004). Low-cost tomographs of electrical resistivity. *The Leading Edge*, 23(5):472–480.

Davis, T. A., Gilbert, J. R., Larimore, S. I., and Ng, E. G. (2000). A column approximate minimum degree ordering algorithm. Technical Report TR-00-005, Department of Computer and Information Science and Engineering, University of Florida.

de Groot-Hedlin, C. and Constable, S. C. (1990). Occams inversion: to generate smooth two-dimensional models from magnetotelluric data. *Geophysics*, 55:1613–1624.

Dey, A. and Morrison, H. F. (1979). Resistivity modelling for arbitrarily shaped three-dimensional structures. *Geophysics*, 44:753–780.

Dieter, K., Paterson, N. R., and Grant, F. S. (1969). IP and resistivity type curves for three-dimensional bodies. *Geophysics*, 34:615–632.

Doetsch, J., Coscia, I., Greenhalgh, S., Linde, N., Green, A., and Günther, T. (2010). The borehole-fluid effect in electrical resistivity imaging. *Geophysics*, 75(4):xxx–xxx. in print.

Druskin, V. (1998). On the uniqueness of inverse problems from incomplete boundary data. *SIAM J. Appl. Math.*, 58(5):1591–1603.

Duff, I. S., Erisman, A. M., and Reid, J. K. (1986). *Direct Methods for Sparse Matrices*. Clarendon Press.

Dunavant, D. A. (1985). High degree efficient symmetrical Gaussian quadrature rules for the triangle. *Int. J. Numer. Meth. Eng.*, 21(6):1129—-1148.

Ellis, R. G. and Oldenburg, D. W. (1994). The pole-pole 3-D DC-resistivity inverse problem: a conjugate gradient approach. *Geophys. J. Int.*, 119(1):187–194.

Farquharson, C. G. and Oldenburg, D. W. (1998). Non-linear inversion using general measures of data misfit and model structure. *Geophys. J. Int.*, 134(1):213–227.

Farquharson, C. G. and Oldenburg, D. W. (2004). A comparison of automatic techniques for estimating the regularization parameter in non-linear inverse problems. *Geophys. J. Int.*, 156(3):411–425.

Flechsig, C., Fabig, T., Rücker, C., and Schütze, C. (2010). Geoelectrical Investigations in the Cheb Basin/W-Bohemia: An Approach to Evaluate the Near-Surface conductivity structure. *Stud. Geophys. Geod*, 54:417–437.

Fox, R. C., Hohmann, G. W., Killpack, T. J., and Rijo, L. (1980). Topographic effects in resistivity and induced-polarization surveys. *Geophysics*, 45(1):75–93.

Friedel, S. (2003). Resolution, stability and efficiency of resistivity tomography estimated from a generalized inverse approach. *Geophys. J. Int.*, 153(2):305–316.

Friedel, S., Brunner, I., Jacobs, F., and Rücker, C. (2000). New results from DC resistivity imaging along the flanks of Merapi volcano. In Buttkus, B., Greinwald, S., and Ostwald, J., editors, *Decade-volcanoes under investigation*, volume 4 of *Mitteilungen der Deutschen Geophysikalischen Gesellschaft, Sonderband IV/2000*, pages 23–29. Deutsche Geophysikalische Gesellschaft.

Frommer, A. and Maass, P. (1999). Fast CG-based methods for Tikhonov-Phillips regularization. *SIAM J. Sci. Computing*, 20(5):1831–1850.

Geometrics (2001). *OhmMapper TR1, Operation Manual.* Geometrics Inc., 2190 Fortune Drive, SanvJose, CA, USA.

Gerstenecker, C., Läufer, G., Steineck, D., Tiede, C., and Wrobel, B. (2005). Validation of Digital Elevation Models around Merapi Volcano, Java, Indonesia. *Nat. Hazards Earth Syst. Sci.*, 5(6):863—-876.

Geselowitz, D. B. (1971). An Application of Electrocardiographic Lead Theory to Impedance Plethysmography. *IEEE Trans. Biomed. Eng.*, BME-18(1):38–41.

Günther, T. (2004). *Inversion Methods and Resolution Analysis for the 2D/3D Reconstruction of Resistivity Structures from DC Measurements*. PhD thesis, Freiberg University of Mining and Technology. Available from `http://fridolin.tu-freiberg.de`.

Günther, T., Rücker, C., and Spitzer, K. (2006). Three-dimensional modelling and inversion of dc resistivity data incorporating topography – II. Inversion. *Geophys. J. Int.*, 166:506–517.

Günther, T. and Rücker, C. (2009). Advanced inversion strategies using a new Geophysical Inversion and Modelling Library. In *Ext. Abstr. 15th European Meeting of Environmental and Engineering Geophysics*, Dublin, Ireland.

Haber, E. (2005). Quasi-Newton methods for large-scale electromagnetic inversion problems. *Inverse Probl.*, 21:305–323.

Hansen, P. C. and O'Leary, D. P. (1993). The use of the L-curve in the regularization of discrete ill-posed problems. *SIAM J. Sci. Comput.*, 14(6):1487–1503.

Heikkinen, L. M., Vilhunen, T., West, R. M., and Vauhkonen, M. (2002). Simultaneous reconstruction of electrode contact impedances and internal electrical properties: II. Laboratory experiments. *Meas. Sci. Technol.*, 13:1855–1861.

Herwanger, J. V., Pain, C. C., Binley, A., de Oliveira, C. R. E., and Worthington, M. H. (2004). Anisotropic resistivity tomography. *Geophys. J. Int.*, 158(2):409–425.

Hestenes, M. R. and Stiefel, E. (1952). Methods of conjugate gradients for solving linear systems. *J. Res. Nat. Bur. Stand*, 49:409–436.

Holcombe, H. T. and Jiracek, G. R. (1984). Three-dimensional terrain corrections in resistivity surveys. *Geophysics*, 45:75–93.

Igel, J. (2007). *On the Small-Scale Variability of Electrical Soil Properties and its Influence on Geophysical Measurements*. PhD thesis, University of Frankfurt/Main.

Karypis, G. and Kumar, V. (1998). A Fast and High Quality Multilevel Scheme for Partitioning Irregular Graphs. *SIAM Journal on Scientific Computing*, 20(1):359–392.

Kemna, A. (2000). *Tomographic inversion of complex resistivity*. PhD thesis, Ruhr-Universität Bochum.

Kershaw, D. S. (1978). The incomplete Cholesky-conjugate gradient method for the iterative solution of systems of linear equations. *J. Comput. Phys.*, 26(1):43–65.

Knödel, K., Lange, G., and und Hans-Jürgen Voigt (2007). *Environmental Geology: Handbook of Field Methods and Case Studies*. Springer Berlin Heidelberg New York.

Kuras, O., Beamish, D., Meldrum, P. I., and Ogilvy, R. D. (2006). Fundamentals of the capacitive resistivity technique. *Geophysics*, 71(3):G135–G152.

Kuras, O., Pritchard, J., Meldrum, P., Chambers, J., Wilkinson, P., Ogilvy, R., and Wealthall, G. (2009). Monitoring hydraulic processes with automated time-lapse electrical resistivity tomography (ALERT). *Compt. Rendus Geosci.*, 341(10-11):868–885.

Large, D. B. (1971). Electrical potential near a spherical body in a conducting half-space. *Geophysics*, 36(4):763–767.

Lelièvre, P. G. and Oldenburg, D. W. (2009). A comprehensive study of including structural orientation information in geophysical inversions. *Geophys. J. Int.*, 178(2):623–637.

Li, Y. and Oldenburg, D. W. (1999). 3-D Inversion of DC resistivity data using an L-curve criterion. In *69th Annual Internat. Mtg., Soc. Expl. Geophys., Expanded Abstracts*.

Li, Y. and Spitzer, K. (2002). Three-dimensional DC resistivity forward modelling using finite elements in comparison with finite-difference solutions. *Geophys. J. Int.*, 151(3):924–934.

Loke, M., Acworth, I., and Dahlin, T. (2003). A comparison of smooth and blocky inversion methods in 2-D electrical imaging surveys. *Exploration Geophysics*, 34(3):182–187.

Loke, M. and Barker, R. (1996a). Rapid least-squares inversion of apparent resistivity pseudosections by a quasi-Newton method. *Geophys. Prospect.*, 44(1):131–152.

Loke, M. H. and Barker, R. D. (1996b). Practical techniques for 3D resistivity surveys and data inversion. *Geophys. Prospect.*, 44(3):499–523.

Lowry, T., Allen, M. B., and Shive, P. N. (1989). Singularity removal: A refinement of resistivity modeling techniques. *Geophysics*, 54(6):766–774.

McGillivray, P. R. and Oldenburg, D. W. (1990). Methods for calculating Fréchet derivatives and sensitivities for the non-linear inverse problem: a comparative study. *Geophys. Prospect.*, 38(5):499–524.

Menke, W. (1989). *Geophysical Data Analysis: Discrete Inverse Theory*, volume 45 of *International Geophysics Series*. Academic Press Inc.

Militzer, H. and Weber, F., editors (1985). *Angewandte Geophysik*. Springer. Band 2.

Mlčoch, B. and Skácelová, Z. (2009). Digital elevation model of the crystalline basement of the Cheb and Sokolov Basin araeas. *Z. Geol. Wiss.*, 37:145–152.

Mufti, I. R. (1976). Finite-difference resistivity modeling for arbitrarily shaped two-dimensional structures. *Geophysics*, 41:62–78.

Neukirch, M. and Klitzsch, N. (2010). How to Invert Capacitive Resistivity (Line Electrode) Measurements with DC Inversion Programs. *Vadose Zone*. in print.

Okabe, M. (1981). Boundary element method for the arbitrary inhomogeneities problem in electrical prospecting. *Geophys. Prospect.*, 29(1):39–59.

Oldenborger, G. A., Knoll, M. D., Routh, P. S., and LaBrecque, D. J. (2007). Time-lapse ERT monitoring of an injection/withdrawal experiment in a shallow unconfined aquifer. *Geophysics*, 72(4):F177–F187.

Pagliara, G. and Vignoli, G. (2006). Focusing Inversion Techniques Applied to Electrical Resistance Tomography in an Experimental Tank. In *XI International Congress of the International Association for Mathematical Geology*, Liege (Belgique).

Pain, C. C., Herwanger, J. V., Saunders, J. H., Worthington, M. H., and de Olivieira, C. R. E. (2003). Anisotropic resistivity inversion. *Inverse Probl.*, 19:1081–1111.

Park, S. K. and Van, G. P. (1991). Inversion of pole-pole data for 3-d resistivity structure beneath arrays of electrodes. *Geophysics*, 56:951–960.

Paulson, K., Breckon, W., and Pidcock, M. (1992). Electrode Modelling in Electrical Impedance Tomography. *SIAM J. Appl. Math.*, 52(4):1012–1022.

Portniaguine, O. and Zhdanov, M. S. (1999). Focusing geophysical inversion images. *Geophysics*, 64(3):874–887.

Pous, J., Marcuello, A., and Queralt, P. (1987). Resistivity inversion with a priori information. *Geophys. Prospect.*, 35(5):590–603.

Press, W. H., Teukolsky, S. A., Vetterling, W. T., and Flannery, B. P. (1988–1992). *Numerical Recipes in C: The art of scientific computing*. Cambridge University Press.

Pridmore, D. F., Hohmann, G. W., Ward, S. H., and Sill, W. R. (1981). An investigation of finite-element modelling for electrical and electromagnetical data in three dimensions. *Geophysics*, 46:1009–1024.

Queralt, P., Pous, J., and Marcuello, A. (1991). 2-D resistivity modeling: An approach to arrays parallel to the strike direction. *Geophysics*, 56(7):941–950.

Ridd, P. (1994). Electric potential due to a ring electrode. *IEEE J. Ocean. Eng.*, 19(3):464–467.

Roy, A. and Apparao, A. (1971). Depth of investigation in direct current methods. *Geophysics*, 36(5):943–959.

Rücker, C. and Günther, T. (2011). The simulation of finite ERT electrodes using the complete electrode model. *Geophysics*. Accepted for publication: March 2011.

Rücker, C., Günther, T., and Spitzer, K. (2006). Three-dimensional modelling and inversion of dc resistivity data incorporating topography – I. Modelling. *Geophys. J. Int.*, 166:495–505.

Saad, Y. (1996). *Iterative Methods for Sparse Linear Systems*. PWS, Boston.

Sasaki, Y. (1989). Two-dimensional joint inversion of magnetotelluric and dipole-dipole resistivity data. *Geophysics*, 54:254–262.

Sasaki, Y. (1994). 3-D resistivity inversion using the finite-element method. *Geophysics*, 59(11):1839–1848.

Schütze, C., Rücker, C., and Flechsig, C. (2010). Large-scale geoelectrical measurements at the Central Bohemian shear zone nearby the research well Rittsteig (Bavaria, Germany). *Z. Geol. Wiss.*, 38(1):69–77.

Shewchuk, J. R. (2002). Delaunay Refinement Algorithms for Triangular Mesh Generation. *Computational Geometry: Theory and Applications*, 22(1–3):21–74.

Si, H. (2004). TetGen. A 3D Delaunay tetrahedral mesh generator. v.1.3. Users manual 4, WIAS.

Singha, K. and Gorelick, S. M. (2005). Saline tracer visualized with three-dimensional electrical resistivity tomography: Field-scale spatial moment analysis. *Water Resour. Res.*, 41:W05023.

Škvor, V. and Sattran, V. (1974). Geological Map of CR 1:50.000, 11-14, Cheb. Technical report, Czech Geological Survey, Prague, Czech Republic.

Sommerfeld, A. (1967). *Vorlesungen über Theoretische Physik, Band III: Elektrodynamik*. Akademische Verlagsgesellschaft Geest & Portig, Leipzig, 4th edition.

Špičáková, L., Uličný, D., and Koudelková, G. (2000). Tectonosedimentary evolution of the Cheb Basin (NW Bohemia, Czech Republic) between late Oligocene and Pliocene: a preliminary note. *Stud. Geophys. Geod.*, 44(4):556–580.

Spitzer, K. (1995). A 3-D finite-difference algorithm for DC resistivity modelling using conjugate gradient methods. *Geophys. J. Int.*, 123(3):903–914.

Spitzer, K. (1998). The three-dimensional DC sensitivity for surface and subsurface sources. *Geophys. J. Int.*, 134(3):736–746.

Spitzer, K. and Wurmstich, B. (1999). Speed and Accuracy in 3D Resistivity Modeling. In Oristaglio, M. and Spies, B., editors, *Three-dimensional Electromagnetics*, number 7 in Geophysical Developments. Society of Exploration Geophysicists.

Südekum, W., Grinat, M., Epping, D., Grelle, T., and Meyer, R. (2010). Vertikale Elektrodenstrecken zur Erkundung von Änderungen im Salz-Süßwasser-Übergangsbereich auf Borkum (german). *Brunnenbau*, 12:68–71.

Sugimoto, Y. (1999). Shallow high-resolution 2–D and 3–D electrical crosshole imaging. *The Leading Edge*, 18(12):1425–1428.

Švancara, J., Gnojek, I., Hubatka, F., and Dědáček, K. (2000). Geophysical field pattern in the West Bohemian geodynamic active area. *Stud. Geophys. Geod.*, 44(2):307–326.

Telford, W., Geldart, L., and Sheriff, R. (1976). *Applied Geophysics*. Cambridge University Press, 1st edition.

Tikhonov, A. N. and Arsenin, V. Y. (1977). *Solution of Ill-Posed Problems*. V.H. Winston ans Sons, Washington D.C.

Toledo, S., Chen, D., and Rothkin, V. (2001). TAUCS – A Library of Sparse Linear Solvers. `http://www.tau.ac.il/~stoledo/taucs/`.

Tripp, A., Hohmann, G., and Swift, C. (1984). Two-dimensional resistivity inversion. *Geophysics*, 49:1708–1717.

Ullrich, B., Günther, T., and Rücker, C. (2008). Electrical resistivity tomography methods for archaeological prospection. In Posluschny, A., Lambers, K., and Herzog, I., editors, *Layers of Perception. Proceedings of the 35th International Conference on Computer Applications and Quantitative Methods in Archaeology (CAA)*, Berlin.

Vauhkonen, P., Vauhkonen, M., Savolainen, T., and Kaipio, J. (1999). Three-dimensional electrical impedance tomography based on the complete electrode model. *IEEE Trans. Biomed. Eng.*, 46:1150–1160.

Verführt, R. (1993). A review of a posteriori error estimator and adaptive mesh refinement. Technical report, Institut für Angewandte Mathematik, Universität Zürich.

Vogel, C. R. (1996). Non-convergence of the L-curve regularization parameter selection method. *Inverse Probl.*, 12:535–547.

Wang, M., Dickin, F., and Mann, R. (1999). Electrical Resistance Tomographic Sensing System for Industrial Applications. *Chem. Eng. Comm.*, 175(1):49–70.

Wirgin, A. (2004). The inverse crime. *arXiv*, math-ph/0401050v1:1–8.

Wu, X., Xiao, Y., Qi, C., and Wang, T. (2003). Computations of secondary potential for 3D DC resistivity modelling using an incomplete Choleski conjugate-gradient method. *Geophys. Prospect.*, 51:567–577.

Xu, S. Z. (2001). *The boundary element method in geophysics*. Geophysical monograph series. Society of exploration geophysics.

Xu, S.-Z., Gao, Z., and Zhao, S.-k. (1988). An integral formulation for three-dimensional terrain modeling for resistivity surveys. *Geophysics*, 53(4):546–552.

Yi, M.-J., Kim, J.-H., and Chung, S.-H. (2003). Enhancing the resolving power of least-squares inversion with active constraint balancing. *Geophysics*, 68(3):931–941.

Yi, M.-J., Kim, J.-H., Song, Y., Cho, S.-J., Chung, S.-H., and Suh, J.-H. (2001). Three-dimensional imaging of subsurface structures using resistivity data. *Geophys. Prospect.*, 49(4):483–497.

Zhang, J., Mackie, R. L., and Madden, T. R. (1995). 3-D resistivity forward modeling and inversion using conjugate gradients. *Geophysics*, 60(5):1313–1325.

Zhao, S. and Yedlin, M. J. (1996). Some refinements on the finite-difference method for 3-D DC resistivity modeling. *Geophysics*, 61(5):1301–1307.

Zhdanov, M. S. (2002). *Geophysical Inverse Theory and Regularization Problems*. Methods in Geochemistry and Geophysics. Elsevier, Amsterdam - New York - Tokyo.

Zhdanov, M. S. and Keller, G. V. (1994). *The Geoelectrical Methods in Geophysical Exploration*. Methods in Geochemistry and Geophysics. Elsevier, Amsterdam - London - New York - Tokyo.

Zhou, B. and Greenhalgh, S. A. (2001). Finite element three-dimensional direct current resistivity modelling: accuracy and efficiency considerations. *Geophys. J. Int.*, 145(3):679–688.

Zienkiewicz, O. C. (1977). *The Finite Element Method*. McGraw-Hill, London, 3rd edition.

Curriculum Vitae

Personal

Name	Carsten Rücker
Date of Birth	02.07.1973
Place of Birth	Schmölln, Germany
Nationality	German

Professional record

01/2011 –	Research assistant at the Department of Applied Geophysics, Berlin University of Technology
02/2000 – 11/2009	Research assistant at the Institute of Geophysics and Geology, University of Leipzig
01/2000	Diploma in geophysics at the University of Leipzig Diploma thesis: “Die Methode der Finiten Elemente mit adaptiver Gittererzeugung und Integration eines Mehrgitterverfahrens zum Lösen des gleichstromgeoelektrischen Vorwärtsproblems”
10/1994 – 01/2000	Studies in geophysics at the University of Leipzig, (Leipzig, Germany)

Acknowledgments

I wish to express my gratitude to my supervisor Prof. Dr. Franz Jacobs, for giving me the opportunity to work in the Institute of Geophysics and Geology and for providing me the freedom to develop and follow my own ideas. I am grateful to Prof. Dr. Ugur Yaramanci for kindly serve as the second referee.

Especially I am grateful to Dr. Thomas Günther for all the fruitful discussions and the close collaboration during the last decade and I am look forward to further cooperation and some exciting common projects.

I would like to thank Dr. Christina Flechsig, Dr. Claudia Schütze and Dr. Anita Just for the opportunity of common field work and Dr. Sven Friedel, for showing me the world of geoelectrics. Special thanks to my former roommate Dr. Ulrich Serfling for many scientific and non-scientific discussions.

Also, I wish to thank Heike Tröller for proofreading my English language and le-tex publishing services for introducing me to the basics of scientific typesetting.

Last, but not least, I express my gratitude to my family and friends for all the patience over the last years.